

UNIVERSITY OF OKLAHOMA
GRADUATE COLLEGE

DESIGN AND IMPLEMENTATION OF A PHASED ARRAY ANTENNA
FOR MULTI-MISSION APPLICATIONS

A DISSERTATION
SUBMITTED TO THE GRADUATE FACULTY
in partial fulfillment of the requirements for the
Degree of
DOCTOR OF PHILOSOPHY

By
MIRHAMED MIRMOZAFARI
Norman, Oklahoma
2018

DESIGN AND IMPLEMENTATION OF A PHASED ARRAY ANTENNA
FOR MULTI-MISSION APPLICATIONS

A DISSERTATION APPROVED FOR THE
SCHOOL OF ELECTRICAL AND COMPUTER ENGINEERING

BY

Dr. Guifu Zhang, Chair

Dr. Yang Hong

Dr. Richard Doviak

Dr. Hjalti Sigmarsson

Dr. Yan Zhang

*To my father for his continuous support,
my wife for her boundless encouragement,
and my mother for her unconditional love.*

Acknowledgments

First, I would like to express my sincere gratitude to my advisor Professor Guifu Zhang for his continuous support, patient supervision, and encouragement. His invaluable vision and precious advice helped me to gain experience in polarimetric phased array antennas and shaped my academic career. I deeply admire his commitment to academic excellence and dedication to weather community.

I am thankful to the members of my Ph.D. committee, Professor Yang Hong, Professor Richard Doviak, Professor Hjalti Sigmarsson, and Professor Yan Zhang for their insightful and helpful suggestions. Special thanks to Professor Richard Doviak for his precise comments and commitment to be a great coauthor of my publications. It was a great honor for me to being able to have his name as coauthor on my papers. I also sincerely thank other and former ARRC faculty members, Professor Caleb Fulton and Dr. Shaya Karimkashi for their valuable expertise, time, and guidance throughout my research. My special thanks to Dr. Shahrokh Saeedi who has trained me and helped me tirelessly in the fabrication of my antennas. He, as a precious coauthor of my papers, has revised them meticulously and has been a constant source of support for me.

I am grateful to the generous financial support for my research by National Oceanic and Atmospheric Administration (NOAA). The staff members at the

Advanced Radar Research Center (ARRC) and School of Electrical and Computer Engineering (ECE) deserve my sincere thanks as well. I would like to extend my thanks to all my friends at the University of Oklahoma, Mehrad Amirkhosravi, Maya Pishvar, Mohamad Darayi, Nazanin Tajik, Saeid Hosseinpour, Nushin Nasr, Mohamad Naghashnejad, Amir Arshadi, Elika Bahrehvar, Kewston Salimi, Hadi Saeidi Manesh, Neda Bathaei, and all whose names I know so well but are too many to be listed here. I wish them all the best of luck with their studies and future careers. I would also like to thank all my distant friends. My special thanks to my good friends, Sahand Yazdan Parast and Seied Jamal Mirhedayati, for their invaluable friendship and support.

Last, but not least, I would like to thank my family. I am sincerely grateful to my beloved wife (Azadeh Gilanpour) for her encouragement and sacrifice during the past four years. I would like to extend my gratitude to my father (Jalal Mirmozafari) and my mother (Ashrafosadat Gheisardoust) for their unconditional support and love. I know that I am forever in your debt. I appreciate all the countless support from my wife's parents (Jamshid and Goli Gilanpour). I am so grateful to my brothers (Toumaj and Pouya), my sister in law (Sara) and my little nephew (Samiar) who waited up for me until I finished my defense. None of this work would have been possible without them. My gratitude to them is more than that can be expressed in words. Thank you.

Table of Contents

Acknowledgments	iv
Abstract	xvii
1 Introduction	1
1.1 Multifunction Phased Array Radar	1
1.2 Phased Array Radar (PAR)	2
1.3 Polarimetric Phased Array Radar (PPAR)	3
1.4 Phased Array Antennas for MPAR	4
1.4.1 Planar Polarimetric Phased Array Radar (PPPAR)	5
1.4.2 Cylindrical Polarimetric Phased Array Radar (CPPAR)	6
1.5 Motivation for Dissertation and Research Objectives	6
1.6 Outline of Dissertation	8
2 A Review of Dual-linear Polarized Antennas	11
2.1 Introduction	11
2.1.1 Interaction Between Two Radiation Elements in a Dual Polarization Antenna	11
2.2 Similar Orthogonal Elements - Group I	13
2.2.1 Crossed Dipole	14
2.2.2 Crossed Slot	17

2.3	A Patch Antenna With Two Orthogonal Modes - Group II . . .	20
2.3.1	Microstrip-fed Dual-polarized Patch Antennas	23
2.3.2	Probe-fed Dual-polarized Patch Antennas	25
2.3.3	Aperture-coupled Dual-polarized Patch Antennas . . .	29
2.3.4	Hybrid-fed Dual-polarized Patch Antennas	34
2.4	Two Different Radiation Elements in a Dual-polarized Antenna - Group III	35
2.4.1	Complementary Elements	36
2.4.2	Non-complementary Elements	37
3	Proposed Crossed Dipole and its Modification	39
3.1	Introduction	39
3.2	Proposed Crossed Dipole	40
3.2.1	Design and Discussion	41
3.2.2	Fabrication Process	43
3.2.3	Measurement Verification	44
3.3	A Modified Version of the Proposed Crossed Dipole	47
3.3.1	Measurement Verification and Matched Beams	51
4	Linear Array Antenna of Crossed Dipoles	55
4.1	Introduction	55
4.2	Antenna Structure and Design	58
4.3	Mirrored Arrangement of Crossed Dipole Elements and Cross- Polarization Reduction	60
4.4	Embedded Element Pattern of the Proposed Antenna in CPPAR	62
4.4.1	Implementation of Proposed Unit Cell Method	63
4.4.2	Validation of Proposed Unit Cell Method	66

5	Planar Array Antenna of Crossed Dipoles	69
5.1	Introduction	69
5.2	Array Antenna Geometry and Design	71
5.3	Imaged Arrangements of Crossed Dipole Elements and Radiation Characterization of Proposed Planar Array	74
5.3.1	Notation and Terminologies	77
5.3.2	Pattern Multiplication in Configured Arrays	80
5.3.3	Subarrays Radiation Patterns Properties	82
5.3.4	Configuration A Subarray Radiation Pattern	82
5.3.5	Configuration B Subarray Radiation Pattern	83
5.3.6	The Proposed Element and Its Planar Array Properties	88
6	Conclusions and Future Work	93
6.1	Introduction	93
6.1.1	Contributions	95
6.2	Future Work	95
6.2.1	Wide Bandwidth Crossed Dipole Antenna	96
6.2.2	Fully Printed Crossed Dipole over Perfect Magnetic Surface	96
6.2.3	Planar Array Antenna with Polarization Purity in and out of the Principal Planes	97
6.2.4	3D Printed Crossed Dipole Antenna	99
	References	101
	Appendix A 3D Printing of Non-Planar Linear Dipole Phased Array Antennas	110

List of Tables

2.1	A comparison of the performance of antennas in group I. . . .	19
2.2	A comparison of the performance of microstrip-fed dual-polarized antennas in group II.	24
2.3	A comparison of the performance of probe-fed dual-polarized antennas in group II.	28
2.4	A comparison of the performance of aperture-coupled dual-polarized antennas in group II.	35
2.5	A comparison of the performance of antennas in group III. . .	38
3.1	Detailed Dimensions of the fabricated antenna (unit: <i>mm</i>) . . .	41
3.2	Detailed Dimensions of the fabricated antenna (unit: <i>mm</i>) . . .	50
4.1	Detailed Dimensions of the fabricated antenna (unit: <i>mm</i>) . . .	59
5.1	A comparison between patch antenna array performances in different configurations in azimuth plane.	78
5.2	A comparison between patch antenna array performances in different configurations in elevation plane.	78
A.1	Detailed Dimensions of the fabricated antenna (unit: <i>mm</i>) . . .	114

List of Figures

1.1	Aircraft surveillance and weather radar networks, (a) Airport Surveillance Radars, (b) Terminal Doppler Weather Radars, (c) Air Route Surveillance Radars, (d) National Weather Surveillance Radars.	2
1.2	(Right) 8 by 8 dual polarized subarray panel. (Left) Two-panel subarray used to demonstrate overlapped beamforming (From [1]).	5
1.3	(left) Cylindrical array schematic with four dual polarized beams transmitting simultaneously. (Right) Cylindrical Polarimetric Phased Array Radar demonstrator (From [4]).	7
1.4	19-element frequency scanning antenna array under test in the Federal Aviations Administration (FAA) anechoic chamber (From [6]).	8
2.1	Interaction between two radiation elements in a dual polarized antenna.	13
2.2	Voltage distribution of an excited vertical dipole and null locus representation.	15
2.3	Dual-polarized magneto-electric dipoles, (a) Γ -shaped feedlines (Concept from [12]) , (b) differential excitation along with current distribution on antenna (Concept from [8]).	16

2.4	A crossed slot excited with open-ended microstriplines, (a) 3-D and expanded views of the antenna (Concept from [16]), (b) coupled currents from the horizontal slot to the vertical one.	18
2.5	A differential excited crossed slot, (a) top view of the antenna along with magnetic current distributions, (b) bottom view of the antenna (Concept from [16]).	19
2.6	A square patch antenna, (a) driving port at arbitrary point (x,y), (b) TM ₁₀ fields distributions and copolar pattern, (c) TM ₂₀ fields distributions and copolar pattern, (d) TM ₃₀ fields distributions and copolar pattern.	21
2.7	Cross polarization comparison of antenna in [23] in principal planes with different excitation schemes.	22
2.8	Dual-polarized microstrip-fed patch antennas, (a) edge-fed excitation (Concept from [25]), (b) corner-fed excitation (Concept from [26]), (c) differential excitation (Concept from [28]).	24
2.9	Dual-polarized probe-fed patch antennas, (a) simple probe excitation (Concept from [30]), (b) L-shaped probe excitation (Concept from [33]), (c) meander probe excitation (Concept from [34]).	26
2.10	A dual-polarized differential driven antenna. (a) Patch and L-shaped probes, (b) Differential feed network (Concept from [33]).	27
2.11	Dual-polarized patch antennas, (a) square patch with L-shaped configuration of slots (Concept from [38]), (b) circular patch with T-shaped configuration of slots (Concept from [39]).	30

2.12	Dual-polarized patch antennas with H-shaped aperture-coupled excitation, (a) slots at the edge of the patch (Concept from [41]), (b) slots close to patch center (Concept from [42]).	31
2.13	A dual-polarized patch antenna with cross slots aperture (Concept from [45]).	32
2.14	Centered cross slot excitations, (a) rectangular feedlines in separate layers (Concept from [47]), (b) asymmetric offset feedlines (Concept from [48]), (c) balanced feed with feedlines on opposite sides of the ground plane (Concept from [49]).	33
2.15	Hybrid-fed patch antennas, (a) aperture-coupled probe-fed excitation (Concept from [51]), (b) aperture-coupled meander probe-fed excitation (Concept from [52]).	34
2.16	3-D and expanded views of a dual-polarized monopole-slot antenna (Concept from [53]).	36
2.17	Dual polarized omnidirectional antennass (a) a notch-wire antenna (Concept from [54]), (b) a ring patch-arcs antenna (Concept from [55]), (c) a circular patch-dipoles antenna (Concept from [56]).	37
3.1	Proposed crossed dipole antenna, (a) fundamental idea. (b) implemented version with exploded views of two orthogonal boards.	41
3.2	Prototype of the proposed antenna, (a) side view of individual boards and collocated crossed dipole without ground plane, (b) top view with subset showing the antenna stack-up, and (c) bottom view.	43
3.3	Simulated and measured S-parameters of the crossed dipole antenna.	45

3.4	Different widths of two branches of the balun.	46
3.5	Pattern measurement set-up, (a) Side view, (b) Front view. . .	47
3.6	Measured and simulated radiation patterns of the proposed antenna at principal planes, (a) E-plane, (b) H-plane.	48
3.7	The phase imbalance of the proposed balun versus frequency. .	48
3.8	A modified version of the proposed crossed dipole antenna, (a) fundamental idea. (b) implemented version with exploded views of two orthogonal boards.	49
3.9	Input impedance of the antenna with dipole dimensions, (a) variation in antenna length ($W=3$ mm), (b) variation in antenna width ($L=20$ mm).	50
3.10	Prototype of the modified crossed dipole antenna.	51
3.11	Simulated and measured S-parameters of the proposed antenna.	52
3.12	Simulated and measured radiation patterns of proposed crossed dipole at different frequencies in both principal planes.	53
3.13	Matched copolar patterns of dipoles at principal planes.	53
3.14	Simulated envelope correlation coefficient of the antenna.	54
4.1	CPPAR antenna array and demonstrator designed and fabricated at the University of Oklahoma (From [4]).	56
4.2	Frequency scanning linear array and the exploded view of its respective patch antenna (From [65]).	57
4.3	Linear array of the crossed dipole and the exploded view of its element.	59
4.4	Scanning performance of the proposed linear array, (a) active VSWR of crossed dipole element, (b) active port-isolation versus frequency in scanning.	59

4.5	Phase imbalance of the half-wavelength balun and its effect on disturbance of the null locus.	60
4.6	The proposed imaged arrangement for the linear array antenna.	61
4.7	A prototype of 8 imaged crossed dipole linear array antenna. .	62
4.8	Scanning performance of the proposed linear array, (a) horizontal polarization, (b) vertical polarization.	63
4.9	(a) A cylindrical array of vertical dipole elements, (b) equivalent circular array of column elements, (c) unit cell of a column element.	64
4.10	A comparison between full wave and unit cell results of a vertical dipole embedded element pattern.	67
4.11	A comparison between embedded element patterns of (a) proposed crossed dipole and (b) the stacked patch antenna. . . .	68
5.1	(a) NOAA's National Weather Research Testbed (NWRT), (b) The MPAR 10-panel proof of concept demonstrator (From [1]).	70
5.2	Geometry of the proposed array antenna and its respective crossed dipole element.	72
5.3	Impedance transformation from the SMA connector to the dipole.	72
5.4	Unit cell of proposed crossed dipole.	73
5.5	Scan element pattern of the proposed crossed dipole in E-plane.	74
5.6	Simulated (a) active VSWR and, (b) active port-isolation of the proposed crossed dipole versus frequency in scanning.	74
5.7	Different 2×2 subarray configurations, (a) Configuration A, (b) Configuration B, (c) Configuration C, and (d) Configuration D (Concept from [81]).	75

5.8	16×8 planar patch array antenna gains in principal planes, (a) Configuration A, (b) Configuration B, (c) Configuration C, and (d) Configuration D.	76
5.9	16×8 planar array including 8×4 identical 2×2 subarrays. . .	78
5.10	Patch array antenna gains in azimuth plane for (a) Configuration A and (b) Configuration B.	81
5.11	Radiation patterns and electric field decomposition in azimuth plane for (a) single element, (b) two elements of configuration A, (c) two elements of configuration B.	84
5.12	2×1 subarray copolar radiation pattern and its decomposition to its even and odd components in the azimuth plane for (a) Configuration A, (b) Configuration B, (c) Configuration B with attenuated odd component.	86
5.13	2× 1 subarray copolar radiation pattern and its decomposition to its even and odd components for Configuration B with attenuated odd component.	87
5.14	2× 1 subarray radiation patterns and their decomposition to even and attenuated odd components for different interelement spacings.	88
5.15	Different 2×2 subarray configurations of proposed crossed dipole, (a) Configuration A, (b) Configuration B, (c) Configuration C, and (d) Configuration D.	89
5.16	Even and odd field components of dual linear polarized crossed dipole antenna for (a) horizontal and (b) vertical polarizations.	90

5.17	16×8 crossed dipole planar array gains in principal planes, (a) Configuration A, (b) Configuration B, (c) Configuration C, and (d) Configuration D.	92
6.1	A double-layered printed dipole antenna integrated with a Marchand balun.	97
6.2	Electric and magnetic sources and their images near (a) electric (PEC) and (b) magnetic (PMC) conductors.	98
6.3	A sample design of a dual-band Electromagnetic Bandgap (EBG) Artificial Magnetic Conducting (AMC) ground plane fabricated at the Pennsylvania State University.	98
6.4	A unit cell of two imaged linear dipole antennas. One pole of each dipole is shown transparent to present the excitation method.	99
A.1	A unit cell of two imaged linear dipole antennas. One pole of each dipole is shown transparent to present the excitation method.	112
A.2	Reflection coefficient of the single dipole antenna as a function of gap distance between the two poles.	112
A.3	Simulated active VSWR in 0°, 30°, and 45° scanning angles.	113
A.4	Antenna prototype after each fabrication process. (a) 3-D printed sample, (b) antenna after electroless plating, (c) final copper coated antenna after electro plating, isolating the excited pole, and soldering of connectors.	114
A.5	Linear array antenna and the radiation pattern measurement set-up.	115
A.6	S-parameter of the middle element in the array.	115
A.7	Measured radiation patterns of the proposed array antenna at different frequencies. (a) 2.7 GHz, (b) 2.85 GHz, and (c) 3 GHz.	117

Abstract

Multifunction Phased Array Radar (MPAR) was defined to investigate the feasibility of integrating weather observation and air surveillance radars into a single network. Weather radars require dual polarization capability which may be also beneficial to aircraft characterization. Research activities have begun to identify challenges, mitigate risk, and demonstrate polarimetric technologies. Ten-panel, developed by MIT's Lincoln Laboratory, was the first dual-polarized planar phased array demonstrator. Alternatively, a cylindrical polarimetric phased array radar (CPPAR) was developed at the Advanced Radar Research Center of the University of Oklahoma to resolve the intrinsic limitations of planar arrays in making accurate polarimetric measurements. The current CPPAR employs a frequency scanning patch array antenna. Since the radar's performance would be the most important driver, the future operational CPPAR, suitable for long-range weather measurement, will utilize a new antenna with higher performance.

It is the purpose of this research to propose a new dual-polarized phased array antenna for MPAR application. A crossed dipole antenna with sufficient operational frequency bandwidth is designed. A high polarization purity is achieved by using a group of efficient techniques in element scale. This element was modified to obtain a higher match between copolar beams. The modified element is utilized as an embedded element to form a cylindrical and a planar

array antenna. It is demonstrated that suppressed azimuthal surface wave and consequently highly matched copolar beams can be achieved in a cylindrical array of proposed crossed dipole. In order to compensate for the electrical and geometrical asymmetry of the element, an imaged arrangement of the elements with respect to the center of the array is utilized. It is shown that a planar array of the modified crossed dipole, arranged in a specific configuration, proposes zero cross-polarization in the principal planes without increased side lobe problem. The experimental verification demonstrates that the proposed phased array antennas are promising candidates for multi-mission applications.

Chapter 1

Introduction

1.1 Multifunction Phased Array Radar

Weather observations and air surveillance share the same principle of detecting electromagnetic wave scattering. Therefore, it would be more cost-efficient and easier to share data if a single radar network were used for multiple missions. It was the basis for Multifunction Phased Array Radars (MPAR) initiated by a joint effort between the National Oceanic Atmospheric Administration (NOAA) and the Federal Aviation Agency (FAA) [1]. A life-cycle cost savings of approximately \$5 billion was estimated in the initial reports. Besides that, it was operationally efficient to perform all these missions with a single system. The project received great attention and researches have started to investigate the feasibility of replacing four networks 1) National Weather Surveillance Radars (WSR-88D or NEXRAD); 2) Terminal Doppler Weather Radars; 3) Airport Surveillance Radars; and 4) Air Route Surveillance Radars, all shown in figure 1.1, with a single scalable architecture.



(a)



(b)



(c)



(d)

Figure 1.1: Aircraft surveillance and weather radar networks, (a) Airport Surveillance Radars, (b) Terminal Doppler Weather Radars, (c) Air Route Surveillance Radars, (d) National Weather Surveillance Radars.

1.2 Phased Array Radar (PAR)

The flexibility of the phased array radar justifies its utilization in performing missions for both weather sensing and route surveillance. Phased array radars with electronic scan capability allow for faster data update [2] and thus the observation of evolutions of severe storm phenomena. Its high precision in detection of point targets may also be beneficial to aircraft surveillance. Unlike 5 min mechanical volumetric scan, a phased array radar could complete

the same mission on the order of the seconds which is required by aircraft surveillance. Added to these is the possibility of adaptive scanning, where the echoes are used to reallocate radar resources, adjust the scanning scenario, and change the waveform in response to what had been observed. A phased array antenna, backed by a compatible backend, can effectively perform an agile beam forming. These features indicate that phased array antennas could be promising candidates for MPAR project.

1.3 Polarimetric Phased Array Radar (PPAR)

Weather radars, such as WSR-88D, have been upgraded to dual polarization capability which enables them to estimate the observables more precisely [3]. The shapes of raindrops change with their sizes, providing different horizontally and vertically polarized returns [4]. The ratio of these orthogonal returns, referred to as differential reflectivity, is a function of the diameter of the target. Therefore, weather radar can obtain more information on the type of hydrometer by using a pair of orthogonally oriented polarization rather than a single polarization. Such a feature could also be advantageous to aircraft characterization, clutter suppression, and detection and tracking of small targets. Research activities have begun in academia and industry to identify challenges, mitigate risk, and demonstrate polarimetric technologies for both weather and airport surveillance. The C-band Spaceborne Imaging Radar and the X-band Synthetic Aperture Radar missions are conducted by a joint U.S./German/Italian Space Agency effort, where polarimetric phased-array radars are built by JPL and the Ball Communication Systems Division [5]. An Airborne Synthetic Aperture Radar is also conducted by NASA/JPL for weather imaging with full-polarization radars.

1.4 Phased Array Antennas for MPAR

The principles of the phased array antenna was discovered early in the nineteenth century, matured over the past decades, and evolved into numerous designs and topologies [2]. However, the MPAR seeks a solution with dual linear polarization capability. This introduces an additional challenge to antenna designers, as a high separation between two orthogonal radiation patterns (polarization isolation) is required. For instance, in weather observation, the intrinsic differential reflectivity Z_{DR} values range from about 0.2 dB for drizzle and dry snow, to 3–4 dB for heavy rain and large drops. Therefore, it is desirable that the measurement error for differential reflectivity be about 0.2 dB. In addition, to distinguish between rain and melting snow, the error of the copolar correlation coefficient (ρ_{hv}) must be less than 0.01 [4]. These Z_{DR} and ρ_{hv} requirements can be translated to antenna parameters as 40 dB polarization isolation and higher than 99% match between horizontal and vertical copolarization patterns, respectively. Such accuracies were satisfied by dish antennas for decades, however, this becomes a challenging task for PPAR.

When research activities on the MPAR started, there was no “off the shelf” antenna characterized for dual linear polarization performance. Therefore, the joint FAA/NOAA government released contracts with academia, industry, and national laboratories to investigate and design solutions based on the architecture of their preference. Various alternative antennas, with distinct advantages and disadvantages, were designed and the MPAR stringent requirements were addressed.

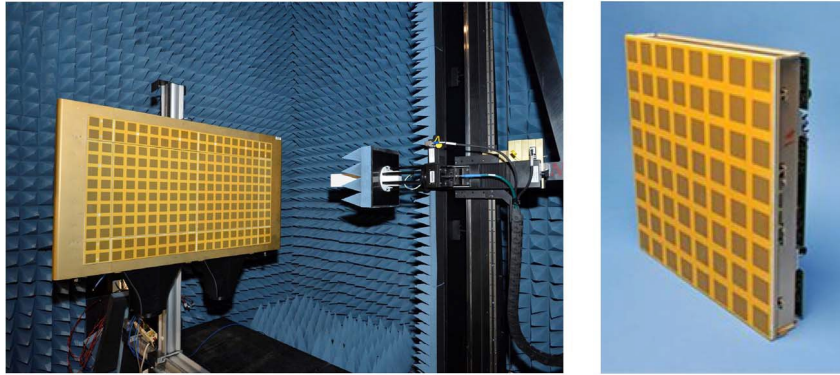


Figure 1.2: (Right) 8 by 8 dual polarized subarray panel. (Left) Two-panel subarray used to demonstrate overlapped beamforming (From [1]).

1.4.1 Planar Polarimetric Phased Array Radar (PP-PAR)

Ten-panel, as shown in figure 1.2, is actually blocks of 8 by 8 dual polarized patch antennas designed by the MIT's Lincoln Laboratory. The blocks are arranged side-by-side, forming a planar phased array antenna. Fabricated by printed circuit technology, the Ten-panel solution is cost-effective, and also allows for the compact integration of T/R modules at the back of the antenna. The first dual polarized planar antenna showed promising results in the experiment.

A serious challenge in polarimetric measurement is maintaining a high polarization isolation within the whole volumetric scan. That is, two beams must be orthogonal over the entire scanning scenario which is not easily achieved by a planar phased array antenna. When the transmit beam is directed off the principal plane, the two polarized beams are not orthogonal and the horizontal (vertical) polarization is not parallel (perpendicular) to the surface of the earth. Such an effect causes part of the horizontally oriented power to be returned in the vertical beam and vice versa. This bias can be compensated

through costly and cumbersome calibration, but at the cost of a decrease in the sensitivity [6]. Although the PPPAR is feasible for MPAR, it is not necessarily the best solution for weather measurements due to its intrinsic scanning limitations [6].

1.4.2 Cylindrical Polarimetric Phased Array Radar (CPPAR)

A cylindrical polarimetric phased array radar (CPPAR) was developed at the Advanced Radar Research Center (ARRC) of the University of Oklahoma. The cylindrical array, which is shown in figure 1.3, is divided into four quadrants, each covering a 90° sector of volume. The main idea for this structure is the commutating in the azimuth direction rather than scanning. That is, each quadrant can be rotated electronically around the cylinder. Therefore, the array beam, which always faces the broadside directions, allows for high polarization purity and invariant azimuth scan. This is achieved at the cost of complexity of the structure. While the main concept of the CPPAR has been demonstrated [6], its related issues are still being studied. The main challenges are achieving a low cross-polarization level, high isolation between two polarizations, and matched horizontal and vertical copolar beams [6].

1.5 Motivation for Dissertation and Research Objectives

The current CPPAR demonstrator is populated by a frequency scanning linear array antennas which is depicted in figure 1.4. Like Ten-panel, CPPAR utilizes compact patch elements into its linear columns of the array antenna. Each

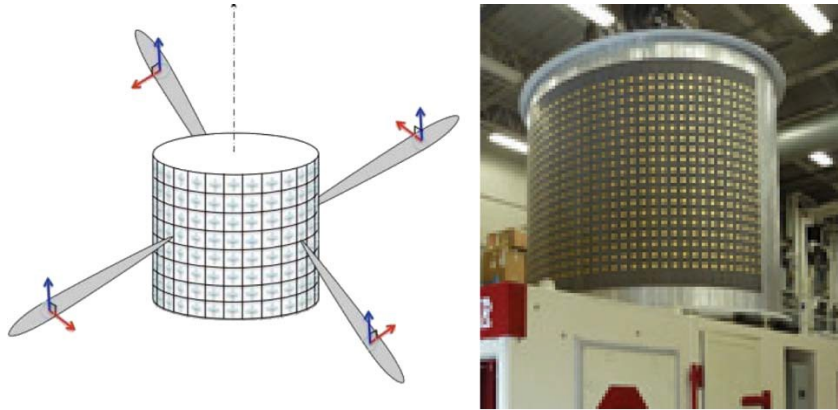


Figure 1.3: (left) Cylindrical array schematic with four dual polarized beams transmitting simultaneously. (Right) Cylindrical Polarimetric Phased Array Radar demonstrator (From [4]).

linear array is excited by a single T/R module, reducing cost and complexity of the design. Scanning in the elevation direction is carried out by changing the frequency, which in turn adjusts the phase difference between adjacent vertical elements. While the current CPPAR shows promising weather measurement capabilities, its performance can be modified by individual excitation of each element. Such a cylindrical radar, capable of long-range measurement, will benefit the weather community by providing adaptive beam forming based on the features of echoes bouncing off the target. To cover the whole frequency range, required by MPAR, a multilayer stacked patch antenna was utilized in the current CPPAR. Such a thick grounded substrate is a proper medium for the azimuthal surface wave to travel around the cylinder and radiate. This effect changes the shape of the copolarization patterns, causing mismatch between the vertical and horizontal copolar patterns. An alternative antenna element with removed substrate over the principal ground plane can suppress the azimuthal surface wave, resulting in a higher match between copolar patterns. Finally, a higher performance in terms of the side lobe level of array antenna could be achieved by using a symmetrical antenna element with re-

spect to its center. Therefore, the need for an alternative phased array antenna has arisen.



Figure 1.4: 19-element frequency scanning antenna array under test in the Federal Aviations Administration (FAA) anechoic chamber (From [6]).

1.6 Outline of Dissertation

This dissertation is devoted to design and characterization of a new phased array antenna whose performance satisfies the strict MPAR requirements. Following the introduction, Chapter 2 compiles and summarizes research activities related to dual polarization antennas for a broad range of applications. Various cross coupling mechanisms between orthogonal polarizations will be specifically discussed and related to port isolation as part of this contribution to a growing body of knowledge. Techniques to suppress these components will be discussed in the context of example antennas. It is found that the use of simple and symmetrical structures is advantageous to antenna polarization purity. The techniques, discussed therein, can be integrated into future antennas with higher performance, opening the door for new application spaces such as phased array weather radar and precise polarization control for communication systems.

Following the points mentioned in Chapter 2, a crossed dipole antenna with symmetrical geometry is proposed in Chapter 3. The reasons for choosing such

an element are emphasized. The coupling mechanisms between different parts of the orthogonal polarizations are discussed in detail. This is followed by a parametric study of the dimensions of the proposed antenna, showing its versatility in operating over a wide frequency range with the desired bandwidth. Fabrication process and measurement set-up are provided, and the simulation results are verified by experiment. Looking for more symmetry between the two polarizations, we modified the proposed crossed dipole in a new version of the antenna. Highly matched copolar patterns, obtained through utilizing identical radiation elements, is discussed.

Chapter 4 addresses the characterization of a linear crossed dipole, made by the above-mentioned antenna. This linear array is developed to replace the current frequency scanning antenna on the CPPAR. Dimension adjustments of the crossed dipole in the linear array environment will be discussed. This is followed by the scanning assessment of the linear array and finalizing the interelement spacing. A specific arrangement of the elements in the array configuration is presented. The suppressed cross-polarization level is verified by measurement results. Another focus of this chapter is the characterization of the cylindrical array radiation pattern. Phase mode analysis is utilized in order to extract the embedded element pattern of the antenna in a cylindrical array. Such a pattern, in conjunction with coherent addition in Matlab, is utilized to form the final pattern of the cylindrical array antenna.

Chapter 5 studies a planar crossed dipole array antenna. The dimensions of the element are finalized, using the periodic (Master/Slave) boundary condition in the HFSS. The desirable performance of the antenna in scanning to severe angles is demonstrated and is followed by a parametric study of the antenna dimensions. Four possible imaged configurations are applied to the

planar array arrangement, and the reduced cross-polarization levels are discussed. A side lobe issue with imaged patch antenna array is discussed and related to 2×2 subarray radiation pattern $\overline{E}_{2 \times 2}(\theta, \varphi)$. The requirement of the element radiation pattern to eliminate the increased side lobe is theoretically calculated. A condition for the magnitude of the odd copolar component is specified, which can be expanded to any other type of antenna in order to examine whether they suffer from the side lobe issue. It is shown that the simple crossed dipole array, arranged in a specific configuration, can provide zero cross polarization in both principal planes while it has no increased side lobe issue.

Finally, Chapter 6 will give a brief conclusion that highlights the research contributions. We will introduce potential modifications and suggestions for the future direction of the phased array antennas. These will open up additional research activities within the antennas and propagation community.

Chapter 2

A Review of Dual-linear Polarized Antennas

2.1 Introduction

This section compiles and summarizes research activities related to dual polarization antennas for a broad range of applications. Existing dual polarization antennas are categorized into three separate groups according to their topologies. Some representative antennas of each group are presented and their performance are compared in terms of port isolation, cross-polarization, frequency bandwidth, dimension, and complexity. As the main focus of this section, the port isolation and the polarization purity are discussed in detail and the techniques to enhance them are discussed. The techniques, discussed herein, can be integrated in future antennas with higher performance, opening the door for new application spaces.

2.1.1 Interaction Between Two Radiation Elements in a Dual Polarization Antenna

To specify how well a dual-polarized antenna separates its two polarizations, some criteria should be defined. Port-isolation and cross- to copolarization level are considered as measures of coupling between ports and patterns of

two polarizations, respectively. A common framework of interaction between the radiation elements in a dual polarization antenna will help us to properly understand the source of the port isolation and the cross-polarization. Figure 2.1 represents a scenario of two distant orthogonal radiation elements, where the separation between elements is exaggerated to show their interaction clearly. To simplify the problem, each element is assumed to be lossless and radiate linearly with no cross-polarization. Under these circumstances, part of the power (P_a) delivered to element A is effectively radiated (P_{ra}), and a fraction of the delivered power is directed toward the element B (P_x). While the former accounts for intended copolar radiation of the antenna A, the latter is a source of cross coupling to element B. From P_x power partially goes toward port B (P_b), which determines the port isolation and partially reradiates (P_{rb}), which contributes to the cross-polarization radiation, as in most of the dual polarized antennas, the elements are located at right angles to one another. Therefore, the cross coupling (isolation), the port-to-port coupling (isolation), and the cross-polarization in a dual polarized antenna can be defined as

$$\text{Cross Coupling : } C_x = \frac{P_x}{P_a} \quad (2.1)$$

$$\text{Port Coupling : } C_{ba} = \frac{P_b}{P_a} \quad (2.2)$$

$$\text{Cross Polarization : } XP = \frac{P_{rb}}{P_{ra}} \quad (2.3)$$

The port isolation, frequently mentioned in the literature, is the magnitude of the port coupling expressed by (2) in dB scale. From the discussion above, it is clear that the interaction between the radiation elements mainly comes from the cross (transverse) coupling P_x (C_x), and reducing it will result in reduction of both port coupling P_b (C_{ba}) and cross polarization P_{rb} (XP). The

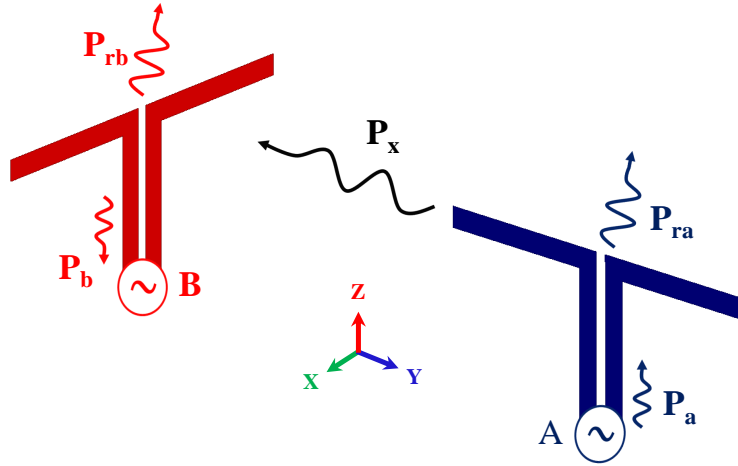


Figure 2.1: Interaction between two radiation elements in a dual polarized antenna.

techniques proposed in the literature to reduce the transverse coupling (C_x) can be summarized as below:

- Blockage
- Null location
- Distant elements.

A detailed discussion of these techniques will be provided in the following sections wherever an antenna using any of the techniques is introduced. Figure 2.1 represents ideal elements with no cross-polarization. However, in practice, the element A itself exhibits some level of the cross-polarization which adds to that radiated from antenna B. Accordingly, choosing elements with inherently low cross-polarization enhances the overall polarization purity of the dual-polarized antenna.

2.2 Similar Orthogonal Elements - Group I

The simplest solution to design a dual-polarized antenna is to duplicate a radiation element and position it at a right angle to the original one. The matched

beams obtained through utilizing identical radiation elements is advantageous in many applications such as MIMO and weather observations. In addition, such a symmetry in both polarizations serves the antenna to show low port coupling (P_b). Crossed dipole and crossed slot are the classical representatives of this category, widely proposed and discussed in the literature.

2.2.1 Crossed Dipole

The roots of crossed dipoles track back to the 1930s, when the first crossed dipole named turnstile antenna was proposed by Brown [7]. Since then, modifications with emphasis on broader impedance bandwidth, profile miniaturization, and higher isolation have been proposed [8]. A crossed-dipole is originally a pair of half-wavelength dipoles aligned at right angles to each other. Different dipole excitations include half-wavelength balun [9], Γ -shaped strips [10], and direct coaxial cables [11].

The cross coupling (C_x), discussed earlier as the major interaction between the orthogonal radiation elements, might happen between any two parts of the orthogonal polarizations. Specifically, for a crossed dipole, the cross coupling might happen between the baluns or the dipoles of the two polarizations, denoted by C_{bb} and C_{dd} , respectively.

The coupling between dipoles (C_{dd}) is discussed in figure 2.2 where a vertical dipole is differentially excited. This figure represents how the null locus, mentioned earlier, allows the cross dipoles to retain minimum interaction between the orthogonal elements (C_x). It is known that at any time electric charges of opposite polarity are located on the facing poles of the vertical dipole. It produces a potential distribution with alternating positive and negative values at the upper and lower hemispheres, shown in blue and red colors

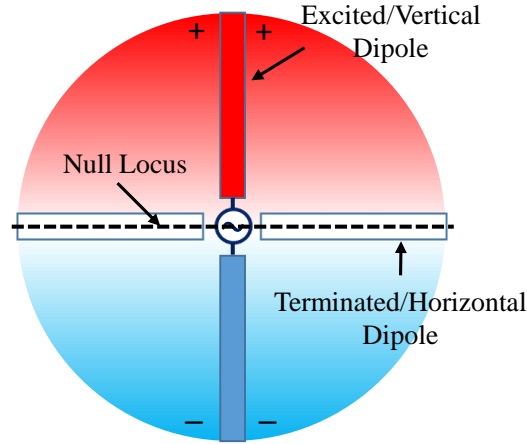


Figure 2.2: Voltage distribution of an excited vertical dipole and null locus representation.

in figure 2.2. If the dipole possesses two identical poles (geometrical symmetry) and is also excited by ideal differential signal (electrical symmetry), a null locus with zero potential appears along the bisector of excited dipole which can be considered as a virtual AC ground plane. Whatever lies along this line, including the horizontal dipole, experiences no coupling from the vertical dipole. This explains why an ideal crossed dipole shows theoretically zero interaction ($C_{dd} = 0$) between two dipoles. It is worth noting that the null locus can be shifted from equator if either electrical or geometrical symmetry is disturbed. These two cases which are prone to some cross coupling are discussed in the following.

The balun-to-balun coupling, C_{bb} , could significantly account for cross coupling between elements (C_x), as the baluns are often oriented parallel to each other. Therefore, any current on a balun can be coupled to the other one and vice versa. Figure 2.3a represents how blockage can reduce the balun-to-balun coupling (C_{bb}). A dual-polarized magneto-electric dipole antenna is depicted which is basically a realization of a complementary antenna with a fairly larger frequency bandwidth compared to the conventional dipole [12]. Each folded

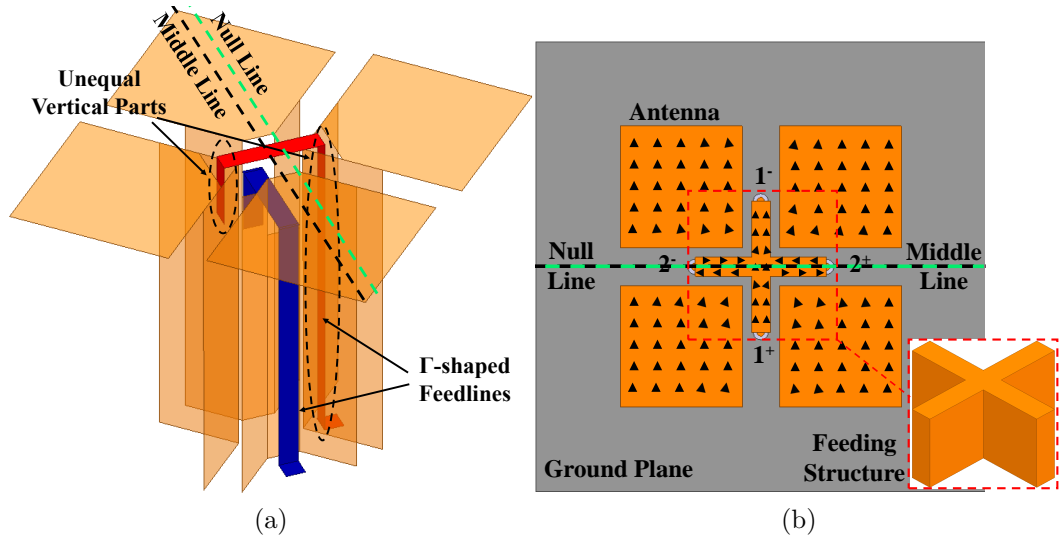


Figure 2.3: Dual-polarized magneto-electric dipoles, (a) Γ -shaped feedlines (Concept from [12]) , (b) differential excitation along with current distribution on antenna (Concept from [8]).

dipole provides a separate room for its respective Γ -shaped feedline and isolates it from its counterpart coupling. The single-ended Γ -shaped feedline is geometrically asymmetric with respect to the center of the antenna owing to its unequal vertical parts. Such a geometrical asymmetry shifts the null locus from the middle line of the antenna, as shown in figure 2.3a. It is resolved in figure 2.3b, where a symmetrical differential driven antenna is shown [8]. The geometrical symmetry, disturbed by the Γ -shaped feedline, no longer exists in this differential driven antenna. The null locus occurs along the middle line and lower cross coupling (C_x) is achieved.

Regardless of whether a crossed dipole is excited differentially or by a Γ -shaped feedline, it is difficult to achieve ideal differential signals within the entire frequency bandwidth. The phase imbalance of the baluns or feed networks, is often optimized at a center frequency, and increases toward the beginning and the end of the frequency bandwidth [13]. Consequently, the null line of the excited dipole is disturbed from the equator at these margin fre-

quencies. Such an electrical asymmetry causes coupling between orthogonal dipoles (C_x). The differential excitation has a superior performance compared to single-side excitation while electrical asymmetry results in a disturbance of the null locus. The current distribution when differential port 1 is excited is depicted in figure 2.3b. Differential port 2, consists of two separate ports, 2^- and 2^+ . Both mentioned ports are equally coupled to the orthogonal element and the out of phase couplings cancel each other. That is, in spite of some cross coupling (P_x), occurring between orthogonal elements, the ports remain decoupled (P_{ba}). Differential feeding adds a level of complexity to the design as it requires a feed network with differential signals at their outputs.

2.2.2 Crossed Slot

Slot antennas are considered complementary elements to the dipoles since both have similar radiation patterns [14]. Contrary to the dipole antennas, which should be located a quarter wavelength above the ground plane, the slot antennas lie on the ground plane, resulting in a more compact profile, hence lower cross-polarization. On the other hand, slot antennas have narrower frequency bandwidth compared to that of the dipoles. Two crossed slot antennas with single-ended [15] and differential excitation [16] are discussed below.

Figure 2.4a shows a crossed slot antenna where they are etched on the sides of a cuboid and excited by an open-ended microstrip lines [15]. Considering the horizontal slot as a complementary metal antenna excited in the middle [14], one can specify the null locus along the middle line as shown in figure 2.4b. The coupled currents from the horizontal slot to the vertical slot, when the former is excited in its center and the latter is terminated, is depicted. It is shown that the coupled currents along the radiating edges of the vertical slot

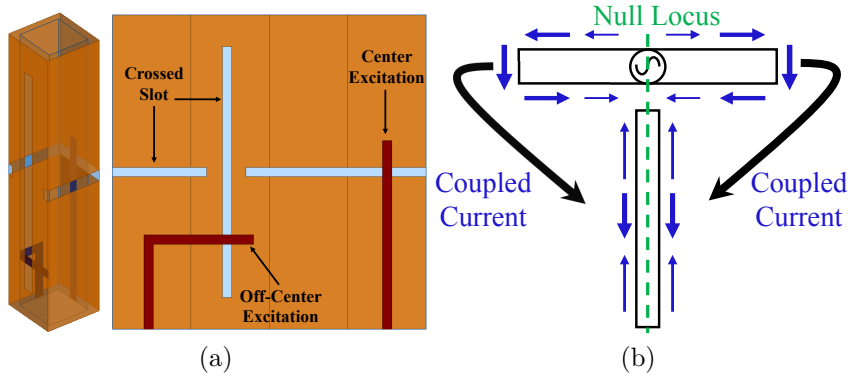


Figure 2.4: A crossed slot excited with open-ended microstriplines, (a) 3-D and expanded views of the antenna (Concept from [16]), (b) coupled currents from the horizontal slot to the vertical one.

are of the same amplitudes and phases and cannot excite it. Therefore, the slots remain decoupled. Any deviation from above symmetry introduces some cross-coupling (P_x) between slots. It occurs for this design because of its offset excitation of the vertical slot. Such coupling adds to the coupling between feedlines placed in proximity which resembles the balun-to-balun coupling in the crossed dipole.

A dual polarization crossed slot with high performance is illustrated in figure 2.5a [16]. Combination of different techniques, incorporated into the design, accounts for its high port isolation (P_{ba}) and low cross polarization. Each differential port lies along the null locus of the other polarization. Four diagonal strips and four diagonal slots are etched on the top and bottom of the substrate, respectively, which block the transverse coupling (P_x). The symmetrical design and differential excitation guarantees minimum port coupling (P_{ba}) in times of electrical asymmetry. The magnetic current densities when port 1^+ and port 1^- are individually excited with opposite phase are shown in blue and red in figure 2.5a, respectively. It is evident that the upper and lower slots carry currents with the same directions which contributes to copo-

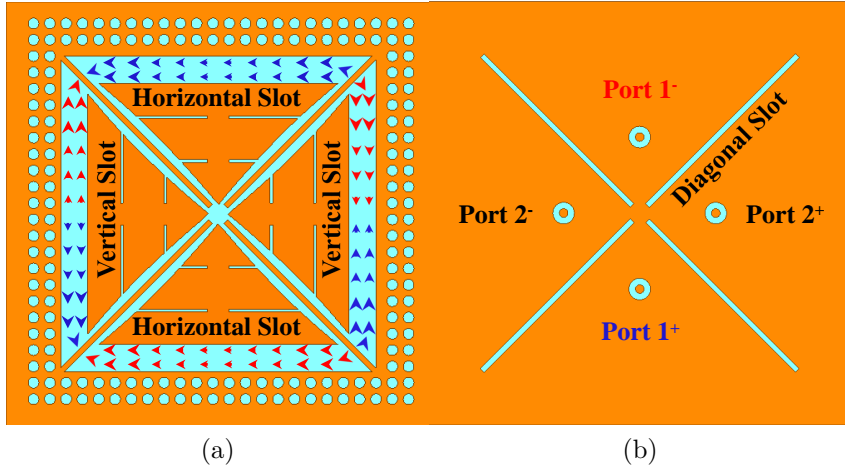


Figure 2.5: A differential excited crossed slot, (a) top view of the antenna along with magnetic current distributions, (b) bottom view of the antenna (Concept from [16]).

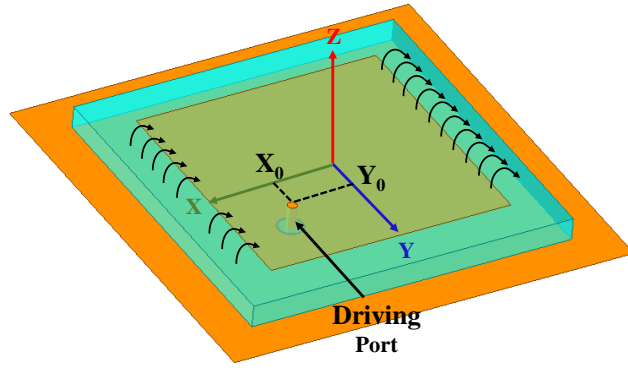
Table 2.1: A comparison of the performance of antennas in group I.

Ref.	Freq. BW (GHz)	Port Isolation (dB)	X-pol (dB)	Dimensions (mm) Length×Width× Height
[12]	1.7-3.4	>36	>-19	64.6×64.6×27
[8]	0.95-1.92	>36	>-23	122×122×48
[9]	2.6-3.04	>52	>-38	55×55×72
[15]	2.34-2.49	>32.5	>-12	12×12×42
[16]	2.51-2.69	>40	>-26.4	57.5×57.5×3.04

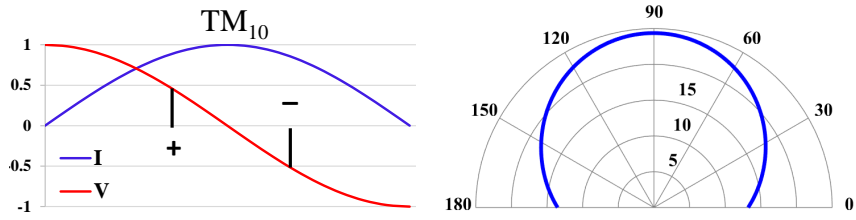
larization components. On the other hand, the vertical slots have currents mirrored with respect to the horizontal bisector of the antenna and in the opposite directions. Hence, the cross-polarization components resulted from these currents add destructively in the principal planes. Table 2.1 compares the performance of the antennas mentioned in this category in terms of measured dual polarization parameters. The cross-polarization is provided within $\pm 90^\circ$ from broadside in the principal planes which are normalized to the peak of copolarization.

2.3 A Patch Antenna With Two Orthogonal Modes - Group II

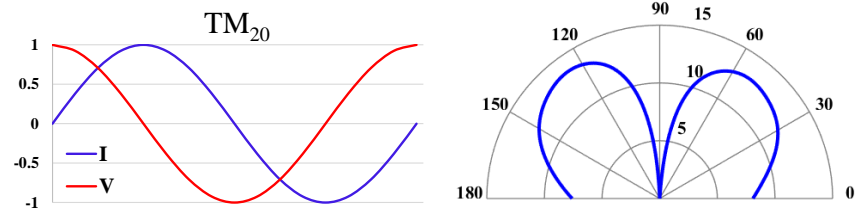
Two orthogonal modes, each corresponding to an individual polarization, can be excited underneath a patch antenna [17]. This, in turn, results in the radiation of two orthogonal polarized waves near the broadside direction forming a dual linear-polarized antenna. Various configurations with orthogonal modes are reported in the literature [18]. However, herein we mainly consider a square patch antenna with dominant orthogonal modes, i.e. TM_{01} and TM_{10} . These antennas make up a large percentage of proposed dual-polarized antennas [19] and their main advantages lie in their symmetry of structure, compactness, easy and inexpensive fabrication process. Along with two dominant modes, other undesired modes can also be stimulated beneath the patch. Degrading the antenna performance, they are considered as sources of port coupling and cross-polarization radiation [20]. In this section, the microstrip patch antennas are categorized according to their excitation methods, and the techniques to suppress the higher-order modes and enhance the port isolation are discussed. A square patch antenna with driving port at an arbitrary point (x,y) is shown in figure 2.6a. Current and voltage distributions related to the first three order modes in the x-direction, i.e. TM_{10} , TM_{20} , TM_{30} along with their corresponding radiation patterns are also illustrated. To excite the dominant TM_{10} mode, a 50Ω excitation port should be located on either side of the middle line (y -axis) with an offset from it. The modal expansion technique indicates that along with TM_{10} , the higher order modes in the same (TM_{n0}) and the transverse directions (TM_{0n}) can also be excited [21]. While the same directed modes make some minor ripples on the copolarization, the transverse modes are the source of the cross coupling and the cross-polarization radiation. Let



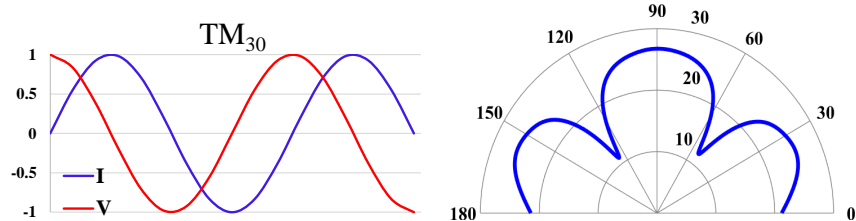
(a)



(b)



(c)



(d)

Figure 2.6: A square patch antenna, (a) driving port at arbitrary point (x,y) , (b) TM_{10} fields distributions and copolar pattern, (c) TM_{20} fields distributions and copolar pattern, (d) TM_{30} fields distributions and copolar pattern.

us examine a particular case of driving point located along the middle line of the patch (x -axis). The x -axis is specified as the null lines and the infinite lines of the odd and even y -directed modes, respectively, and such transverse modes

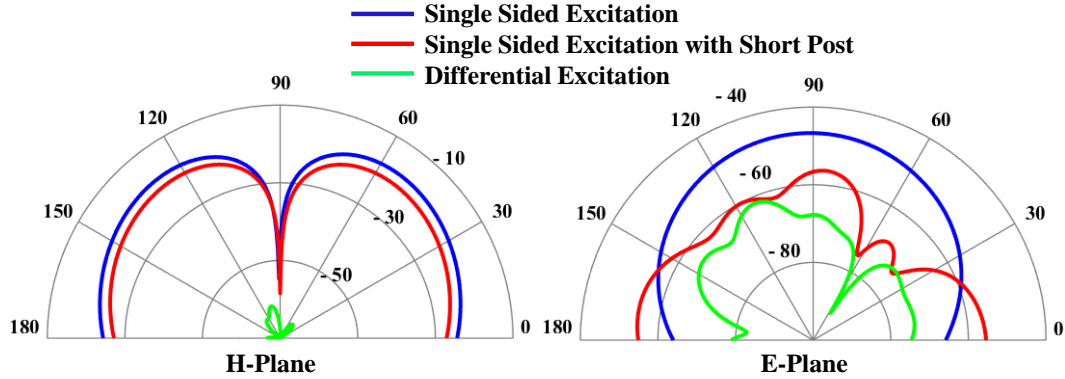


Figure 2.7: Cross polarization comparison of antenna in [23] in principal planes with different excitation schemes.

are equally mismatched to the port input impedance. Accordingly, locating the input port along the middle line of the patch (x-axis) suppresses the transverse modes and provides the lowest possible cross-polarization. Regarding the cross-polarization of a square patch antenna different analysis were reported. Reference [22] introduces the TM_{02} as the origin of the cross-polarization radiation in such antenna. If that is the case, a short post at the center of the patch, where the impedance of even modes are infinite, can suppress them in both orthogonal directions. Reference [23] indicates that even in single mode (TM_{10}) operation, the asymmetry of the probe location results in disturbance of ideal field distribution, causing high cross-polarization in the H-plane. To suppress the higher order modes and simultaneously preserve the geometrical symmetry of the antenna, differential excitation is proposed in [23]. How it matches the TM_{10} mode and attenuates the higher order ones can be realized by comparing the field distributions of different modes in figures 2.6b-2.6d. The same patch antenna in [23] was simulated with differential scheme and short post and their suppressed cross polarizations are compared with common single-sided excitation in figure 2.7. Similar to previous category, the cross coupling (C_x) in dual-polarized patch antenna can be examined in terms

of its main contributors. In such antennas, each feeding mechanism along with all respective propagation modes in each direction comprise a single polarization. Therefore, the cross coupling between two polarizations can occur either directly between feeding mechanisms, or between orthogonal modes, denoted by C_{ff} and C_{mm} , respectively. Positioning input port along the null locus in order to avoid power being leaked to the transverse modes (C_{mm}) was discussed and is common to all excitation methods. The coupling between feeding mechanism (C_{ff}) will be addressed in each section a feeding method is discussed.

2.3.1 Microstrip-fed Dual-polarized Patch Antennas

The microstrip feedline is the simplest and the most compact way of exciting a microstrip patch antenna. It includes two single metal layers where the microstrip line and the patch antenna are printed monolithically on a common board. However, it suffers from spurious radiation from the microstrip feed lines which degrades the polarization purity [24]. Such effect dominates in wide bandwidth antennas where the substrate thickness is increased. A microstrip line can excite a patch antenna either on the edges (figure 2.8a) [25] or at the corners (figure 2.8b) [26]. A nearly 20 dB isolation of edge-fed patch antenna is improved to almost 30 dB by using wire bonds which allow for higher modes suppression [25]. It has been analyzed and experimentally verified in [26] that the corner-fed dual-polarized patch exhibits an isolation about 10 dB better than that of the edge-fed patch antenna. Both these samples utilize single-sided excitation associated with each polarization. The asymmetry of single-sided excitation in an inset-fed patch antenna and the disturbance of the patch rectangular shape were discussed in [27]. Such an asymmetry yields

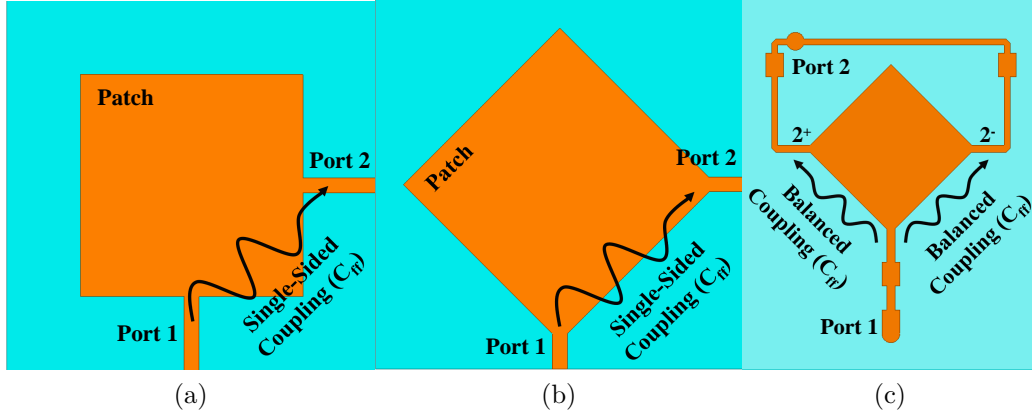


Figure 2.8: Dual-polarized microstrip-fed patch antennas, (a) edge-fed excitation (Concept from [25]), (b) corner-fed excitation (Concept from [26]), (c) differential excitation (Concept from [28]).

Table 2.2: A comparison of the performance of microstrip-fed dual-polarized antennas in group II.

Ref.	Freq. BW (GHz)	Port Isolation (dB)	X-pol (dB)	Dimensions (mm) Length×Width× Height
[25]	3.75-3.95	>30	NA	24×24×0.508
[26]	5.95-6.05	>30	NA	15×15×0.8
[28]	6.5-6.65	>34	NA	14×14×1.57

distorted copolarization and increased cross-polarization. The high cross coupling (C_x) partly occurs between microstrip lines themselves (C_{ff}). A way out of this issue is balanced coupling proposed by differential excitation as shown in figure 2.8c [28]. Suppression of the higher order modes in the corresponding direction along with balanced feeding end up enhanced polarization purity provided in Table 2.2. The two strips of differential feeding along with the patch antenna make a loop-shape structure as it is shown in figure 2.8c. Therefore, the implementation of two differential-fed microstrip line in a single layer without overlap is impossible.

2.3.2 Probe-fed Dual-polarized Patch Antennas

A patch antenna can be excited by a coaxial probe beneath the patch which eases the impedance matching [17] and has lower cross polarization compared to the microstrip line excitation. The latter is achieved owing to identical geometry of radiating slots on either side of the patch and preserving its rectangular shape. However, the increased length of the probe can be problematic in wideband applications [29]. These issues and their possible remedies will be discussed in the following. Size reduction is achieved in a slotted dual-polarized patch antenna shown in figure 2.9a, which modifies the fields distributions, hence the frequency and radiation patterns of the operating modes [30]. This is the simplest probe-fed excitation, where placing each probe on the null locus of transverse modes yields high port-isolation. The symmetrical pattern of the slots results in the identical transverse currents and thus cross-polarization cancellation in both principal planes. This antenna has a narrow frequency bandwidth. The performance of such excitation is degraded in wideband applications where a thick substrate is utilized. The increased length of the probe with inductive features disturbs the impedance matching. Analysis of other issues requires probe characterization. In [31] and [32], the excitation probe is respectively modeled as a short monopole and dipole antenna immersed in the substrate. In either case, these parallel feeds positioned in close proximity in a dual polarized antenna is susceptible to some direct coupling between them (C_{ff}) and this dominates as the thickness of the substrate increases. In addition, the probe's leakage radiation is observed in terms of raised crossed-polarization in the H-plane and distorted copolarization in the E-plane [31]. Luk *et al.* suggested an L-shaped probe to concurrently achieve wider frequency bandwidth and lower cross-polarization [33]. The former is attained

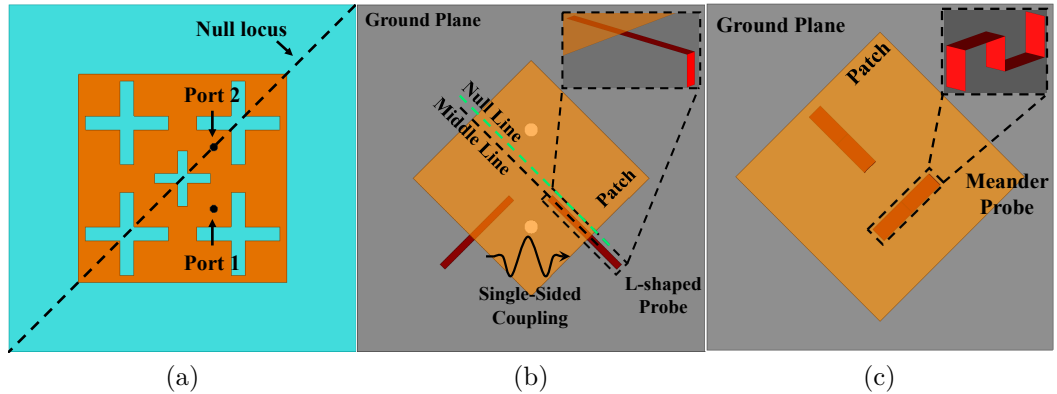


Figure 2.9: Dual-polarized probe-fed patch antennas, (a) simple probe excitation (Concept from [30]), (b) L-shaped probe excitation (Concept from [33]), (c) meander probe excitation (Concept from [34]).

by the horizontal portion of the probe making an open circuit stub of length less than a quarter wavelength. Such capacitive effect compensates for the inductance of the vertical portion of the probe, making a resonant frequency close to that of the TM_{01} mode of the patch. The lower cross-polarization is attributed to shortening the probe vertical portion. Figure 2.9b shows a dual-polarized antenna fed by L-shaped probes [35]. Of importance is the wide bandwidth of the antenna provided in Table 2.3. As discussed earlier, the geometrical asymmetry of the single-sided excitation with respect to the center of the patch disturbs the normal distribution of the dominant TM_{01} mode, resulting in displacement of the null locus from the center line of the patch. This effect, as seen in figure 2.9b, causes some cross coupling between two polarizations. It adds to direct single-sided coupling between feedlines (C_{ff}) which is stronger in L-shaped probes since they have longer dimensions compared to that of a simple probe. This larger dimension is shown in figure 2.9b, where the vertical portions are placed out of the patch to prevent the overlap and the horizontal portions extend underneath the patch. Later, we will compare such performance with a same patch with differential excita-

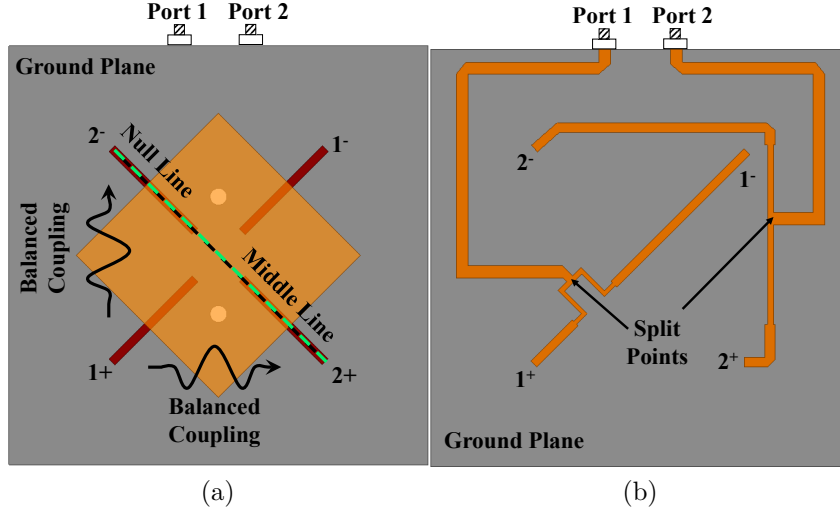


Figure 2.10: A dual-polarized differential driven antenna. (a) Patch and L-shaped probes, (b) Differential feed network (Concept from [33]).

tion. The open circuit quarter-wavelength horizontal portion of the L-shaped probe was replaced by a half-wavelength one shorted to the antenna on one side [34]. The new feed allows for lower cross-polarization due to a pair of out of phase vertical currents on either side of the antenna which resembles a balanced feed excitation in the antenna's E-plane. Such long feeding is not applicable to dual-polarization performance. Therefore, the half-wavelength stub is meandered [36] in a compact profile at a modest increase in the cross-polarization. Figure 2.9c depicts a dual-polarized antenna fed by meander probes. The increased length of the probes increases the chance of the coupling between them (C_{ff}). Moreover, the antenna's performance is limited by its poor polarization purity. Meandering is not a precise process and often results in fabrication tolerances [36]. To implement the meandering precisely, the vertical and horizontal portions of the probes could be respectively replaced by precise plated blind vias and microstrip line strips, which remains as a future research. To compare the performance of single-sided and differ-

Table 2.3: A comparison of the performance of probe-fed dual-polarized antennas in group II.

Ref.	Freq. BW (GHz)	Port Isolation (dB)	X-pol (dB)	Dimensions (mm) Length×Width× Height
[30]	0.852-0.858	>30	>-32	67.056×67.056×NA
[35]	1.71-1.88	>20	NA	77×77×21
[36]	1.68-2.04	>30	>-15	61×61×17.5
[35]	1.65-1.98	>30	>-10	92×92×22.5

ential excitations, a dual-polarized differential driven antenna with L-shaped probe [35] is provided in figure 2.10a. Suppression of the higher order modes guarantees the single mode operation. In addition, symmetrical locations of two probes with respect to the center of the patch preserves the geometrical symmetry, hence normal distribution of the dominant TM_{01} mode. Therefore, the null locus, as shown in figure 2.10a, is returned to the middle line of the patch and lowest cross coupling occurs between two polarizations. In times of electrical asymmetry, the same balanced couplings experienced phase reversal cancel each other. Finally, the leakage radiations from two vertical portions, with the same amplitudes and reverse directions, cancel in the far-field [31], resulting in lower cross-polarization. Compared by the same authors of [35], 10 dB isolation improvement is contributed by the differential excitation. Differential excitation is advantageous in theory but difficult to implement. The feed network for the above antenna is shown in figure 2.10b. The space to accommodate the half-wavelength delay line for each polarization enlarges the antenna profile. Feed network can affect the symmetry and polarization purity of differential driven antenna. In figure 2.10b, the feed network lies in an extra layer beneath the ground plane which blocks the feed spurious radiation. To further reduce the feed-to-feed coupling (C_{ff}) in figure 2.10b, the lengths of

the feedlines from the input ports to the split points can be minimized and the input ports can be located as far away as possible. Therefore, an optimum design of feed network provides the antenna with better performance which remains as future research activities.

2.3.3 Aperture-coupled Dual-polarized Patch Antennas

D. M. Pozar introduced the aperture-coupling excitation method [37], where the radiating patch is coupled to a feedline through a slot etched in the ground plane. The feed network is implemented in a separate layer underneath the ground-plane which blocks the interference between the antenna radiation and the parasitic radiation of the feedlines [37], resulting in pure radiation of the antenna. Having an extra layer compared to the previous excitations, hence an extra transverse coupling mechanism, C_{ss} , named slot-to-slot coupling is introduced to the dual-polarized antenna. In such a feeding scheme, C_{ss} and C_{ff} are functions of both feedlines and slots characteristics such as their shapes, lengths, positions with respect to the center of the patch, and their relative orientations with respect to each other. These issues are addressed in the following.

A dual-polarized antenna, proposed by Adrian and Schaubert in 1987, is illustrated in figure 2.11a [38]. Two rectangular slots corresponding to two dominant modes of the patch antenna are placed beneath the patch in an L-shaped configuration at an offset from the patch center. This is not the best configuration of two orthogonal slots to have minimum slot-to-slot coupling (C_{ss}). It is modified in a T-shaped configuration, as shown in figure 2.11b [39]. The coupling reduction, discussed in the crossed slots section in terms of current distributions, also applies to this T-shaped slots. A parametric study of

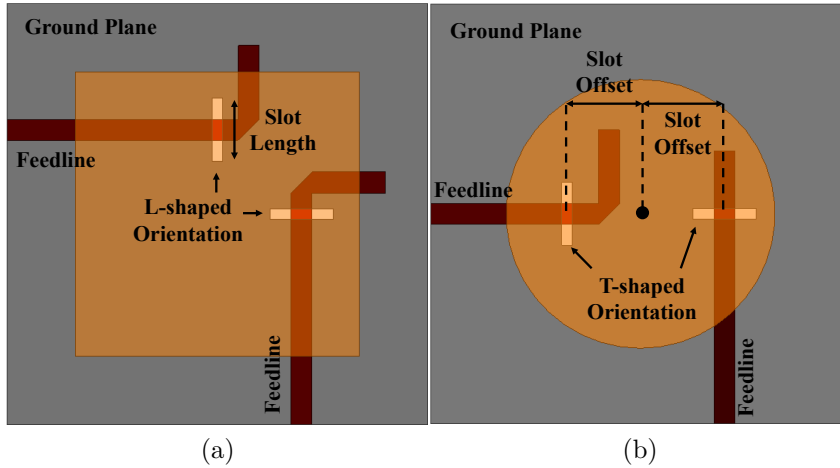


Figure 2.11: Dual-polarized patch antennas, (a) square patch with L-shaped configuration of slots (Concept from [38]), (b) circular patch with T-shaped configuration of slots (Concept from [39]).

port coupling as a function of the slots lengths and their offset from the patch center was carried out in [40]. It has been clarified that the port coupling decreases as the slot lengths decreases or the slot offsets increases. Both these changes are interpreted as an increase of the effective distance between the two slots. It is evident that such distance is limited by the patch dimensions, and reducing slot-to-slot coupling (C_{ss}) by making the slots more distant is not feasible beyond a limit. Alternatively, it can be carried out by modifying the shape of the slots.

Pozar *et al.* modified the slot shape and replaced the original circular slot by a dog-bone aperture [43]. Allowing for stronger coupling to the patch at the same frequency, the dog-bone slot proposes an approximately 30% size reduction. Moreover, it eases the positioning constraints for dual aperture antennas, and reduces the back lobe radiation [43]. The evolution of slot shapes was continued and different modified shapes were proposed [44]. A couple of dual-polarized antennas utilizing H-slots is provided in figures 2.12a

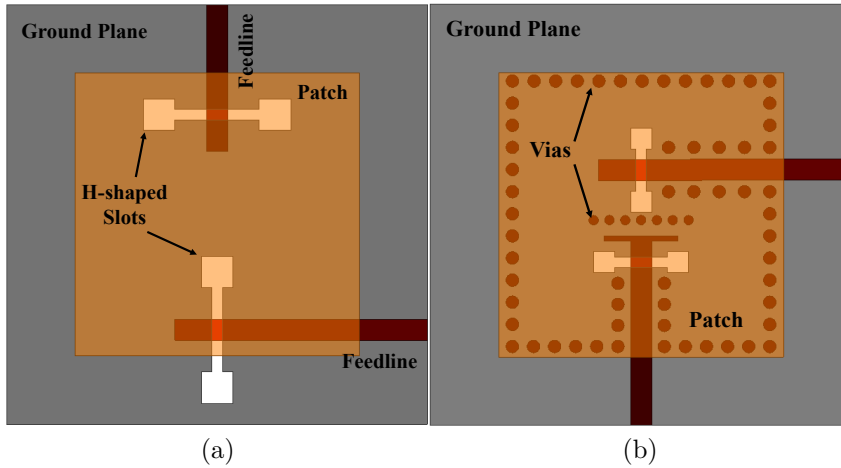


Figure 2.12: Dual-polarized patch antennas with H-shaped aperture-coupled excitation, (a) slots at the edge of the patch (Concept from [41]), (b) slots close to patch center (Concept from [42]).

and 2.12b. The simple design in figure 2.12a demonstrates that high transverse isolation (C_x) does not necessarily require complicated bulky structure and is feasible by following some basic points specified below.

- H-shaped slots are utilized, allowing for shorter lengths of slots and more distant location of them compared to the rectangular slots (C_{ss} reduction).
- The straight feedlines are oriented orthogonally and as far away as possible (C_{ff} reduction).
- T-shaped configuration of slots is utilized (C_{ss} reduction).
- C_{ss} reduction is achieved by locating two slots at the middle and the edge of the patch which are coupled via the magnetic field and the electric field, respectively.
- The resonant frequency of the patch and that of the slot are tuned near to each other [41].

As the aperture gets closer to the center of the patch, better coupling to the patch, hence wider bandwidth is achieved [37]. However, two slots

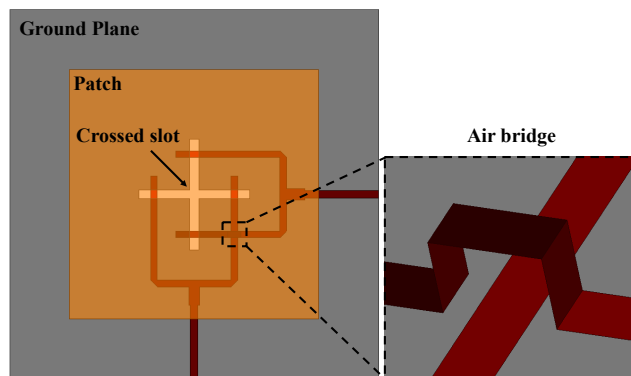


Figure 2.13: A dual-polarized patch antenna with cross slots aperture (Concept from [45]).

close to each other is prone to high slot-to-slot coupling (C_{ss}). Figure 2.12b represents simultaneous reduction of feed-to-feed coupling (C_{ff}) and slot-to-slot coupling (C_{ss}) by inserting metalized vias in the substrate [42]. It is achieved at an increase in the cost and complexity of the design. Rows of vias provide separate rooms for each feedline and corresponding slot and block the transverse leakage (C_x). This blockage can be realized by comparing field distributions of the antenna before and after inserting vias [42].

The aperture-coupled antennas, discussed so far, though isolated lack symmetry in their geometry. The offset slots from the patch center cause a distortion in the antenna radiation patterns at their principal planes. Tsao *et al.* in 1988 proposed a dual-polarized patch antenna excited by a centered orthogonal slots, namely, cross slots shown in figure 2.13 [45]. The symmetry applied to the design is reflected in their symmetric radiation pattern. Each branch of the cross slots is excited with a balanced feed located symmetrically with respect to the cross center. Such a feeding shows lower slot-to-slot coupling (C_{ss}) compared to the single feedline excitation [46]. Moreover, it has the advantage of higher order modes suppression and lower coupling between orthogonal modes (C_{mm}). To avoid overlapping, an air bridge provides a

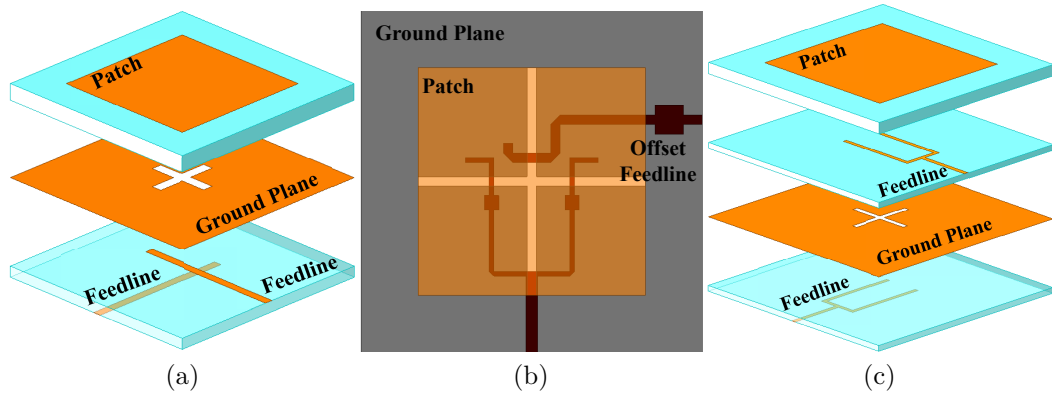


Figure 2.14: Centered cross slot excitations, (a) rectangular feedlines in separate layers (Concept from [47]), (b) asymmetric offset feedlines (Concept from [48]), (c) balanced feed with feedlines on opposite sides of the ground plane (Concept from [49]).

crossover between the two orthogonal feedlines. It complicates the fabrication, and also the inevitable feed-to-feed coupling (C_{ff}) in this region degrades the input port isolation. To avoid the crossover and ease the fabrication process, two alternative solutions were proposed in [47] and [48], and respectively illustrated in figures 2.14a and 2.14b. In figure 2.14a the orthogonal feedlines are laid in two separate layers and the balanced feedline for each polarization is replaced by a single rectangular one. As for figure 2.14b, the balanced feedline for one polarization is replaced with an asymmetric offset feedline. Targonski and Pozar compared the performance of a single offset feedline with that of a balanced one [46]. They demonstrated that by feeding the slot in a balanced configuration with two symmetric feedlines, no voltage is induced across the unfed slot (C_{ss}), and the two crossed apertures remain decoupled. Therefore, the mentioned solutions, albeit easy-to-fabricate, are not of superior performance. To retain the balanced feedlines for both polarizations and remove the crossover, Yamazaki *et al.* proposed the antenna shown in figure 2.14c [49]. The two feedlines are implemented on the opposite sides of the ground plane.

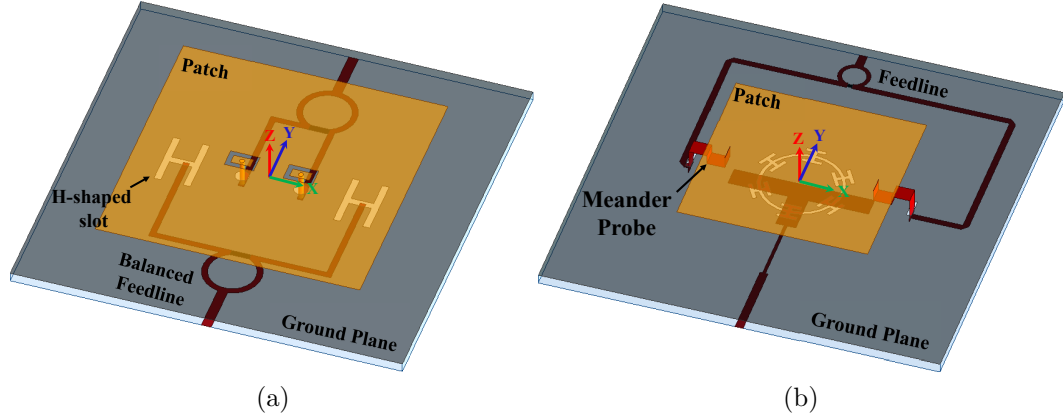


Figure 2.15: Hybrid-fed patch antennas, (a) aperture-coupled probe-fed excitation (Concept from [51]), (b) aperture-coupled meander probe-fed excitation (Concept from [52]).

So, the coupling between them (C_{ff}) is mainly blocked by the ground plane. How the upper feedline excites the antenna could be a deviation from the original aperture-coupled excitation as it could be coupled to the patch directly. It is resolved by placing an electrically thick substrate between upper feed and the antenna [50]. Such excitation could be also carried out for offset single sided aperture-coupled antennas with different configurations which may be attractive options in the future research.

2.3.4 Hybrid-fed Dual-polarized Patch Antennas

Any combination of feeding methods for patch antenna could be a new dual-polarization feeding called hybrid excitation. It remains an area of fruitful investigation as not many researches have been reported in this field so far. Figures 2.15a and 2.15b show two samples of hybrid-fed rectangular patch antennas [51], [52]. A combination of aperture-coupled and probe-fed excitations are utilized in both antennas. Due to differential excitation for one polarization, both antennas have complicated structures. Figure 2.15a demonstrates

Table 2.4: A comparison of the performance of aperture-coupled dual-polarized antennas in group II.

Ref.	Freq. BW (GHz)	Port Isolation (dB)	X-pol (dB)	Dimensions (mm) Length×Width× Height
[38]	2.18-2.24	>18	NA	55×55×3.15
[39]	1.56-1.63	>35	NA	NA×NA×4
[41]	10.7-12.75	>40	NA	11.4×11.4×2.26
[42]	11.8-14.6	>40	>-26	18.5×18.5×1.3
[45]	3.31-4.17	>27	>-25	NA
[47]	4.65-6.25	>22	>-18	NA×NA×8.68
[48]	1.75-2.25	>35	>-20	54×50×15.762
[49]	1.75-2.25	NA	NA	24×19×3
[51]	1.644-1.905	>40	>-20	57.5×57.5×15
[52]	2.3-2.58	>40	>-23	53×53×10

another balanced aperture coupled excitation. Instead of a single offset slot, two symmetric H-shaped slots along the x-axis are excited uniformly. Recalling the field distributions of y-directed modes, x-axis ($y=0$) or any of parallel ones ($y=y_0$) comprises semi-impedance locus associated with y-directed modes. Therefore, TM_{01} can be excited either by a single aperture or by multiple apertures of uniform excitations distributed along any of these lines. Two symmetrical apertures, as shown in figure 2.15a, have the advantage of transverse modes suppression which yields lower cross coupling (C_x) and symmetric radiation pattern.

2.4 Two Different Radiation Elements in a Dual-polarized Antenna - Group III

The dual polarization antennas in this category comprise two different radiation elements assigned to each polarization. Ideally, when two ports are absolutely decoupled, each element radiates its respective radiation pattern.

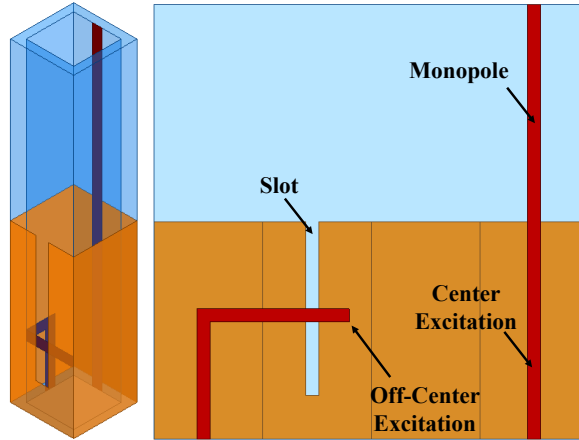


Figure 2.16: 3-D and expanded views of a dual-polarized monopole-slot antenna (Concept from [53]).

Therefore, choosing elements with low cross-polarization will enhance the ultimate polarization purity of the dual-polarized antenna. Because of two different radiation elements, the matching between the two copolarization beams is subject to some degradation. However, this can be modified by using complementary elements. The antennas proposed in this section are used for base station systems where the priority is given to the omnidirectional radiation pattern rather than very low cross-polarization.

2.4.1 Complementary Elements

Having complementary radiation patterns, a slot antenna and a flat metallic antenna of the same size can be integrated in a dual-polarized antenna with matched copolar beams [14]. Figure 2.16 depicts a compact dual polarized monopole-slot antenna implemented on the facing sides of a cuboid [53]. The same coupling discussion, provided for crossed slot, also holds for this antenna, with the exception that one slot is replaced by a monopole antenna. Asymmetric single-sided excitation of the slot accounts for some level of cross coupling (C_x). Higher performance could be achieved with a balanced or differential

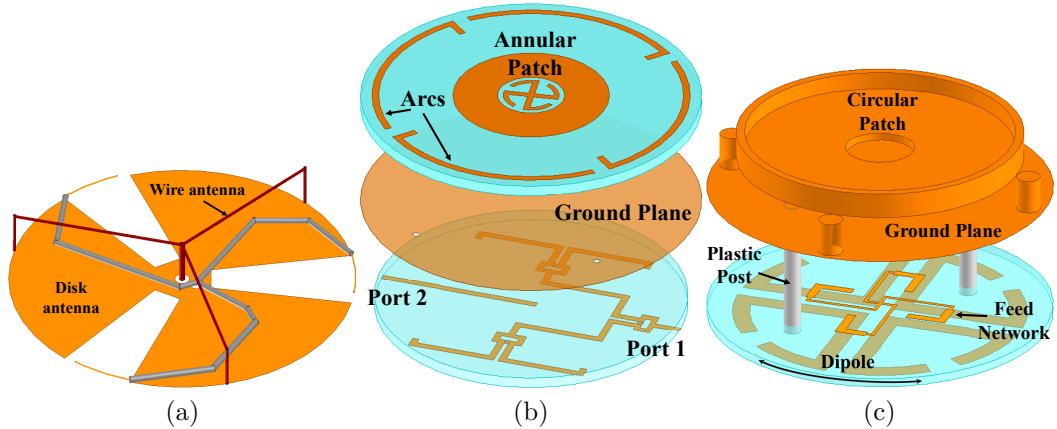


Figure 2.17: Dual polarized omnidirectional antennas (a) a notch-wire antenna (Concept from [54]), (b) a ring patch-arcs antenna (Concept from [55]), (c) a circular patch-dipoles antenna (Concept from [56]).

feeding of slot which remains as a research opportunity.

2.4.2 Non-complementary Elements

A group of elements, each covering a fraction of space, can function as a vertical monopole antenna. To obtain an omnidirectional pattern, a feed network is required to excite each element with uniform excitation. It complicates the geometry of the dual-polarization antenna and increases the probability of the cross coupling and the interference in the elements' radiation patterns. A notch-wire antenna is shown in figure 2.17a [54]. It includes a three-notched disk antenna and a three wire antenna as components for the horizontal and the vertical polarization, respectively. Three notches and three wire-loops, each spaced 120° apart and uniformly excited, are utilized to emulate omnidirectional pattern. In order to reduce the cross coupling (C_x) between radiation elements, the wires are placed between the notches where the current distribution on the excited disk has a null. Despite the null location of wires, the antenna exhibits poor performance in terms of port isolation. It is because

Table 2.5: A comparison of the performance of antennas in group III.

Ref.	Freq. BW (GHz)	Port Isolation (dB)	X-pol (dB)	Dimensions (mm) Length×Width× Height
[53]	2.37-2.53	>36	>-6	50×16×16
[54]	1.68-1.82	>10	NA	50×50×20
[55]	4.8-5.02	>40	>-18	48×48×4
[56]	1.7-2.2	>40	>-12	120×120×27

of the corresponding parallel sections of the two radiation elements located in close proximity. A planar version of the dual-polarized omnidirectional antenna is provided in figure 2.17b [55]. An annular-ring patch serves as a vertically polarized antenna while the horizontal polarization is realized with four arcs encircling the patch. To obtain the omnidirectional pattern at their corresponding H-planes, the annular patch is excited at its TM_{01} mode and the arcs are uniformly excited by a Wilkinson power divider. To reduce the coupling between the radiation elements (C_x), they are placed within a radial distance from each other in a symmetric configuration. Moreover, the feed networks for both polarizations are implemented beneath the ground plane. So, the ground plane blocks the coupling between the antennas and the feedlines as well as spurious radiation of the feedlines. The annular-ring and the arcs are replaced by a circular folded patch and half-wavelength dipoles, respectively, shown in figure 2.17c [56]. The radiation elements are located on the opposite sides of the ground plane where the radial distance of previous design is replaced by a height distance lowering the coupling between elements (C_x). Such space diversity is problematic in applications where compact geometry is required.

Chapter 3

Proposed Crossed Dipole and its Modification

3.1 Introduction

We have examined and compared various dual-polarized antennas in the previous chapter. It was shown therein that the patch antennas are intrinsically narrow bandwidth since they work based on the principle of the slot antennas on their both radiating edges. Wider frequency bandwidth can be obtained by the stacked microstrip patch antennas where the upper patches are parasitically coupled to the principal patch. However, it is not a suitable solution for a large phased array antenna with a respective large ground plane [57]. This grounded thick dielectric provides a proper medium for the surface wave to travel along the ground plane and radiate [58]. Such radiations make some ripples on the radiation patterns and reshape them, causing a mismatch between copolar radiation beams. We will examine the surface wave effects on the shapes of radiation patterns in the following chapters.

Alternatively, the crossed dipole with sufficient operational frequency bandwidth can be utilized as an appropriate solution. Contrary to the patch antennas, the crossed dipole does not utilize a continuous dielectric slab over the ground plane, resulting in suppression of the surface wave. Various crossed

dipoles topologies have been reported in the literature [59]. A non-planar crossed dipole in [60] achieved 34 dB port-to-port isolation. Due to high sensitivity to fabrication tolerances and lack of the balun feed, the cross-polarization of the antenna is severely degraded. In contrast, an easy-to-fabricate printed dipole with 35 dB port isolation is provided in [10]. However, it suffers from the collocation of co- and cross-polarization peaks in the radiation pattern. The stringent requirements of the MPAR project need a detailed design of a new antenna.

In this chapter, we propose a crossed dipole antenna which meets the MPAR requirements [9]. High port isolation and low cross-polarization are achieved. The baluns are designed below the principal ground plane which allows for pure radiation of the dipole and lower cross-polarization level. Finally, the fabrication of the antenna using inexpensive printed circuit technology eases the manufacturing process.

3.2 Proposed Crossed Dipole

The fundamental idea and the implemented version of the proposed crossed dipole are provided in figure 3.1a and figure 3.1b, respectively. For each polarization, a bent dipole, a parallel line, and a balun are sandwiched between two substrates of 0.06 inch thickness. Dipoles are connected to parallel lines and are situated a quarter wavelength above the principal ground plane. Baluns are designed below the principal ground plane. Each balun has two branches, extending 180° out of phase from each other, providing a balanced differential port. The parallel lines are attached to the baluns through a cross-shaped slot cut in the principal ground plane. To have collocated orthogonal dipoles without intersection, two baluns with different lengths are considered. The final

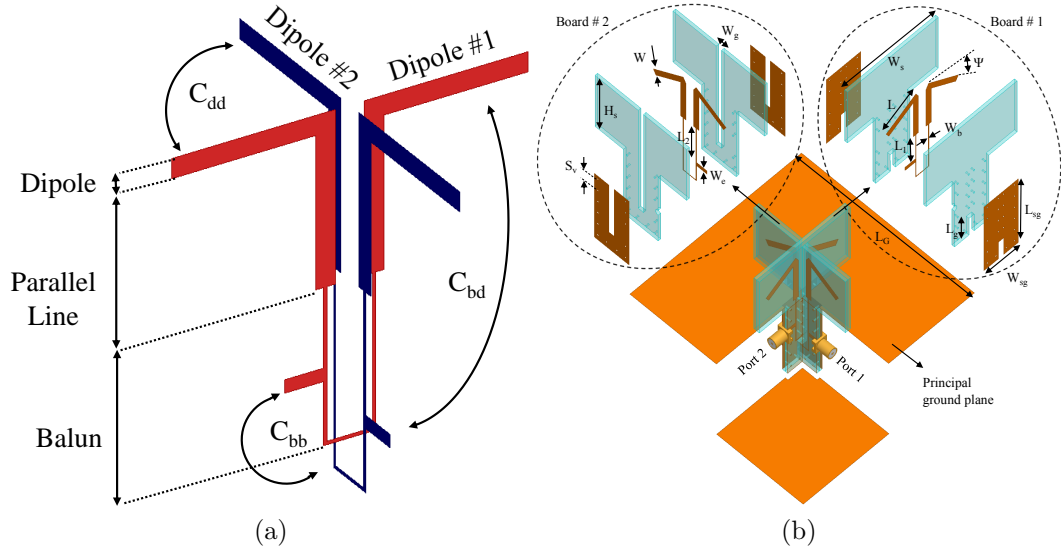


Figure 3.1: Proposed crossed dipole antenna, (a) fundamental idea. (b) implemented version with exploded views of two orthogonal boards.

Table 3.1: Detailed Dimensions of the fabricated antenna (unit: mm)

Parameters	L	W	L_G	W_s	H_s	L_g	L_1
Values	20	3	300	55	32	10.45	16
Parameters	W_g	L_{sg}	W_{sg}	W_e	W_b	S_v	L_2
Values	3.05	40	20	2	0.35	7	22.3

dimensions of the antenna, implemented using Rogers RO 4003 ($\epsilon_r = 3.55$), are provided in Table 3.1.

3.2.1 Design and Discussion

The cross coupling (C_x), discussed in the previous chapter as the major interaction between the orthogonal radiation elements, is specified for the crossed dipole in figure 3.1a in terms of its contributors as

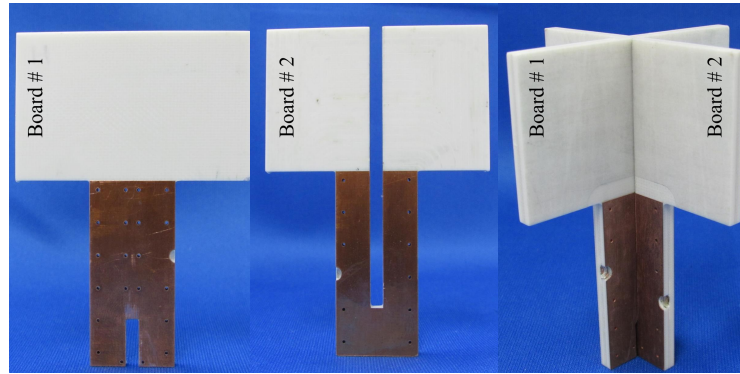
$$C_x = C_{dd} + C_{bb} + C_{bd} + C_{db} \quad (3.1)$$

where C_{dd} is the coupling between orthogonal dipoles, C_{bb} is the coupling between orthogonal baluns, and C_{bd} and C_{db} are the coupling between balun #2 and dipole #1 and vice versa. Decreasing each of these three components reduces the transverse coupling (C_x).

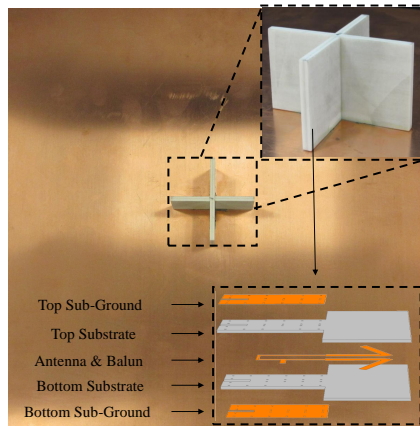
The coupling between dipoles (C_{dd}) and its suppression using the null locus was discussed in the previous chapter. We graphically showed therein, in terms of voltage distribution, that two orthogonal dipoles with identical poles (geometrical symmetry) will have zero interaction ($C_{dd}=0$) if they are driven with ideal differential signal (electrical symmetry). It is shown in figure 3.1a that each dipole possesses two identical bent wings. It is worth noting that the null locus can be shifted from the equator if either electrical or geometrical symmetry is disturbed. These two cases which is prone to some cross coupling will be discussed later.

The parallel baluns, shown in figure 3.1b could remarkably account for cross coupling between two polarizations. To implement each of the baluns, the stripline structure is employed. As shown in figure 3.1b, in the stripline structure, the balun is sandwiched between two sub-ground planes and surrounded by electroplated vias. This way, each balun situated in a cavity shaped structure is isolated from the other balun and so, S_{bb} is significantly reduced.

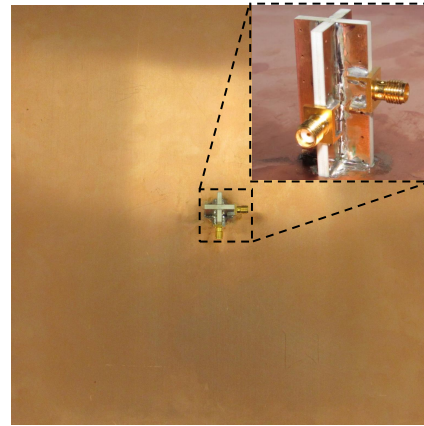
The balun of the antenna #1 can be coupled to the dipole #2 (C_{db}), and vice versa. This is addressed in figure 3.1a, where the dipoles and the baluns are designed on the opposite sides of a principal ground plane connected to each other through a crossed slot in the ground plane. In doing so, while they are isolated from each other, the spurious radiation of the baluns are also blocked by the principal ground plane.



(a)



(b)



(c)

Figure 3.2: Prototype of the proposed antenna, (a) side view of individual boards and collocated crossed dipole without ground plane, (b) top view with subset showing the antenna stack-up, and (c) bottom view.

3.2.2 Fabrication Process

To verify the simulation results, the proposed crossed dipole was fabricated at Radar Innovations Laboratory, the University of Oklahoma. The dipole, parallel line, and balun are all designed in a single metal layer, making it possible to fabricate them simultaneously. It precludes any additional soldering process and consequently, eliminates extra assembling loss. Each dipole along with corresponding balun and parallel line were milled simultaneously on the bottom layer of the top substrate using a LPKF ProtoMat S103 (sub-

set of figure 3.2b). The two stripline sub-ground planes are milled on the top layer of the top substrate and the bottom layer of the bottom substrate. The two boards are bonded together using Rogers RO4450B prepreg. Vias were drilled and electroplated to keep the two ground planes at the same potential. A small section of PCB was removed to ease soldering the SMA connector. To interlock collocated dipoles a couple of short and long gaps, shown in figure 3.2a, are cut into boards #1 and #2, respectively. Cutting the gaps into two boards leave two slits with different lengths on the sub-ground planes. Although two boards look a little different, after collocation both dipoles experience identical environment. The antenna assembly was mounted on a fairly large 300 mm \times 300 mm copper ground plane to decrease the edge effects and block the measurement components.

3.2.3 Measurement Verification

The S-parameters of the fabricated antenna was measured using a N5225A network analyzer from Agilent Technologies, calibrated using an E-Cal module. Figure 3.3 provides simulation and measured S-parameters of the antenna. A better than 15 dB return loss for both ports over the entire frequency range is achieved. While measured S_{11} almost matches its simulation counterpart, S_{22} experiences a slight shift of center resonance frequency, which can be attributed to fabrication tolerances. It is worth noting that, the most critical dimension of the proposed antenna is the width of the baluns (0.35 mm). Any discrepancy between the widths of two branches of the balun, will cause a frequency resonance shift and also will result in unequal power split between two poles of the dipole. Such discrepancy due to fabrication tolerances is shown in figure 3.4. This condition impairs the geometrical symmetry, the isolation

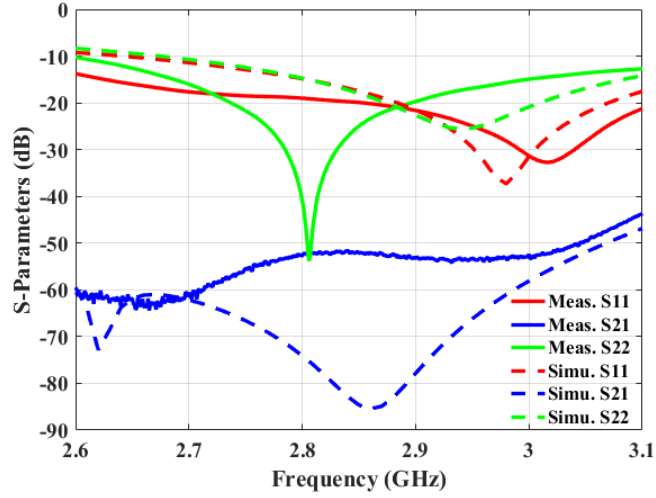


Figure 3.3: Simulated and measured S-parameters of the crossed dipole antenna.

between dipoles, and the polarization purity. Therefore, a shift between center resonant frequencies is observed in the measured and simulated S_{11} , and the measured isolation is less than its simulated result. Nevertheless, the port-to-port isolation remains better than 52 dB over the entire frequency range.

The radiation patterns of the antenna were measured in the far-field anechoic chamber at the Advanced Radar Research Center of the University of Oklahoma, and the measurement set-up is provided in figure 3.5. A fairly high stand of Rohacell 31HF foam from EVONIK industries, with a dielectric constant of 1.05 is fabricated and mounted over the pedestal to emulate the simulation environment. To suppress any parasitic interference, the feeding cable is covered by absorbers as shown in figure 3.5a. The orthogonal element is terminated in a 50Ω load. Following meticulous measurement considerations, we achieved -50 dB broadside cross polarization level at the center frequency and better than -40 dB over the entire principal planes.

The measured and simulated radiation patterns are illustrated in figure 3.6.

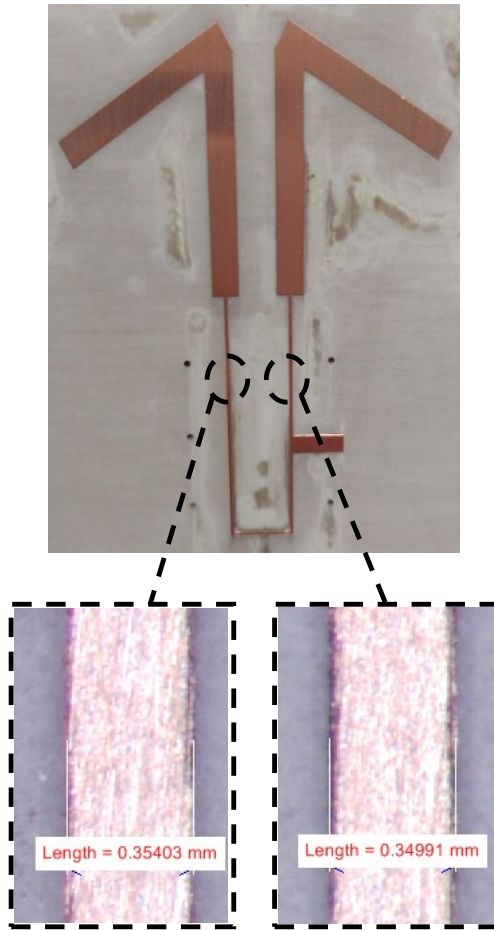


Figure 3.4: Different widths of two branches of the balun.

Whereas the lowest cross-polarization occurs at the center frequency, it rises at the beginning and the end of the frequency range. This is consistent with the simulation results. It is because of the phase imbalance of the balun, as shown in figure 3.7, which is optimized at the center frequency of 2.85 GHz and increases monotonically up to $\pm 9^\circ$ toward the beginning and the end of the frequency range. This condition, referred to as electrical asymmetry, disturbs the null locus from the middle line of the antenna, as shown in the subset of figure 3.7, and causes some cross coupling between the two polarizations. As such, the peak of the copolarization pattern at corresponding E-plane is

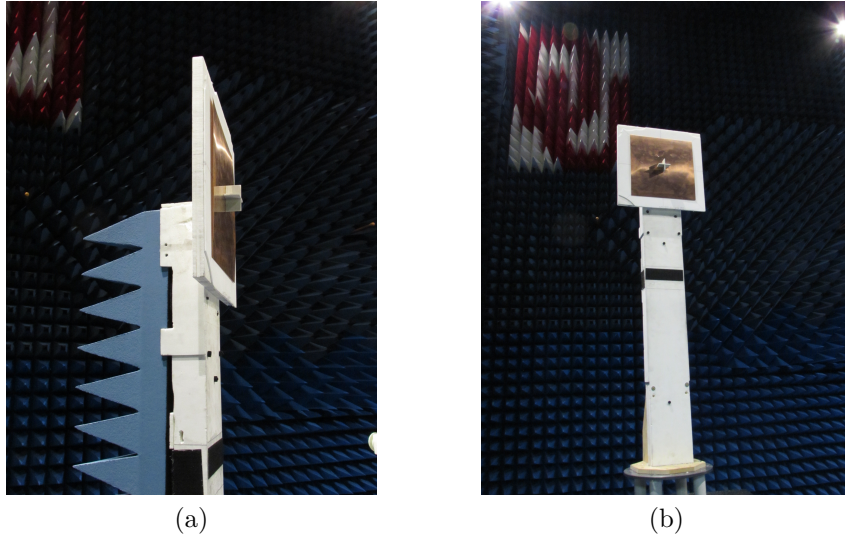
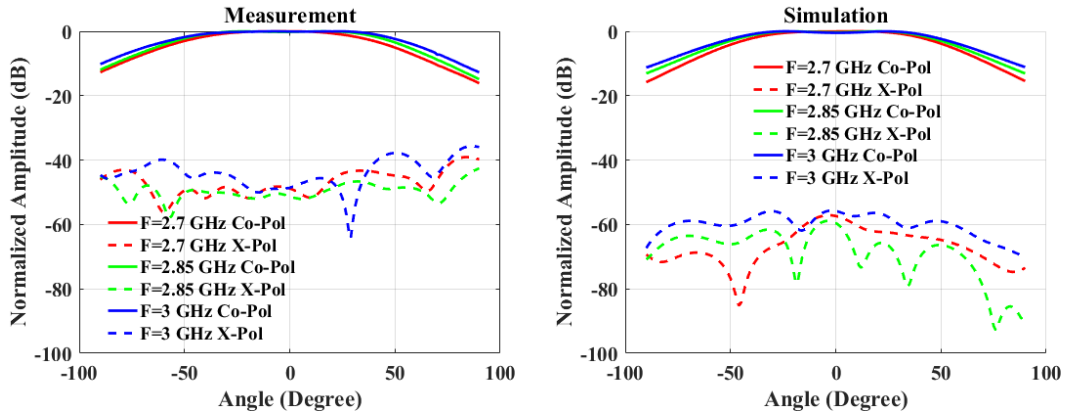


Figure 3.5: Pattern measurement set-up, (a) Side view, (b) Front view.

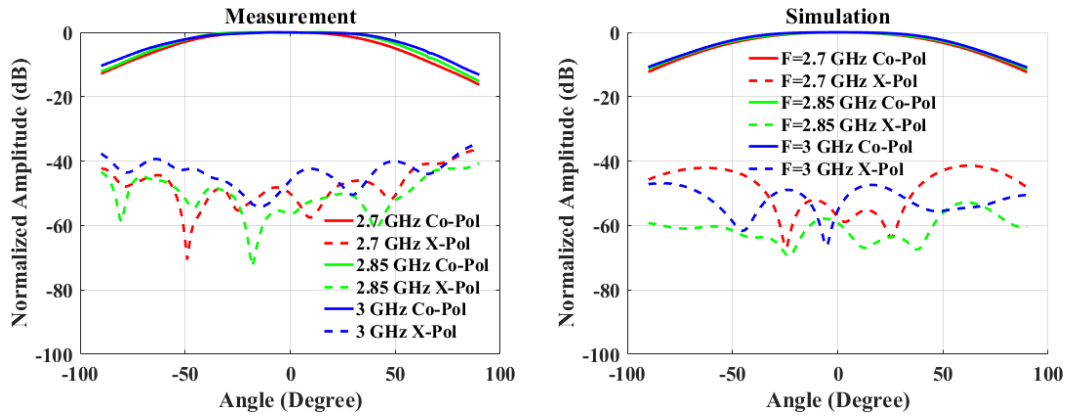
shifted by $\pm 0.5^\circ$, and the cross-polarizations increase at these frequencies. In addition, contrary to the simulation, the cross-polarization level at $\pm 90^\circ$ increases which is attributed to the edge diffraction of the principal ground plane and other measurement components at the back of the antenna. The antenna exhibits very low simulated cross-polarization in E-planes (below -50 dB). The discrepancy observed between the simulated and measured cross-polarization in this plane is due to the limitation of the measurement system. Because of the geometrical symmetry of the structure, the orthogonal polarization has similar radiation characteristics which is not shown for brevity.

3.3 A Modified Version of the Proposed Crossed Dipole

Using similar and symmetrical structures for both polarizations, and their effects on the polarization purity of a dual-polarized antenna were emphasized in the previous chapter. Following the same symmetry point, we modified the above-mentioned crossed dipole, and proposed a geometrically symmetrical



(a)



(b)

Figure 3.6: Measured and simulated radiation patterns of the proposed antenna at principal planes, (a) E-plane, (b) H-plane.

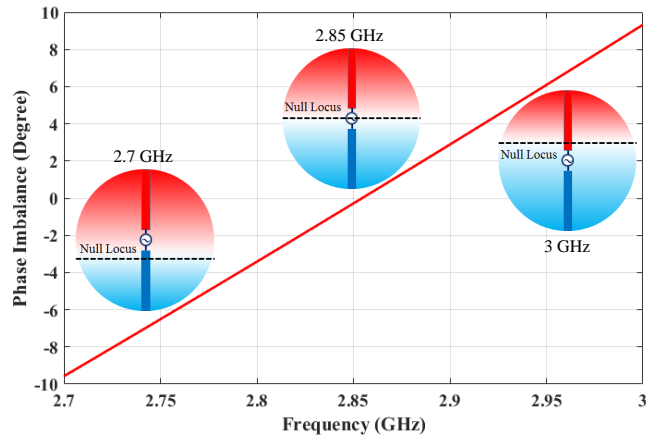


Figure 3.7: The phase imbalance of the proposed balun versus frequency.

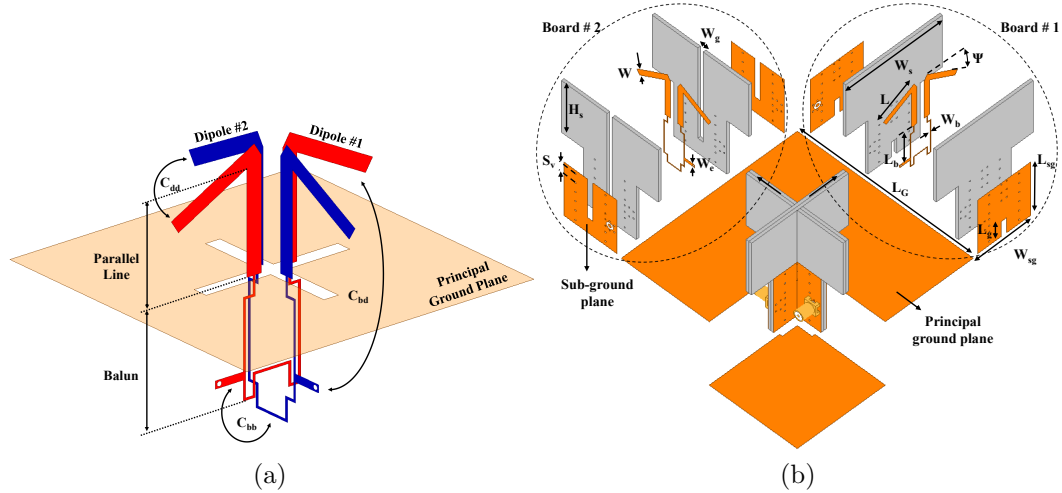


Figure 3.8: A modified version of the proposed crossed dipole antenna, (a) fundamental idea. (b) implemented version with exploded views of two orthogonal boards.

antenna in figure 3.8 [61]. Its different design of the baluns can be realized by comparing with figure 3.1a. Contrary to the previous design, which utilizes two baluns with different lengths, the modified version has two baluns with identical lengths. They are folded upward and downward to avoid intersection at the crossover. This design allows for a shorter length of the antenna, and the size reductions can be revealed by comparing dimensions of the new antenna, provided in Table 3.2, with those of the previous one. In addition, the widths of the branches of the baluns are increased to alleviate the fabrication tolerances, discussed earlier. The higher performance in terms of highly matched beams and similar resonance features, obtained by this modification, will be discussed in the following.

Having a group of key parameters, the proposed antenna shows versatility to match various frequency range with desired bandwidth. Among them, the length (L) of the dipole, its width (W), and its bend angle (Ψ) play the dominant roles. Figures 3.9a and 3.9b depict the parametric study on the length

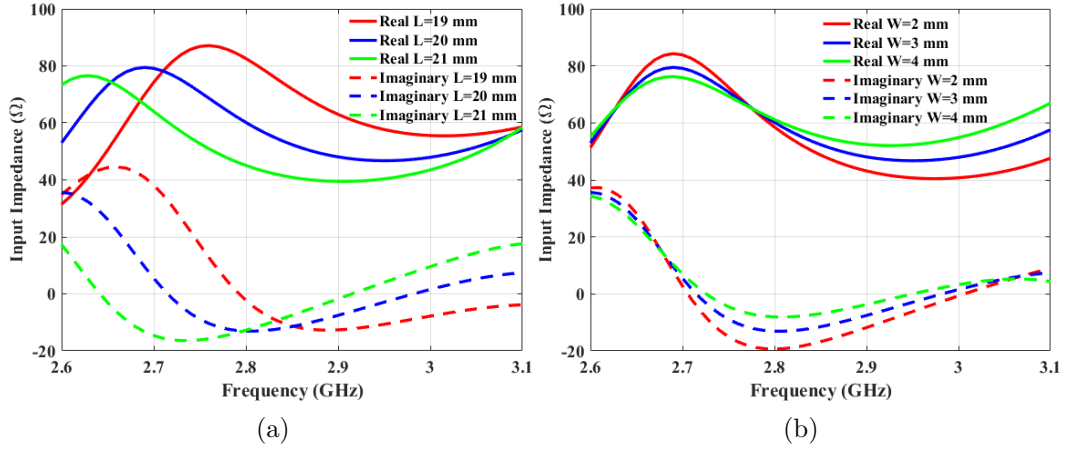


Figure 3.9: Input impedance of the antenna with dipole dimensions, (a) variation in antenna length ($W=3$ mm), (b) variation in antenna width ($L=20$ mm).

Table 3.2: Detailed Dimensions of the fabricated antenna (unit: mm)

Parameters	L	W	L_G	W_s	H_s	L_g	L_b
Values	20	3	100	55	32	9.275	19
Parameters	W_g	L_{sg}	W_{sg}	W_e	W_b	S_v	L_2
Values	3.05	33	30	1.6	0.4	5.7	22.3

and the width of the dipoles, respectively. While the length of the dipole determines the center resonance frequency, the bandwidth is mainly affected by the width of the dipole. It has been demonstrated that a bent dipole with a bend angle of 30° shows the minimum off-boresight gain loss [62]. Because the proposed antenna is eventually intended to function as an element in a scanning array, the dipole bent angle is fixed at 30° to achieve minimum loss in scanning. The final dimensions of the antenna, implemented using Rogers RO 4003 ($\epsilon_r = 3.55$), are provided in Table 3.2.

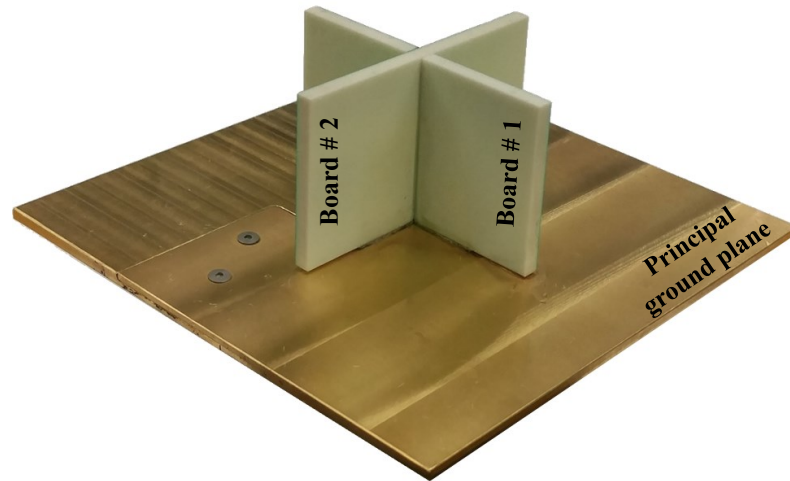


Figure 3.10: Prototype of the modified crossed dipole antenna.

3.3.1 Measurement Verification and Matched Beams

A prototype of the modified crossed dipole was fabricated and displayed in figure 3.10. It may look similar to the original crossed dipole, however, it was fabricated and assembled differently. The edge-mount connector is replaced by a surface-mount connector, allowing for precise automatic assembly. There is no need for a cut of the substrate to access middle layer, so the input impedance at the soldering location is not disturbed anymore. The principal ground plane in the modified version is made of brass which is quite resistant to deformation during hot temperature of the soldering process. Therefore, the flatness of the new principal ground plane improves the linearity of the polarizations.

The S-parameters of the antenna were measured and plotted along with simulation results in figure 3.11. The measurement and simulation return loss match well over the entire frequency range. Better than 14 dB return loss for both ports are achieved. Compared to previous design, better match between two return losses is achieved owing to similar designs for two polarizations. It

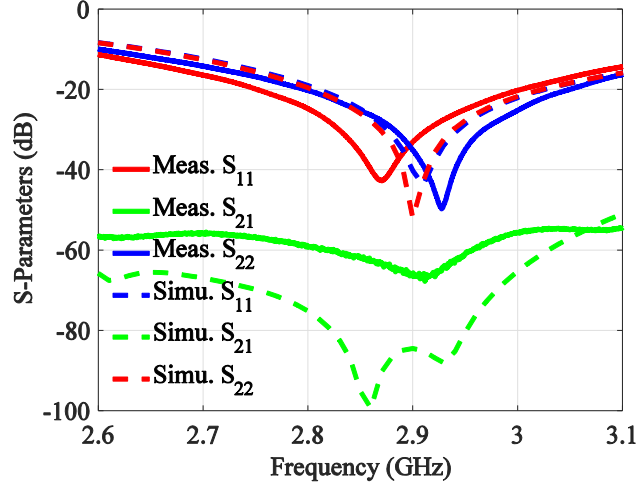


Figure 3.11: Simulated and measured S-parameters of the proposed antenna.

is worth noting that the extreme low level of the simulated port isolation can be easily affected by any fabrication and assembly tolerances. Nevertheless, a measured port isolation higher than 56 dB over the entire frequency range is achieved. To the best of our knowledge, the proposed antenna is among the most isolated antennas reported in the literature to date.

The radiation characteristics of the antenna are provided in figure 3.12. The cross-polarization levels remain below -40 dB in both principal planes over the entire frequency range. Design of identical baluns and dipoles for two polarizations are reflected in the highly matched copolar patterns corresponding to two polarizations, as shown in figure 3.13. Similar radiation patterns of the orthogonal element are not provided for brevity. Besides the multi-mission performance of the proposed crossed dipole, the orthogonality of its radiation patterns corresponding to two polarizations along with high port isolation and matched beams make it a promising candidate for MIMO applications. Vaughan *et al.* demonstrated in [63] that a theoretical crossed dipole could be oriented so that the envelope correlation coefficient (ECC) is

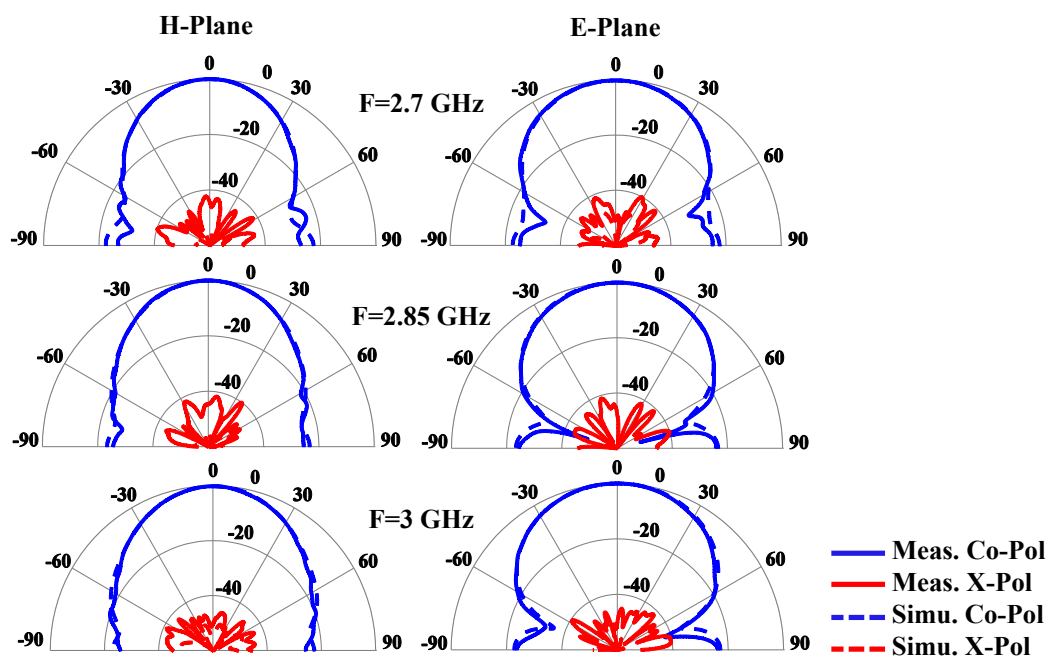


Figure 3.12: Simulated and measured radiation patterns of proposed crossed dipole at different frequencies in both principal planes.

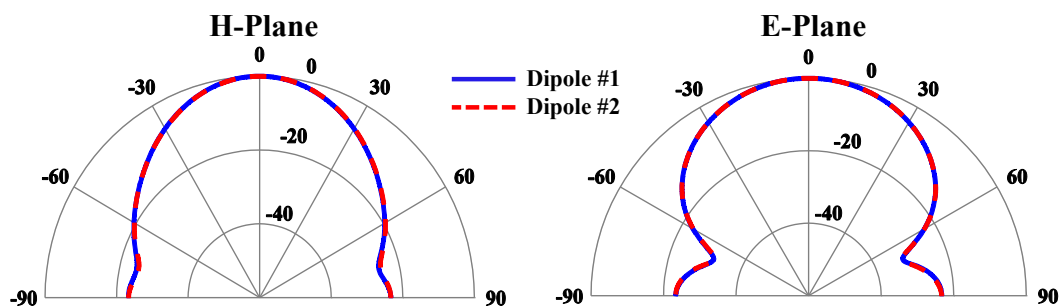


Figure 3.13: Matched copolar patterns of dipoles at principal planes.

identically zero. However, in practice, the ECC for a crossed dipole is subject to degradation regarding the isolation between dipoles. The higher isolation is achieved, the lower ECC results. To examine the independency between two dipoles radiation patterns in the suggested design, the simulated ECC in Ansys HFSS using far field-based method with frequency resolution of 10 MHz and the angular steps of 1 degree is computed using (3.2), and shown

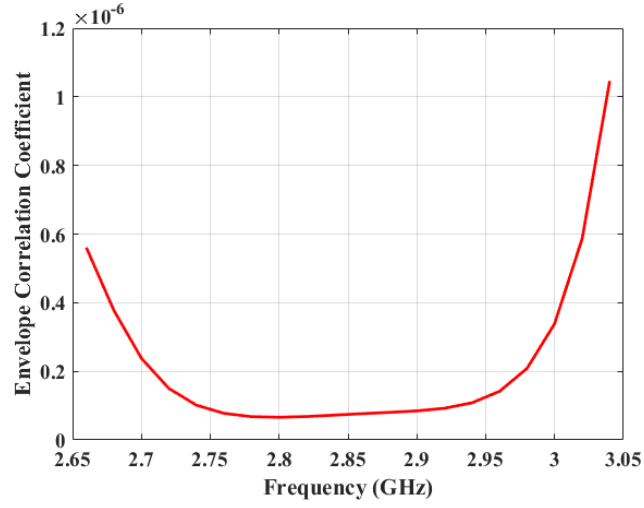


Figure 3.14: Simulated envelope correlation coefficient of the antenna.

in figure 3.14.

$$\rho_e = \frac{\left| \int \int_{4\pi} [\vec{F}_1(\theta, \phi) \bullet \vec{F}_2(\theta, \phi)] d\Omega \right|^2}{\int \int_{4\pi} |\vec{F}_1(\theta, \phi)|^2 d\Omega \int \int_{4\pi} |\vec{F}_2(\theta, \phi)|^2 d\Omega} \quad (3.2)$$

In this equation $\vec{F}_i(\theta, \phi)$ is the far-field radiation pattern of the i th antenna, and \bullet denotes the Hermitian product [63]. This extremely low ECC result indicates the effectiveness of the designed antenna in diversity performance.

Chapter 4

Linear Array Antenna of Crossed Dipoles

4.1 Introduction

A cylindrical polarimetric phased array radar (CPPAR) was proposed for MPAR and developed at the Advanced Radar Research Center (ARRC) of the University of Oklahoma [64]. This demonstrator is displayed in figure 4.1. A cylinder is divided into four quadrants, each can transmit and receive individually. Instead of azimuth scanning, each quadrant commutates. That is, each sector can be electronically rotated around the cylinder so as to the peak of the array beam is always at broadside. Such feature allows for invariant azimuth scanning and high polarization purity [4].

The first demonstrator is populated by frequency scanning linear arrays of patch antennas provided in figure 4.2 [65]. Besides PCB technology, used in the fabrication of the patch antennas, all 19 elements of each column are excited by a series feed, reducing cost and complexity of the antenna design. The beam steering of each polarization in the elevation is achieved using the frequency scanning while only one T/R module is needed for each column. Such antenna allows CPPAR to fully operate in short-range weather measurements.

The future operational CPPAR will require an individual excitation of ele-



Figure 4.1: CPPAR antenna array and demonstrator designed and fabricated at the University of Oklahoma (From [4]).

ments which enables it to perform long-range measurement and agile adaptive scanning. Moreover, the polarimetric performance of current antenna can be substantially modified in a new version. In dual polarization series feed antenna array, part of the cross coupling could occur between feedlines. This is shown in exploded view of the antenna in figure 4.2, where the two series feedline, assigned to each polarization, are parallel and could be easily coupled to each other. To avoid such a problem, a wall of plated vias were drilled between the two feedlines [65]. This improves the cross-polarization to below -30 dB. However, it complicates the antenna design and increases the cost.

It is known that a patch antenna is a narrow bandwidth antenna as it works based on the principle of the radiating slots. To cover the MPAR frequency range, stacked patch antennas, as shown in figure 4.2, were utilized. Such a thick substrate over a giant cylindrical ground plane provides a proper medium for the azimuthal surface wave to propagate around the cylinder. This impairs the isolation between both adjacent columns and quadrants. Moreover, the surface wave refractions will change the shape of the patterns, resulting in a mismatch between the copolar beams.

Finally, the patch antenna is not symmetrical with respect to its center. This can be revealed by considering the shapes and locations of the apertures

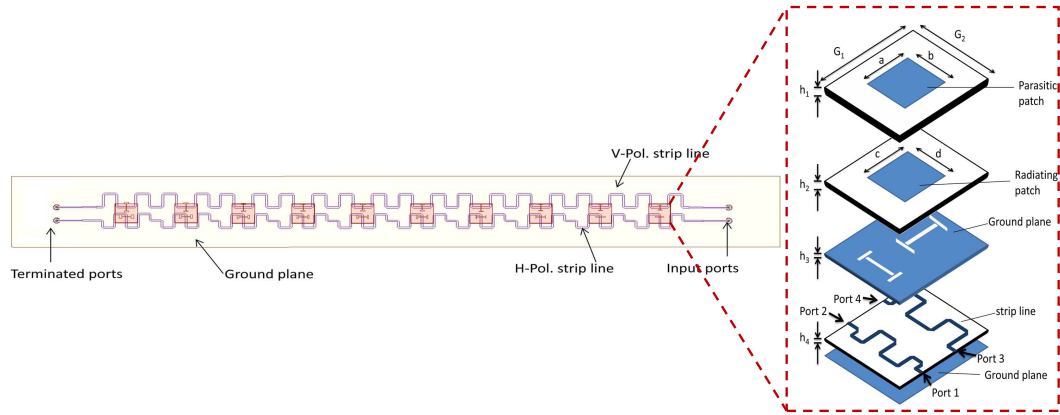


Figure 4.2: Frequency scanning linear array and the exploded view of its respective patch antenna (From [65]).

in exploded view of figure 4.2. This will eventually results in different coupling mechanisms between the two horizontal and the two vertical adjacent polarizations in the array environment. Consequently, a mismatch will occur between the two copolar radiation patterns. Besides that, using a symmetrical element will benefit the antenna in different ways that will be discussed thoroughly in the next chapter.

It is the purpose of this chapter to introduce an alternative to the current frequency scanning antenna array. The proposed linear array includes the modified version of the crossed dipole antenna discussed in the previous chapter. The elements in the linear array are individually excited, allowing for beam shaping and fast adaptive scanning. Higher isolation between the two polarizations is achieved by eliminating the shared series feed. The proposed elements do not require a thick substrate over the ground plane. Therefore, compared to the stacked patch antenna, the surface wave on the cylinder diminishes. This will be discussed in terms of the ripples of the cylindrical embedded element pattern. To attain a lower cross-polarization level, we used an imaged arrangement of the elements in the array configuration.

4.2 Antenna Structure and Design

Figure 4.3 shows the geometry of the proposed linear array along with an exploded view of the element. Each polarization of the element comprises a balun, a parallel line, and a dipole, all sandwiched between two RO 4003 substrates. In addition to identical parallel lines and dipoles, corresponding to two polarizations, a pair of similar baluns with same lengths are designed. One balun is folded upward and the other downward to avoid intersection in the crossover. The parallel lines are attached to the baluns through a crossed slot etched on the principal ground plane. Figure 4.3 also depicts the linear array which consists of 8 crossed dipole elements. In this work, the elements are individually fabricated and situated next to each other. So, we can rotate the elements and examine different configurations. It is also possible to simultaneously fabricate all the elements along the axis in a single step which reduces the fabrication cost. The final dimensions of the proposed linear array are provided in Table 4.1.

The proposed antenna is designed for the frequency range of 2.7 to 3.0 GHz. An inter-element spacing of 50 mm ($0.5\lambda_u$) was chosen in order to avoid the grating lobe in scanning up to $\pm 45^\circ$. Figure 4.4a shows the scanning performance of the middle element in terms of its simulated active VSWR in the HFSS. With active VSWR < 2 over the entire operational bandwidth, the proposed antenna has no blindness effect in scanning up to $\pm 45^\circ$. The active S_{12} is also provided in figure 4.4b. It remains below -40 dB even in severe scanning, showing the ability of the antenna to isolate its two polarizations.

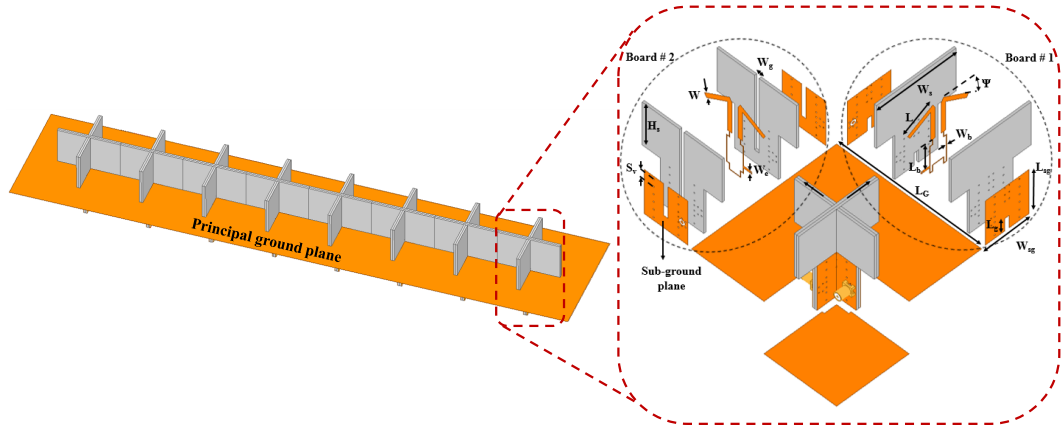


Figure 4.3: Linear array of the crossed dipole and the exploded view of its element.

Table 4.1: Detailed Dimensions of the fabricated antenna (unit: mm)

Parameters	L	W	L_G	W_s	H_s	L_g	L_b
Values	20	3	100	55	32	9.275	19
Parameters	W_g	L_{sg}	W_{sg}	W_e	W_b	S_v	L_2
Values	3.05	33	30	1.6	0.4	5.7	22.3

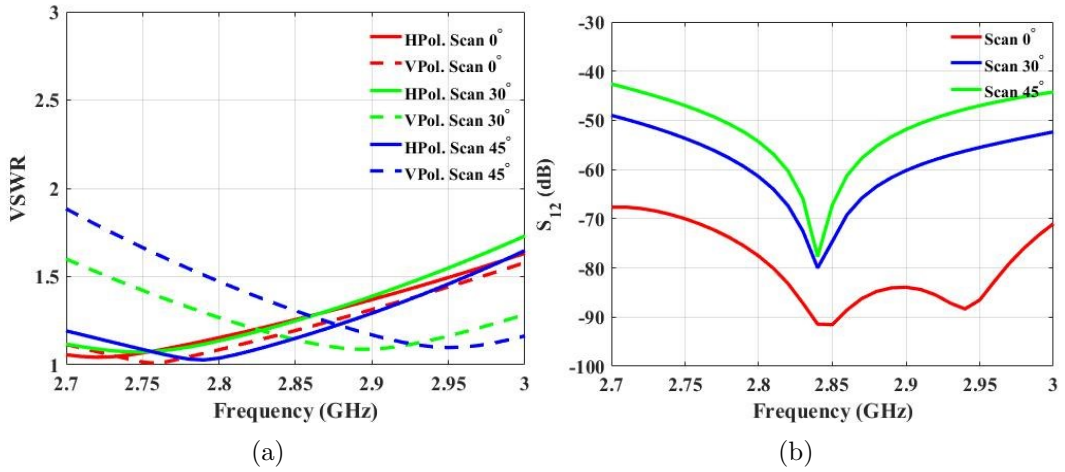


Figure 4.4: Scanning performance of the proposed linear array, (a) active VSWR of crossed dipole element, (b) active port-isolation versus frequency in scanning.

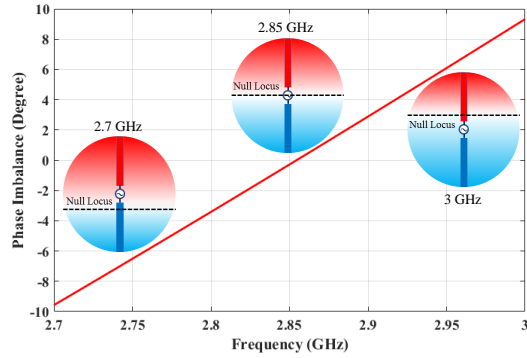


Figure 4.5: Phase imbalance of the half-wavelength balun and its effect on disturbance of the null locus.

4.3 Mirrored Arrangement of Crossed Dipole Elements and Cross-Polarization Reduction

Having an absolutely symmetrical antenna over an entire operational frequency bandwidth is impossible. This issue can be addressed geometrically and electrically. Its geometrical asymmetry can be revealed by considering the balun structure for each polarization in figure 4.3. It consists of two branches of different lengths and is excited from one side. This adds to the electrical asymmetry of the antenna.

Regardless of whether a crossed dipole is excited differentially or by a half-wavelength balun, it is difficult to achieve ideal differential signals within the entire frequency bandwidth. The phase imbalance of the baluns, as shown in figure 4.5, is often optimized at a center frequency and increases toward the beginning and the end of the frequency bandwidth. As such, at these margin frequencies, the peak of the copolar patterns of the dipoles are tilted about $\pm 0.5^\circ$ to one side in their corresponding E-planes and their cross-polarization levels increase. In order to return the symmetry to a linear array antenna with respect to its center and compensate for the beam tilt of the elements,

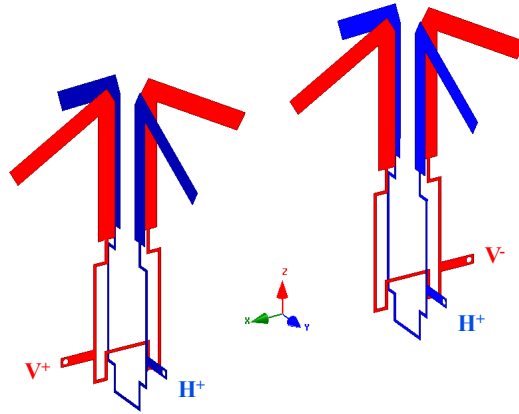


Figure 4.6: The proposed imaged arrangement for the linear array antenna.

the configuration that is shown in figure 4.6 is proposed. In this representation of the two linear elements, the vertical elements are mirrored with respect to yz plane (also bisector of the linear array) while the horizontal ones are identically oriented. Ports marked “-” are excited 180° out of phase with respect to ports marked “+” to have the co-polar fields of the vertical polarizations add in-phase toward boresight. This arrangement will be expanded to two orthogonal directions for the planar array in the next chapter. Detailed discussion will be provided therein.

Figure 4.7 displays a prototype of linear array of eight crossed dipoles, fabricated and situated beside each other. The elements are sequentially rotated resulting in an symmetric imaged arrangement of the linear array antenna. It was measured at the far-field anechoic chamber having an AUT-to-probing-device distance of 10 m. The radiation pattern of each individual element was measured and combined with uniform weighting using MATLAB. The pattern measurement results for both polarizations, provided in figure 4.8, are used to verify the simulation. As expected, the lowest cross polarization occurs at the center frequency where the balun has zero phase imbalance. Nevertheless, the cross-polarization levels remain below -43 dB over the entire frequency

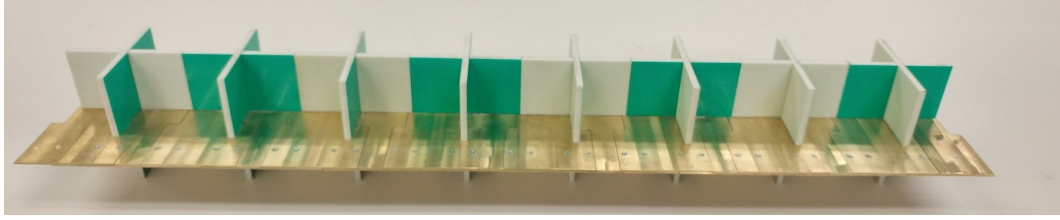


Figure 4.7: A prototype of 8 imaged crossed dipole linear array antenna.

range. This desirable performance can benefit the polarimetric measurement in distinguishing different drops.

4.4 Embedded Element Pattern of the Proposed Antenna in CPPAR

As was mentioned earlier, the purpose of designing the proposed linear array was to replace the current frequency scanning antenna on the CPPAR. Therefore, the radiation properties of the proposed element should be characterized in a cylindrical array environment. Regarding this problem, various solutions have been proposed. Modal approach was used to study the mutual coupling between waveguide elements of a cylindrical array [66]. The embedded element pattern of a cylindrical array was obtained, using the concepts of eigen excitations [67]. The cylindrical form of Floquet theory and the method of moments are respectively proposed in [68] and [69] to analyze a cylindrical array of axial dipoles. Although these solutions are feasible for cylindrical array characterization, they will be complicated and time-consuming for complex antennas and large dimensions.

High Frequency Structure Simulator (HFSS) is capable to simulate a variety of EM structures, using finite-element method (FEM). With increasing access to fast and large-memory computational resources, we are able to sim-

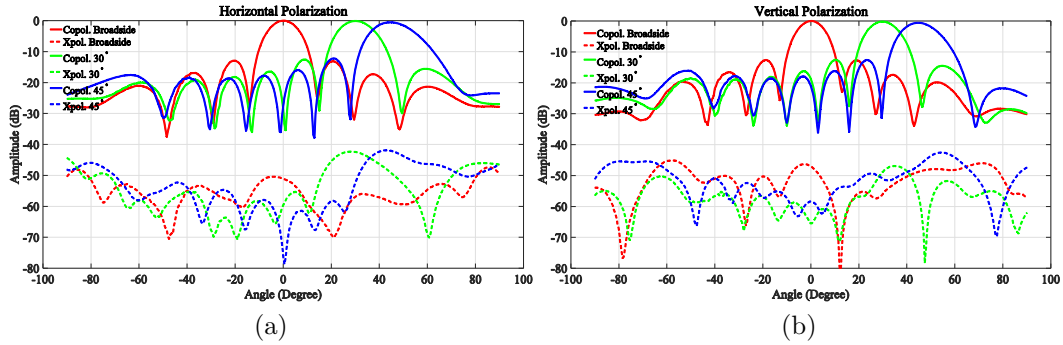


Figure 4.8: Scanning performance of the proposed linear array, (a) horizontal polarization, (b) vertical polarization.

ulate more complicated geometries. However, simulations of large arrays are still computationally prohibitive. We use a fast unit cell approach herein to obtain the embedded element pattern of an arbitrary antenna [70]. Motivated by Floquet’s theorem for periodic structures, HFSS offers the ability to implement periodic boundary conditions (master/slave) to specific faces in the simulation environment. This approach leverages the parallel computational capability and yields precise results. The proposed technique is general and can be used by any other commercially electromagnetic (EM) solver that support periodic boundary conditions. Therefore, it can be widely adopted by engineers and researchers to analyze arbitrary element structures in cylindrical phased arrays.

4.4.1 Implementation of Proposed Unit Cell Method

A conceptual model of a cylindrical array of simple vertical dipoles is shown in figure 4.9a. Our objective is to extract an azimuth cut of an embedded element pattern of the element at a specific elevation angle (θ). To simplify the problem, each column of elements, lying on a ϕ =constant angle, can be replaced by an equivalent element denoted “column element”. Then the prob-

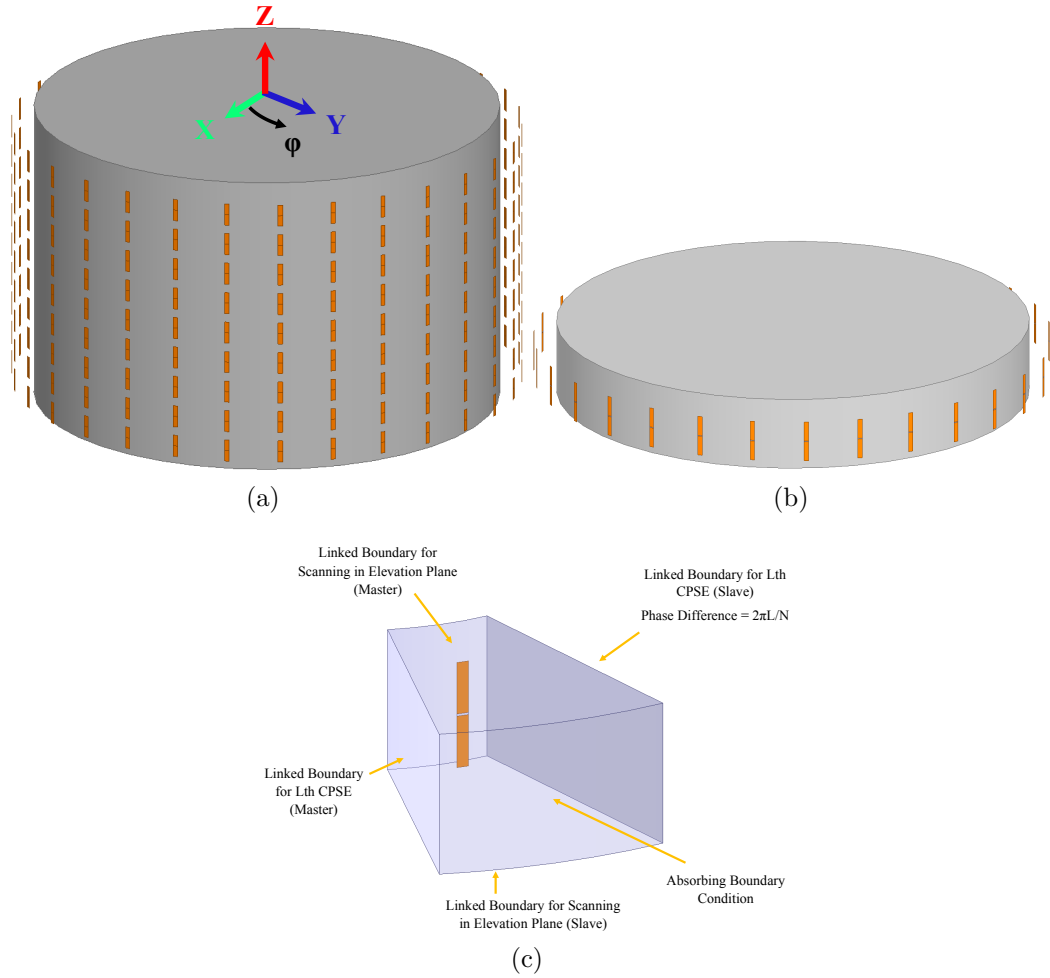


Figure 4.9: (a) A cylindrical array of vertical dipole elements, (b) equivalent circular array of column elements, (c) unit cell of a column element.

lem of a cylindrical array of elements will be simplified to a circular array of column elements, as shown in figure 4.9b. Each of these column elements has a narrow beam in elevation and the field at the peak is proportional to the single embedded element pattern. The indices of the column elements, denoted by $l = 0, 1, \dots, N-1$, show their angular location in the circular array. To obtain the embedded element pattern, the column centered at $\phi=0$ is excited while terminating the others in matched loads. Considering the periodicity of the excitation of the zeroth column element with respect to ϕ , one can express it

as a finite discrete spectrum of angular harmonics

$$\delta_l^0 = \frac{1}{N} \sum_{n=0}^{N-1} \exp(-jn\phi_l), \quad (4.1)$$

where $\phi_l = 2\pi l/N$. These angular harmonics $\exp(-jn\phi_l)$ are the set of cylindrical phase sequence excitations (CPSEs) of the array, with uniform excitation coefficient. Each of these CPSEs corresponds to an electric field harmonic $E^l(\theta, \varphi)$, which the final embedded pattern will be made from their normalized summation expressed as:

$$E_{emb}(\theta, \varphi) = \frac{1}{N} \sum_{n=0}^{N-1} E^l(\theta, \varphi), \quad (4.2)$$

where the harmonics of $E^l(\theta, \varphi)$, corresponded to each CPSE, can be approached as a cylindrical unit cell problem in HFSS. An example of this unit cell is provided in figure 4.9c. This unit cell models a situation where the column element of dipoles is excited by the l th CPSE, and each of the individual dipoles in the column is excited so that the beam is scanned to an elevation angle of θ_{scan} . The fields along the $\phi =$ constant planes are of identical magnitude and a $2\pi l/N$ phase shift between them. Similarly, $Z =$ constant planes include identical fields with a phase difference of $k_0 d_z \sin(\theta_{scan})$, so that the beam is scanned to elevation angle of θ_{scan} . These phase differences can be enforced through linked (master/slave) boundary conditions in HFSS. The analysis for all of the CPSEs, i.e., $l = 0, 1, \dots, N-1$, can be carried out in parallel in HFSS. It is unlike the inversion of large sparse arrays, which typically requires more complex parallelization mechanisms [23].

Let the output of HFSS be denoted by E_{HFSS} for the l th CPSE. The $E^l(\theta_{scan}, \varphi)$ can be obtained by a sequence of phase shifting of E_{HFSS} in Matlab

as:

$$E^l(\theta_{scan}, \varphi) = \sum_{n=0}^{N-1} E_{HFSS}^l(\theta_{scan}, \varphi - n\frac{2\pi}{N})e^{j\frac{2\pi}{N}nl}. \quad (4.3)$$

Using (4.2) and (4.3), we can calculate the final embedded radiation pattern of the array element by

$$E_{emb}^l(\theta_{scan}, \varphi) = \frac{1}{N} \sum_{l=0}^{N-1} \sum_{n=0}^{N-1} E_{HFSS}^l(\theta_{scan}, \varphi - n\frac{2\pi}{N})e^{j\frac{2\pi}{N}nl}. \quad (4.4)$$

The procedure of obtaining embedded element pattern on a cylindrical structure can be summarized as follows.

In HFSS:

1. Apply phase shift to $Z = \text{constant}$ planes based on elevation scan angle.
2. Apply phase shift to $\phi = \text{constant}$ planes based on lth CPSE.
3. Analyze the corresponding unit cell problem in HFSS and store it as $E_{HFSS}^l(\theta_{scan}, \varphi)$ for the lth CPSE.
4. Repeat steps 2 and 3 for all of the CPSEs, i.e., $l = 0, 1, \dots, N-1$.
5. Export all the far fields to a postprocessor, e.g., MATLAB.

In a post-processor (such as MATLAB):

1. Apply (4.4) to obtain the final embedded radiation pattern of the element in the array.

4.4.2 Validation of Proposed Unit Cell Method

To verify the proposed approach, we start with a simple and small geometry that can be simulated by full-wave analysis in HFSS. The full wave results

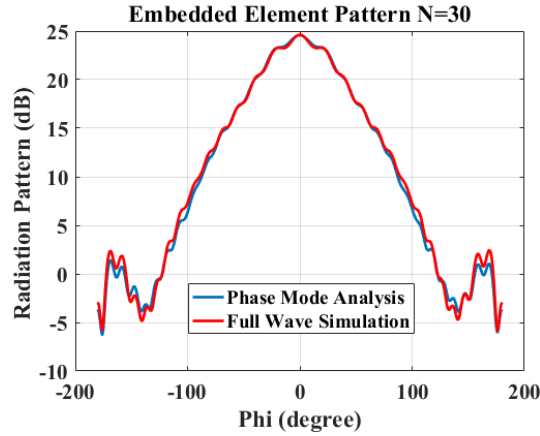


Figure 4.10: A comparison between full wave and unit cell results of a vertical dipole embedded element pattern.

will be compared with those of the proposed solution. Then we will use the unit cell approach to obtain the embedded element patterns of the patch and the crossed dipole on the CPPAR demonstrator. A circular array of 30 vertical dipoles and its corresponding unit cell, like those shown in figure 4.9, are considered. Periodic boundary conditions are imposed on the top and bottom surfaces of both simulations. Therefore, the circular array is a simplified version of an infinite cylindrical array. The radius of the cylinder and the spacing between elements are chosen to be 261 mm and 60 mm, respectively. The embedded element patterns from full-wave and unit cell approaches are provided in figure 4.10. The very good match between the two results shows the feasibility of using phase mode analysis in obtaining the embedded element patterns of more complicated antennas on larger cylinders.

One important objective of proposing the crossed dipole was to remove the substrate over the principal ground plane in order to suppress the surface wave. As the surface wave travels around the cylinder, it radiates and makes some ripples on the copolar pattern. Therefore, its effects can be revealed by examining the radiation characteristics of the patch and the crossed dipole

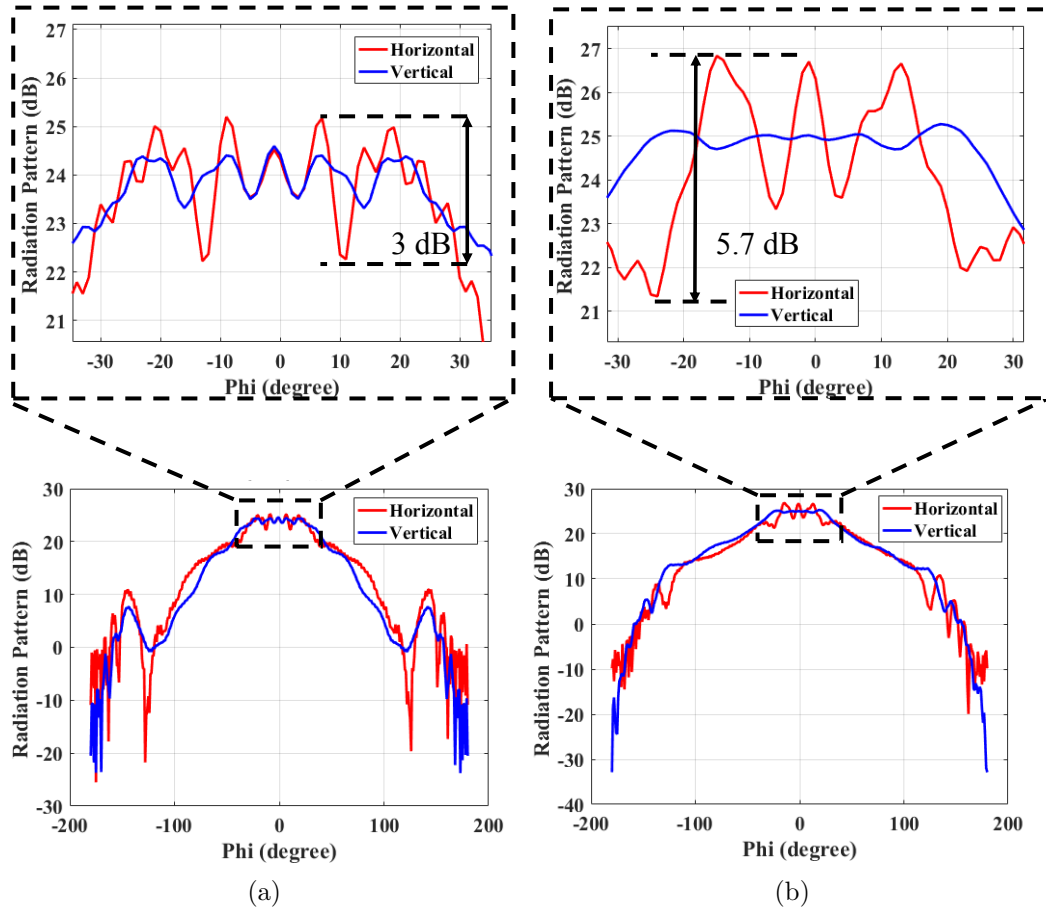


Figure 4.11: A comparison between embedded element patterns of (a) proposed crossed dipole and (b) the stacked patch antenna.

antennas, one with and the other without substrate over the ground plane. The embedded element patterns of these antennas over the same CPPAR ($D = 2$ m) are extracted using unit cell approach and compared in figure 4.11. The ripples around the peak of the copolar patterns are zoomed for the both antennas. The attenuated ripples of the crossed dipole embedded pattern compared to that of the patch antenna, is an evident indication of suppressed cylindrical surface wave. This is an important feature as a better match between copolar patterns can be easily achieved.

Chapter 5

Planar Array Antenna of Crossed Dipoles

5.1 Introduction

The principles of planar phased array antennas (PPAA) have been developed over the past decades [71], and various antenna structures have been adapted for different applications [72], [73]. While improving their features, including, wideband applicability, polarization purity, .etc, researchers have addressed challenges related to PPAA such as mutual coupling, scan blindness, and edge effects [74], [75]. Therefore, PPAA is now a matured technology ready to use in many applications. A planar array antenna is easy to fabricate and this is why it takes priority over other solutions. It has been used for weather surveillance for many years. AN/SPY-1 is a passive array antenna that is shown in figure 5.1a and is comprised of 4,352 elements. This array was used for NOAA's National Weather Radar Test-bed (NWRT) located in Norman, Oklahoma [76].

Multi-function performance, defined by MPAR, requires dual polarization capability. So, the feasibility of polarimetric planar phased array antennas (PPAA) and its related challenges are to be determined in advance. Ten-panel, as shown in figure 5.1b, is a planar phased array solution comprised

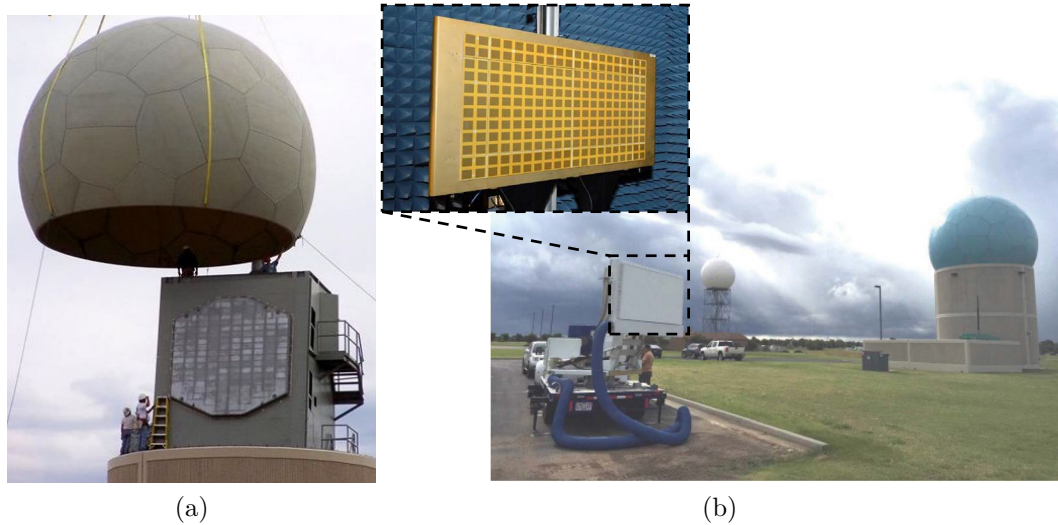


Figure 5.1: (a) NOAA's National Weather Research Testbed (NWRT), (b) The MPAR 10-panel proof of concept demonstrator (From [1]).

of blocks of 8 by 8 dual polarized patch antennas. This array, designed by MIT's Lincoln Laboratory, is used in an S-band dual-pol radar which obtained promising results. The blocks are arranged side-by-side and fabricated by inexpensive printed circuit board technology. The design also allows for the compact integration of T/R modules at the back of the antenna. The patch antennas in each block are excited differentially which has proper performance. Differential excitation and its properties were thoroughly discussed in Chapter 2. In this specific design, the differential signals are made in a separate module at the back of the antenna. Regarding a large number of elements in a big array, it would be far more cost-effective, if the differential feed could be integrated into the antenna. Moreover, the drawback of using a thick grounded substrate and the surface wave excitation were discussed in the previous chapter. This issue could be resolved by designing an antenna which does not require thick substrate over the ground plane. This opens the door to alternatives to the Ten-panel planar array antenna.

It is the purpose of this chapter to propose a new polarimetric planar phased array antenna with higher performance. The modified version of the crossed dipole antenna, discussed in chapter 2, is utilized as the element of the array. Its dimensions will be adjusted in an infinite array using periodic boundary conditions. Each polarization is excited by a balun feed which requires a single connector. So, compared to Ten-panel antenna, the number of required connectors is halved, reducing the cost and assembly process. Unlike the patch antenna, the proposed crossed dipole does not need a thick substrate over the ground plane. Therefore, suppression of the surface wave in both orthogonal directions will be beneficial to matching two copolar beams. Added to these features are the center fed excitation and symmetry of the element in both orthogonal directions. Such a feature and its effect on the side lobe suppression of large arrays will be discussed in the following. Finally, it is worth mentioning that the proposed element, though non-planar, is fabricated by inexpensive PCB technology.

5.2 Array Antenna Geometry and Design

Figure 5.2 shows the geometry of the proposed 6 by 6 planar array antenna with its respective crossed dipole element in the subset of the figure. Part of the substrate is removed to display the radiation elements between the two slabs. Each polarization of the element comprises a balun, a parallel line, and a dipole, all sandwiched between two RO 4003 substrates. Figure 5.3 depicts the impedance match from the SMA connector to the dipole. The 50Ω SMA connector excites the stripline that splits into two 100Ω lines at point “a”. After experiencing two different lengths, which provides 180° phase shift, the signals at the output of the differential traces add in series at point “b”. This

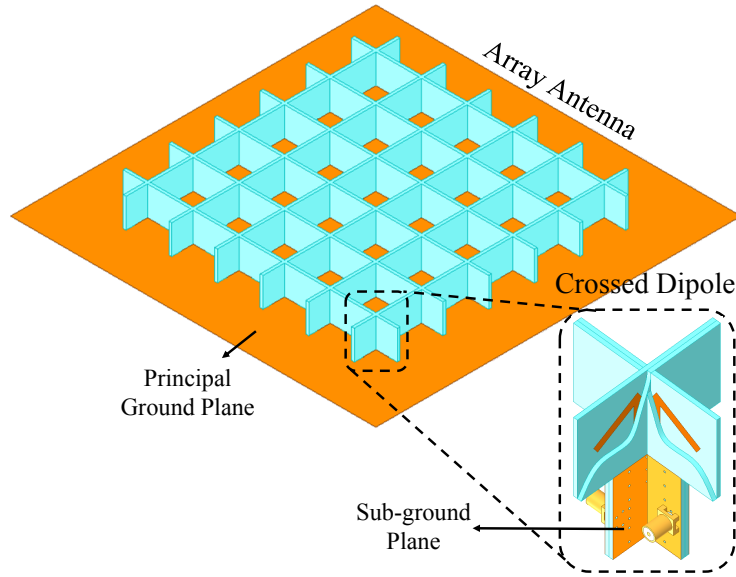


Figure 5.2: Geometry of the proposed array antenna and its respective crossed dipole element.

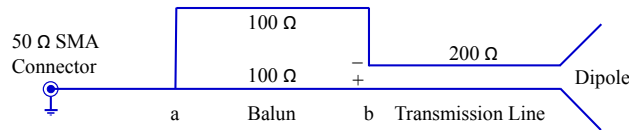


Figure 5.3: Impedance transformation from the SMA connector to the dipole.

forms a 200Ω parallel transmission line which is matched to the dipole input impedance.

This design is based on an infinite periodic array of the proposed crossed dipoles. Therefore, the unit cell approach in HFSS is utilized, taking into account all mutual coupling effects. The unit cell is shown in figure 5.4. The unit cell width is equal to 50 mm , ($0.5 \lambda_H$) where λ_H is the free space wavelength at the highest design frequency of 3 GHz . The proposed crossed dipole is characterized by its three parameters: L (length of the dipole), W (width of the dipole), and Ψ (bend angle of the dipole). We used the first two parameters to match the dipole over the desired frequency range, and then the bend angle was adjusted to obtain the optimum scan element pattern. Using a 1.524 mm

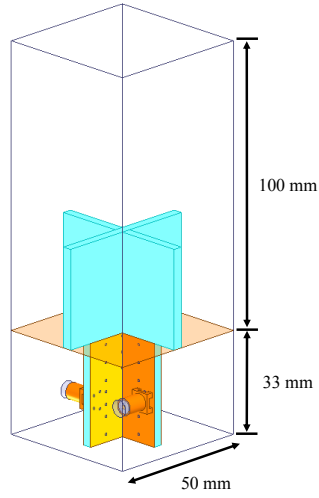


Figure 5.4: Unit cell of proposed crossed dipole.

thick board of Rogers 4003, the optimal dipole dimensions are found to be $L = 44$ mm and $W = 3$ mm.

The E-plane scan element pattern (SEP), formally called the active element pattern [77], is provided in figure 5.5 for different bend angles. This SEP includes the element pattern with all mutual coupling accounted for. Thus, the overall array pattern (ignoring edge effects) can be computed using the scan element pattern and array factor for a given finite array size and lattice [78]. It was traditionally demonstrated [62], and also verified by our simulation that a bent dipole with a bend angle of 30° has the optimum SEP compared to a straight dipole. It is shown that the proposed array antenna can scan far beyond 45° in the principal planes, and this feature demonstrates the feasibility of the proposed array antenna for planar structures.

The active VSWR of the proposed antenna in scanning is given in figure 5.6a. As seen, both polarizations are matched across the bandwidth (VSWR < 2 from 2.7-3 GHz) even in scanning to 45° in the principal planes. The antenna is able to keep its two polarization isolated while scanning in the principal planes. This can be revealed from active S_{12} of the antenna, as

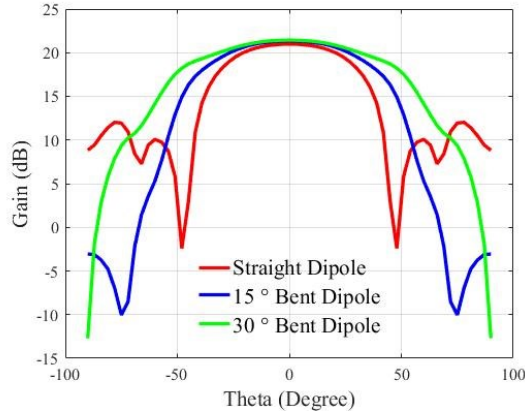


Figure 5.5: Scan element pattern of the proposed crossed dipole in E-plane.

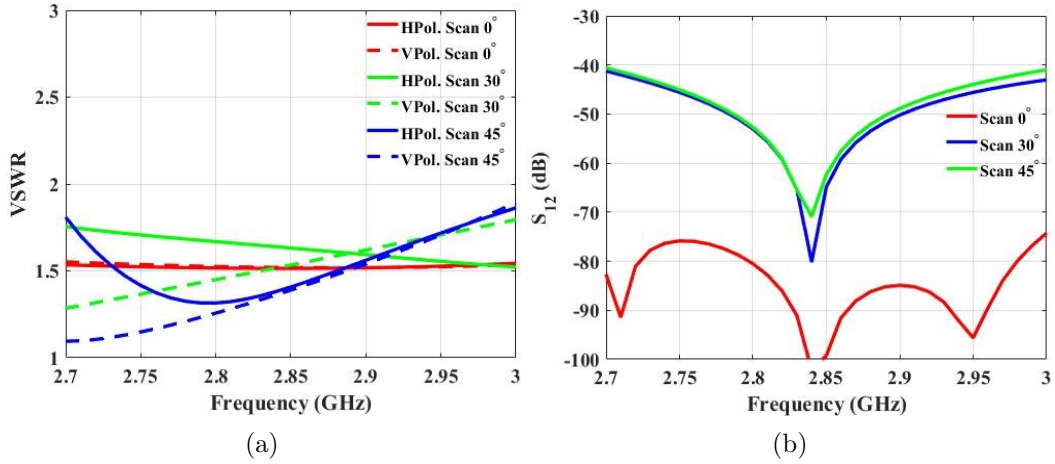


Figure 5.6: Simulated (a) active VSWR and, (b) active port-isolation of the proposed crossed dipole versus frequency in scanning.

shown in figure 5.6b, which remains below -40 dB even in severe scanning.

5.3 Imaged Arrangements of Crossed Dipole Elements and Radiation Characterization of Proposed Planar Array

Defined as a fundamental feature of the array antenna, polarization purity has been frequently discussed in the literature where various solutions to enhance

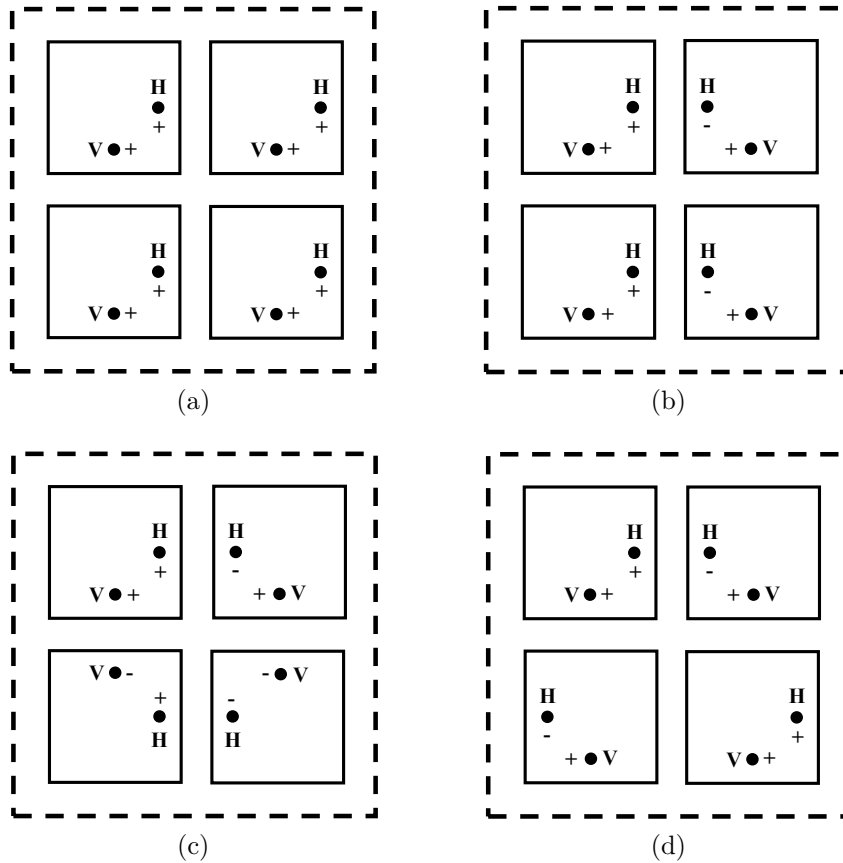


Figure 5.7: Different 2×2 subarray configurations, (a) Configuration A, (b) Configuration B, (c) Configuration C, and (d) Configuration D (Concept from [81]).

it are proposed [79]. Reducing the cross-polarization radiation of an array antenna could be accomplished either in the element scale or in the array scale. The former is continuously being studied for different types of antennas [80]. Alternatively, the cross-polarization suppression can be carried out by sequential rotation of the elements in an array scale. However, it is not a straightforward process and is accompanied by some undesired side effects.

Reference [81] discussed the four possible configurations of a dual linear polarized microstrip patch antenna array. The 2×2 element subarray configurations are provided in figures 5.7a-5.7d, and referred to as configuration A,

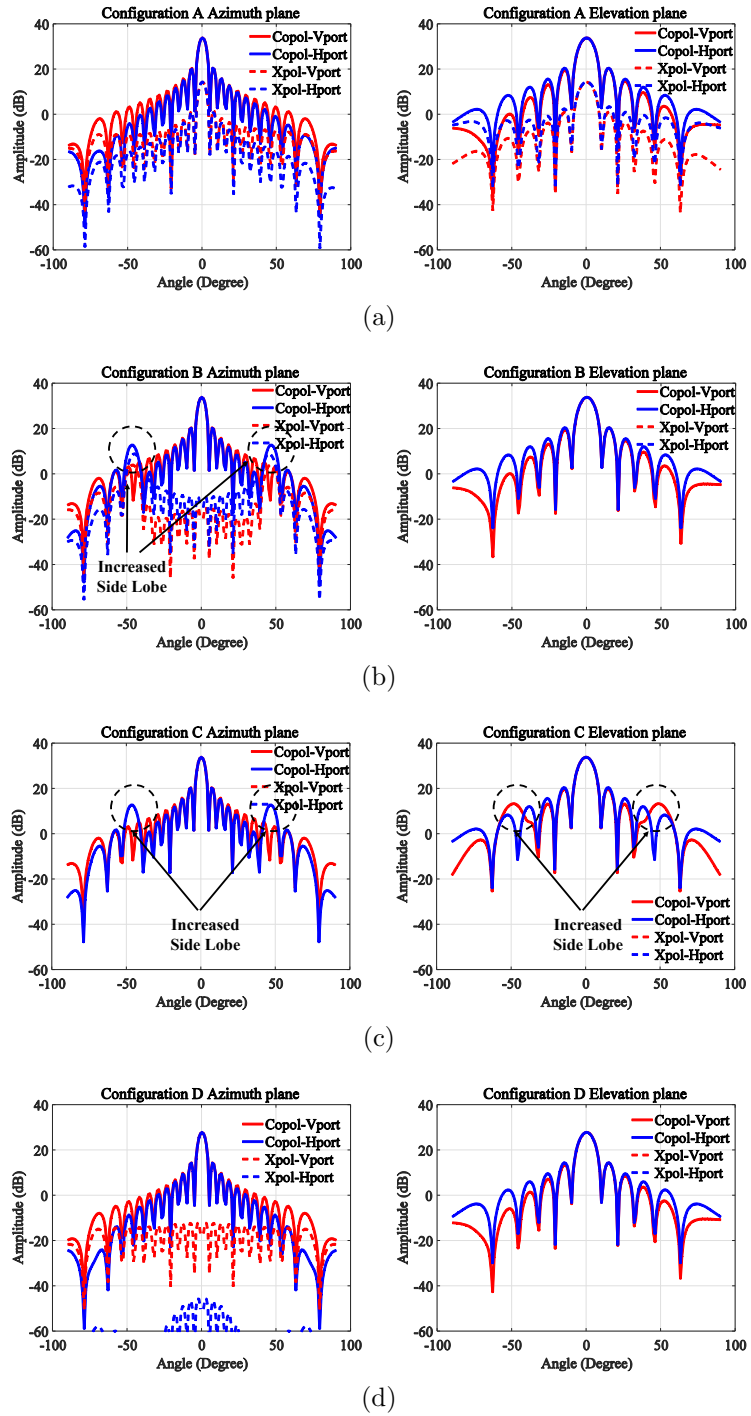


Figure 5.8: 16×8 planar patch array antenna gains in principal planes, (a) Configuration A, (b) Configuration B, (c) Configuration C, and (d) Configuration D.

B, C, and D, respectively. The dots mark the locations of the feed ports, and signals applied to “H” and “V” are primarily intended to generate horizontally and vertically polarized fields, respectively. Ports marked “-” must be excited 180° out of phase with respect to those marked “+” to have the copolar components add in-phase toward boresight. The geometrical and radiation properties of the above configurations are thoroughly discussed in [81]. We duplicated the original patch antenna in [81], and its corresponding 16×8 planar array gains for different configurations in figure 5.8. As seen, cross polarization reduction is obtained at the cost of increased side lobe levels in some configurations. A brief description of all four configurations in terms of the cross polarization level and the increased side lobe issue are provided in Table 5.1 and Table 5.2 for both principal planes. These indicate that minimum cross polarization without side lobe problem is not feasible in single-sided excitation patch antenna array. To achieve the least cross polarization and concurrently avoid the side lobe issue, a two-step rotation is proposed in [81].

In the following, we will identify the reason for increased side lobe in the imaged array configurations by examining the radiation characteristics of the element. The requirement of the element radiation pattern to eliminate the increased side lobe is theoretically calculated and related to the symmetry of the element. We will show how our proposed crossed dipole can obtain lowest cross polarization without side lobe problem [82].

5.3.1 Notation and Terminologies

Before embarking on the detailed discussion, it is helpful to establish a framework and briefly introduce the notations and applied assumptions. As shown in figure 5.9, the array elements are located in a rectangular grid in the xy plane

Table 5.1: A comparison between patch antenna array performances in different configurations in azimuth plane.

Configuration	X-Polarization in Azimuth Plane	H-port Side Lobe in Azimuth Plane	V-port Side Lobe in Azimuth Plane
Conf. A	High	✓	✓
Conf. B	Low	×	✓
Conf. C	Zero	×	✓
Conf. D	Low	✓	✓

Table 5.2: A comparison between patch antenna array performances in different configurations in elevation plane.

Configuration	X-Polarization in Elevation Plane	H-port Side Lobe in Elevation Plane	V-port Side Lobe in Elevation Plane
Conf. A	High	✓	✓
Conf. B	Zero	✓	✓
Conf. C	Zero	✓	×
Conf. D	Zero	✓	✓

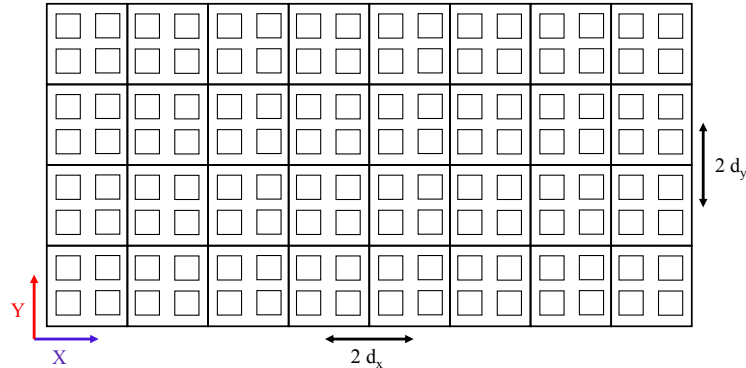


Figure 5.9: 16×8 planar array including 8×4 identical 2×2 subarrays.

and the orientation of the spherical coordinate system is utilized to describe the radiation pattern $\overline{E}(\theta, \varphi)$. The xz and yz planes are designated as azimuth and elevation planes, respectively. The applied power to ports “H” and “V” are intended to generate horizontally and vertically oriented fields, respectively. However, in practice, there always exists some level of cross-polarization. Fol-

lowing the same notation in [81], the co- and cross-polarizations for the two ports are expressed as

$$\bar{E}^H(\theta, \varphi) = \begin{Bmatrix} E^{Hh}(\theta, \varphi) \\ E^{Hv}(\theta, \varphi) \end{Bmatrix} \quad (5.1)$$

$$\bar{E}^V(\theta, \varphi) = \begin{Bmatrix} E^{Vh}(\theta, \varphi) \\ E^{Vv}(\theta, \varphi) \end{Bmatrix} \quad (5.2)$$

where H and V denote the excitation ports, whereas h and v show their respective horizontally and vertically polarized components. Therefore, $E^{Hh}(\theta, \varphi)$ and $E^{Vv}(\theta, \varphi)$ denote the copolar components for the horizontal and vertical polarizations, respectively. Ludwig's third definition is adapted in this work [83].

Any radiation pattern in a principal plane can be decomposed into its even and odd components with respect to the orthogonal principal plane. For instance, the even and odd components of the azimuth plane radiation pattern with respect to the elevation plane can be expressed as

$$\begin{aligned} \bar{E}(\theta, \varphi) &= \begin{Bmatrix} E^h(\theta, \varphi) = E^{he}(\theta, \varphi) + E^{ho}(\theta, \varphi) \\ E^v(\theta, \varphi) = E^{ve}(\theta, \varphi) + E^{vo}(\theta, \varphi) \end{Bmatrix} \\ E^e(\theta, \varphi) &= \frac{E(\theta, \varphi) + E(\theta, \pi - \varphi)}{2} \\ E^o(\theta, \varphi) &= \frac{E(\theta, \varphi) - E(\theta, \pi - \varphi)}{2} \end{aligned} \quad (5.3)$$

where $E^e(\theta, \varphi)$ and $E^o(\theta, \varphi)$ denote the even and odd components of the radiation patterns. In the following sections, we will use these components to calculate the array antenna gains for different configurations.

5.3.2 Pattern Multiplication in Configured Arrays

To have a fair comparison, the same 16×8 planar array in [81] with same properties (interelement spacings $d_x = d_y = 0.7\lambda_0$ where λ_0 is the free-space wavelength) is considered and shown in figure 5.9. The common pattern multiplication can be only applied to configuration A, and due to the sequential rotation of the elements, does not hold for other types of configurations. However, they can be considered as duplications of the 2×2 subarrays, and the multiplication rule can be modified as

$$\bar{E}_{16 \times 8}(\theta, \varphi) = AF_{8 \times 4}(\theta, \varphi) \times \bar{E}_{2 \times 2}(\theta, \varphi) \quad (5.4)$$

where $AF_{8 \times 4}(\theta, \varphi)$ is the normalized array factor for a 8×4 planar array with twice the spacings of the original array, and $\bar{E}_{2 \times 2}(\theta, \varphi)$ is the radiation pattern of a 2×2 subarray. Having a uniformly excited planar array, we can expand $AF_{8 \times 4}(\theta, \varphi)$ as the product of two linear azimuth and elevation array factors

$$\begin{aligned} AF_{8 \times 4}(\theta, \varphi) &= AF_{Az, 8 \times 1}(\theta, \varphi) \times AF_{El, 1 \times 4}(\theta, \varphi) \\ AF_{Az, 8 \times 1}(\theta, \varphi) &= \frac{1}{8} \sum_{i=0}^7 e^{+jk_0(i-7/2)D_x \cos \varphi \sin \theta} = \frac{1}{8} \frac{\sin(16B)}{\sin(2B)} \\ AF_{El, 1 \times 4}(\theta, \varphi) &= \frac{1}{4} \sum_{i=0}^3 e^{+jk_0(i-3/2)D_y \sin \varphi \sin \theta} = \frac{1}{4} \frac{\sin(8C)}{\sin(2C)} \end{aligned} \quad (5.5)$$

$$B = k_0 \frac{d_x}{2} \cos \varphi \sin \theta$$

$$C = k_0 \frac{d_y}{2} \sin \varphi \sin \theta$$

where D_x and D_y in above equations are set to $1.4\lambda_0$. To study the side lobe issue, we narrow down our discussion to H-port patterns for configurations A and B, one with and the other without increased side lobe problem in their corresponding azimuth planes (See Table 5.1). Then the method can be

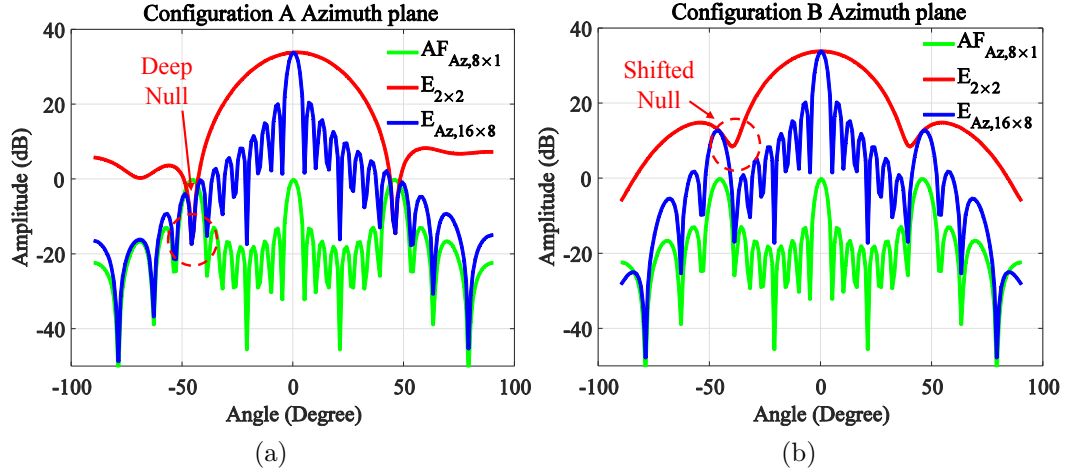


Figure 5.10: Patch array antenna gains in azimuth plane for (a) Configuration A and (b) Configuration B.

readily generalized to include other configurations in any principal plane. In the azimuth plane, the normalized elevation array factor $AF_{EL,1 \times 4}(\theta, \varphi)$ is equal to one. Applying this to (5.4), we can calculate the azimuth plane radiation pattern from

$$\bar{E}_{Az,16 \times 8}(\theta, \varphi) = AF_{Az,8 \times 1}(\theta, \varphi) \times \bar{E}_{2 \times 2}(\theta, \varphi). \quad (5.6)$$

The H-port patterns for configurations A and B in their azimuth planes are plotted in figure 5.10. It is evident that while both configurations have identical array factor $AF_{Az,8 \times 1}(\theta, \varphi)$, the discrepancy in their subarray radiation patterns $\bar{E}_{2 \times 2}(\theta, \varphi)$ gives rise to an increased side lobe level in configuration B. As for configuration A, the sharp null of subarray radiation pattern coincides with the peak of array factor grating lobe and their counteractions suppresses the increased side lobe. However, this is not the case with configuration B as the shifted null of subarray radiation pattern disturbs the balance, resulting in an increased side lobe problem.

5.3.3 Subarrays Radiation Patterns Properties

To discover the discrepancy between the radiation patterns of the subarrays $\overline{E}_{2 \times 2}(\theta, \varphi)$ in different configurations, the 2×2 H-port radiation patterns for configurations A and B in their azimuth planes will be examined. Since both of these configurations have the same duplication in the elevation plane (see figure 5.7), the 2×2 normalized subarray radiation pattern $\overline{E}_{2 \times 2}(\theta, \varphi)$ can be simplified into 2×1 subarray radiation pattern $\overline{E}_{2 \times 1}(\theta, \varphi)$ in the azimuth plane. Figure 5.11 illustrates an element radiation pattern and the orientations of two radiation patterns for a pair of elements in configurations A and B. It should be mentioned that a tilt element radiation pattern is chosen in figure 5.11a to clearly show the pattern rotation in these configurations. When the main beam is pointed to direction phi (φ) in the azimuth plane, the corresponding points of the two element radiation patterns, shown by dashed circles in figure 5.11, add constructively.

5.3.4 Configuration A Subarray Radiation Pattern

This is a straightforward process for configuration A as the elements are simply duplicated with no rotation (Figure 5.11b). Therefore, the electric fields for the left and right elements are identical and can be defined as

$$\overline{E}_L(\theta, \varphi) = \begin{Bmatrix} E^h(\theta, \varphi) \\ E^v(\theta, \varphi) \end{Bmatrix} = \begin{Bmatrix} E^{he}(\theta, \varphi) + E^{ho}(\theta, \varphi) \\ E^{ve}(\theta, \varphi) + E^{vo}(\theta, \varphi) \end{Bmatrix} \quad (5.7)$$

$$\overline{E}_R(\theta, \varphi) = \begin{Bmatrix} E^h(\theta, \varphi) \\ E^v(\theta, \varphi) \end{Bmatrix} = \begin{Bmatrix} E^{he}(\theta, \varphi) + E^{ho}(\theta, \varphi) \\ E^{ve}(\theta, \varphi) + E^{vo}(\theta, \varphi) \end{Bmatrix}. \quad (5.8)$$

The H-port radiation pattern for two elements $\overline{E}_{2 \times 1, A}^H(\theta, \varphi)$ can be calculated by

$$\overline{E}_{2 \times 1, A}^H(\theta, \varphi) = A_L e^{-jB} \overline{E}_L(\theta, \varphi) + A_R e^{+jB} \overline{E}_R(\theta, \varphi). \quad (5.9)$$

Substituting (5.7) and (5.8) into (5.9) with uniform excitation $A_R = A_L = 1/2$, we find

$$\begin{aligned} \overline{E}_{2 \times 1, A}^H(\theta, \varphi) &= \frac{1}{2} e^{-jB} \begin{Bmatrix} E^{Hhe}(\theta, \varphi) + E^{Hho}(\theta, \varphi) \\ E^{Hve}(\theta, \varphi) + E^{Hvo}(\theta, \varphi) \end{Bmatrix} \\ &\quad + \frac{1}{2} e^{+jB} \begin{Bmatrix} E^{Hhe}(\theta, \varphi) + E^{Hho}(\theta, \varphi) \\ E^{Hve}(\theta, \varphi) + E^{Hvo}(\theta, \varphi) \end{Bmatrix} \\ &= \begin{Bmatrix} \cos(B) E^{Hhe}(\theta, \varphi) + \cos(B) E^{Hho}(\theta, \varphi) \\ \cos(B) E^{Hve}(\theta, \varphi) + \cos(B) E^{Hvo}(\theta, \varphi) \end{Bmatrix}. \end{aligned} \quad (5.10)$$

It should be emphasized that the upper and lower expressions in (5.10) correspond to copolar and cross-polar components of the H-port radiation pattern, respectively.

5.3.5 Configuration B Subarray Radiation Pattern

The same process is carried out for configuration B whose pattern rotation and electric field decomposition for the left and right elements are provided in figure 5.11c. For the sake of side-by-side comparison of the signs of electric field components, the same illustration is done for configuration A in figure 5.11b. The electric fields in configuration B for the left and right elements can be defined as

$$\overline{E}_L(\theta, \varphi) = \begin{Bmatrix} E^h(\theta, \varphi) \\ E^v(\theta, \varphi) \end{Bmatrix} = \begin{Bmatrix} E^{he}(\theta, \varphi) + E^{ho}(\theta, \varphi) \\ E^{ve}(\theta, \varphi) + E^{vo}(\theta, \varphi) \end{Bmatrix} \quad (5.11)$$

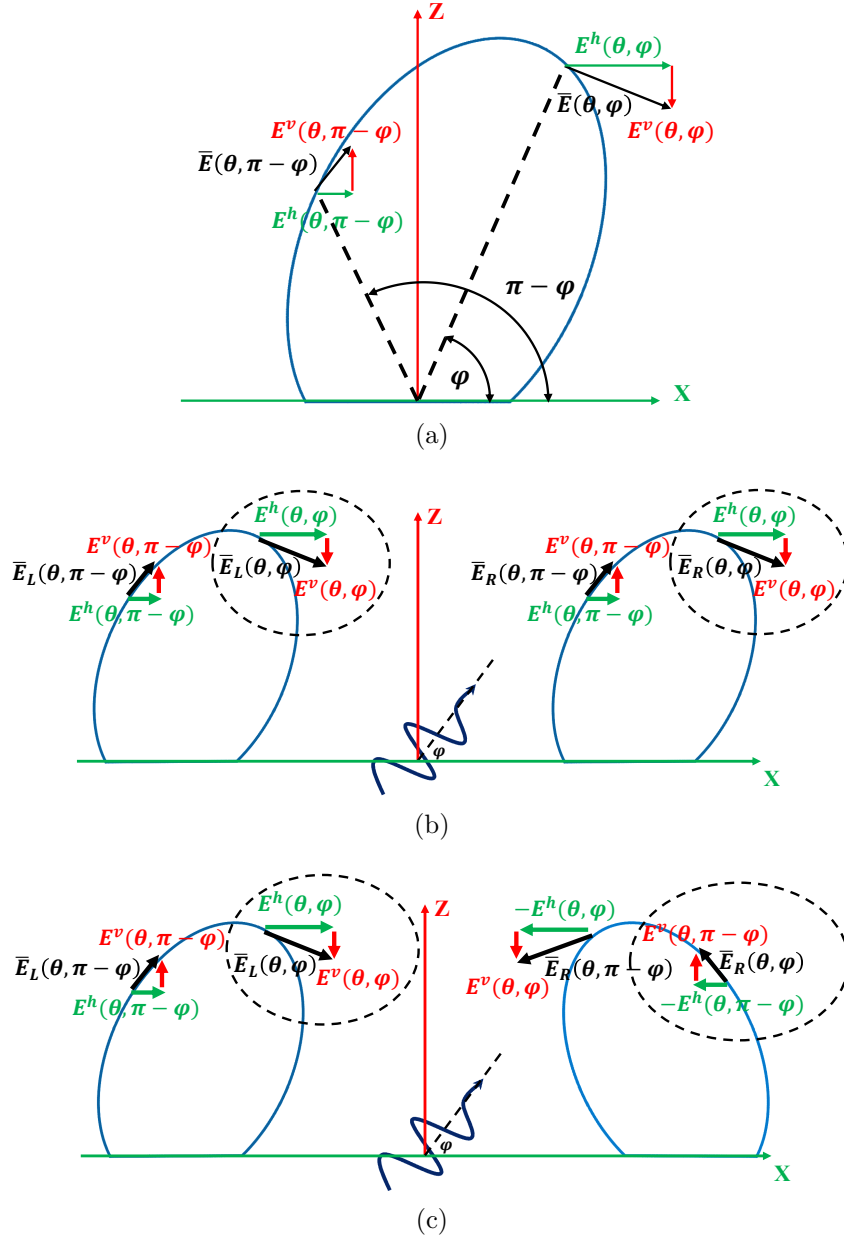


Figure 5.11: Radiation patterns and electric field decomposition in azimuth plane for (a) single element, (b) two elements of configuration A, (c) two elements of configuration B.

$$\begin{aligned}
 \bar{E}_R(\theta, \varphi) &= \begin{Bmatrix} -E^h(\theta, \pi - \varphi) \\ E^v(\theta, \pi - \varphi) \end{Bmatrix} = \begin{Bmatrix} -E^{he}(\theta, \pi - \varphi) - E^{ho}(\theta, \pi - \varphi) \\ E^{ve}(\theta, \pi - \varphi) + E^{vo}(\theta, \pi - \varphi) \end{Bmatrix} \\
 &= \begin{Bmatrix} -E^{he}(\theta, \varphi) + E^{ho}(\theta, \varphi) \\ E^{ve}(\theta, \varphi) - E^{vo}(\theta, \varphi) \end{Bmatrix}.
 \end{aligned} \tag{5.12}$$

Equation (5.9) still holds for this configuration. However, in two polarizations, the H is mirrored with respect to yz plane and the V is kept unchanged. Therefore, they have been excited out of phase ($A_H^L = -A_H^R = 1/2$) and in phase ($A_V^L = A_V^R = 1/2$), respectively, to have their corresponding copolar patterns add in phase at boresight. Substituting these excitation coefficients, we can calculate the H-port two elements radiation pattern $\bar{E}_{2 \times 1, B}^H(\theta, \varphi)$ for horizontal and vertical polarizations

$$\begin{aligned} \bar{E}_{2 \times 1, B}^H(\theta, \varphi) &= \frac{1}{2}e^{-jB} \begin{Bmatrix} E^{Hhe}(\theta, \varphi) + E^{Hho}(\theta, \varphi) \\ E^{Hve}(\theta, \varphi) + E^{Hvo}(\theta, \varphi) \end{Bmatrix} \\ &\quad - \frac{1}{2}e^{+jB} \begin{Bmatrix} -E^{Hhe}(\theta, \varphi) + E^{Hho}(\theta, \varphi) \\ E^{Hve}(\theta, \varphi) - E^{Hvo}(\theta, \varphi) \end{Bmatrix} \quad (5.13) \\ &= \begin{Bmatrix} \cos(B)E^{Hhe}(\theta, \varphi) - j\sin(B)E^{Hho}(\theta, \varphi) \\ -j\sin(B)E^{Hve}(\theta, \varphi) + \cos(B)E^{Hvo}(\theta, \varphi) \end{Bmatrix}. \end{aligned}$$

The different properties of the radiation patterns of two subarrays can be revealed by comparing the copolar components (upper expressions) of (5.10) and (5.13). The copolar component in configuration A has two terms, both with cosine coefficients, whereas its counterpart in configuration B has two terms, one with cosine and the other with sine coefficient. The copolar components of (5.10) and (5.13) along with their two terms are illustrated in figure 5.12a and figure 5.12b, respectively. As can be seen from figure 5.12a, both terms of copolar components in configuration A, with common $\cos(B)$ coefficient result in a deep null in subarray radiation pattern. However, this is not the case with configuration B as the second term with $\sin(B)$ disturbs the null. This term, which has almost a peak at the location of the first term null, increases the null's amplitude and shifts its place. The amount of this displacement

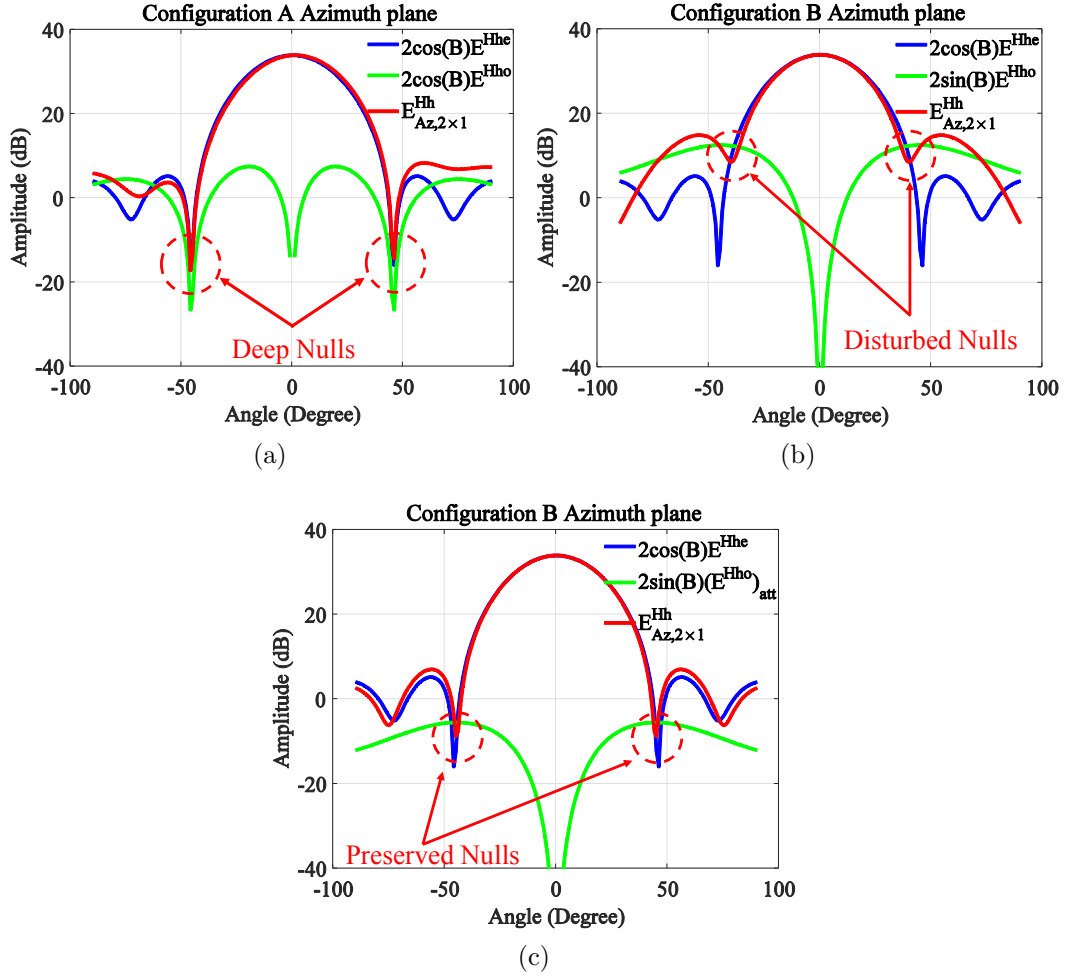


Figure 5.12: 2×1 subarray copolar radiation pattern and its decomposition to its even and odd components in the azimuth plane for (a) Configuration A, (b) Configuration B, (c) Configuration B with attenuated odd component.

depends on the magnitude of the second term $\sin(\beta)E^{Hho}(\theta, \varphi)$. Therefore, it can be inferred that if we have an element radiation pattern with intrinsically low odd copolar component $E^{Hho}(\theta, \varphi)$, then the overall amplitude of the second term would be negligible compared to that of the first term, and the null in the subarray radiation pattern should be preserved. This is shown in figure 5.12c, where the odd copolar component $E^{Hho}(\theta, \varphi)$ for configuration B is intentionally replaced with an attenuated version $E^{Hho}(\theta, \varphi)_{att}$ and its effect

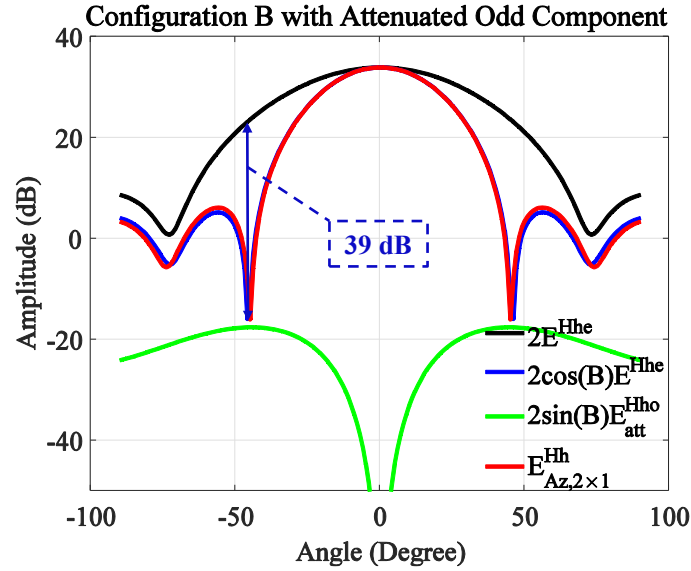


Figure 5.13: 2×1 subarray copolar radiation pattern and its decomposition to its even and odd components for Configuration B with attenuated odd component.

on preserving the null in the subarray radiation pattern is also depicted.

Now the question arises as to how small the odd copolar component $E^{Hho}(\theta, \varphi)$ should be in order to avoid disturbing the null. This is discussed graphically in figure 5.13, where the even copolar component $E^{Hhe}(\theta, \varphi)$, before and after multiplication by $\cos(B)$, is depicted. The coefficient $\cos(B)$ makes a null in the first term pattern by reducing its amplitude by 39 dB at the null location. Therefore, in order to completely preserve the null, the amplitude of the second term must be 39 dB below that of the first term at the null location. Given the unity amplitude of $\sin(B)$ at its maximum, it can be inferred that the amplitude of the odd copolar component $E^{Hho}(\theta, \varphi)$ must be 39 dB below that of even component $E^{Hhe}(\theta, \varphi)$ at the null location.

It is evident from (5.5) that $\cos(B)$ varies by interelement spacing d_x , and consequently changes the location and depth of the null. This variation is depicted in figure 5.14, where three different interelement spacings are consid-

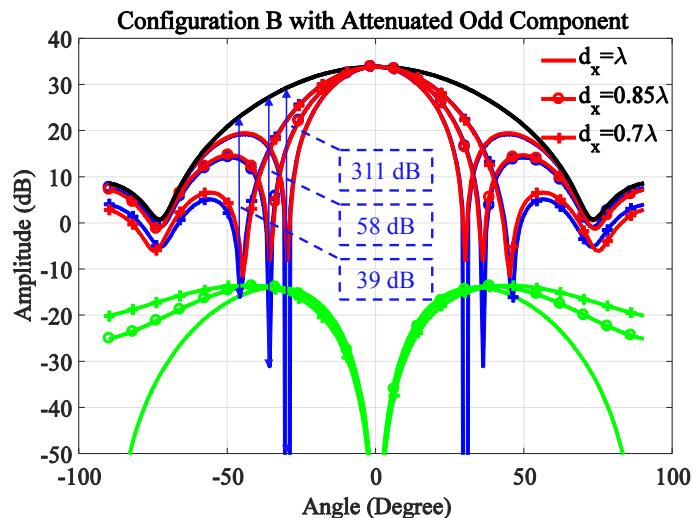


Figure 5.14: 2×1 subarray radiation patterns and their decomposition to even and attenuated odd components for different interelement spacings.

ered. It is shown that with $d_x = \lambda$, at some angles where the B is close to $\pi/2$, the cosine term will have a very sharp null (311 dB). However, it is not required to have a very low corresponding odd component and as shown in figure 5.14, a sufficiently small odd component is adequate to save the null. As a useful rule of thumb it can be concluded that any element radiation pattern with an odd copolar component 35 dB below its even counterpart within an entire plane will not have the side lobe problem in that plane. The following section devotes to our proposed crossed dipole whose radiation pattern satisfies the above-mentioned condition.

5.3.6 The Proposed Element and Its Planar Array Properties

The odd copolar components in the element radiation pattern are identified as the source of the side lobe problem, and the condition to avoid such an issue was specified. It would be informative to briefly discuss where this failure

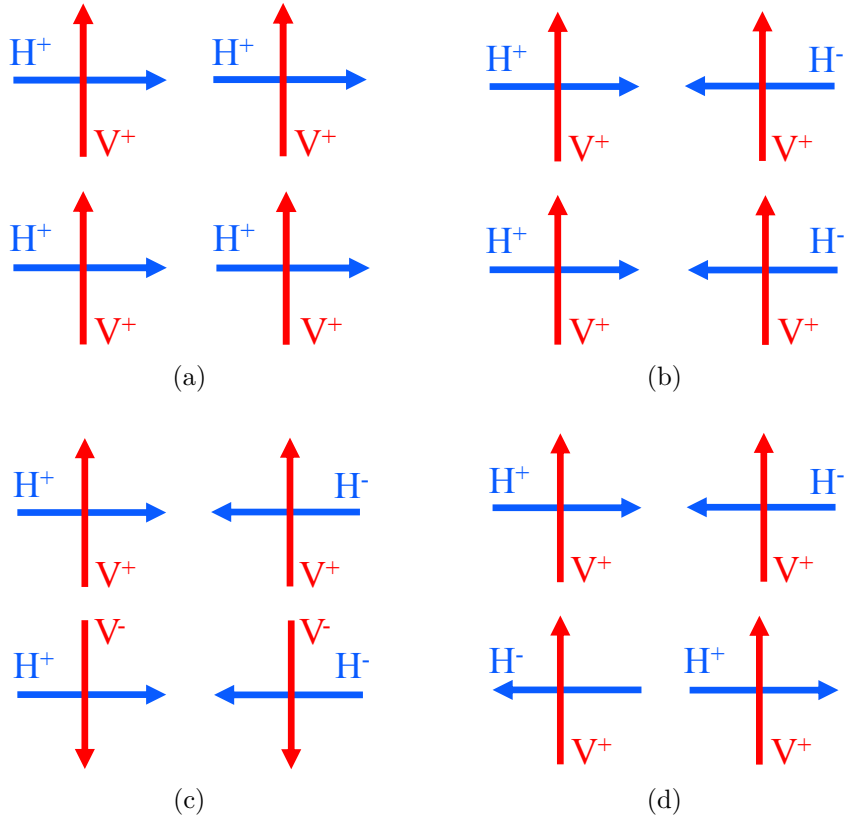


Figure 5.15: Different 2×2 subarray configurations of proposed crossed dipole, (a) Configuration A, (b) Configuration B, (c) Configuration C, and (d) Configuration D.

comes from. Considering the odd component definition of a radiation pattern (3), it can be realized that the asymmetry in the radiation pattern of an antenna with respect to its center results in an increased odd component. This asymmetry is transferred to the antenna near field pattern, and eventually indicates the asymmetrical antenna design with respect to its center. Reference [23] thoroughly discussed this issue in a single-sided excitation patch antenna, which is related to the side lobe problem for the antenna discussed herein. It is mentioned in [23] that the asymmetry of the probe location with respect to the patch center gives rise to the disturbance of fields' phase and amplitude balances in their corresponding E-plane. Such effect dominates as

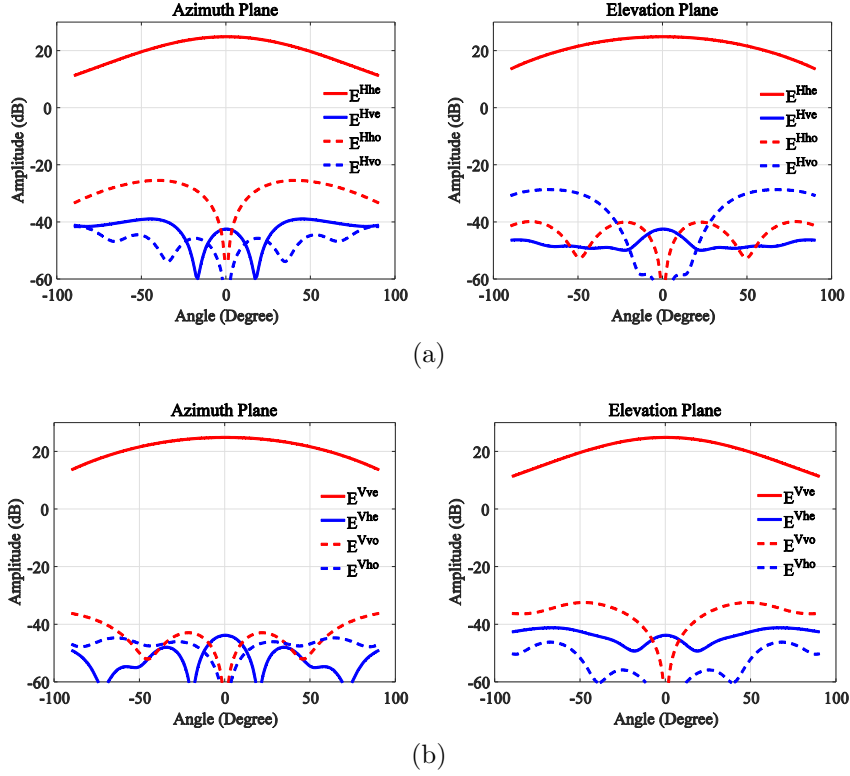


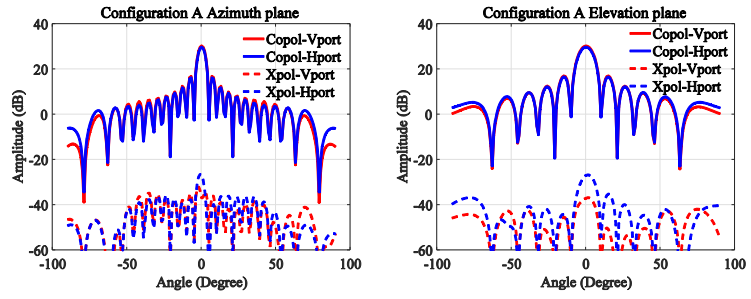
Figure 5.16: Even and odd field components of dual linear polarized crossed dipole antenna for (a) horizontal and (b) vertical polarizations.

the patch thickness and so the probe length increase. This feature is reflected in the increased odd copolar components of the electric fields $E^{Hho}(\theta, \varphi)$ and $E^{Vvo}(\theta, \varphi)$ in their corresponding E-planes.

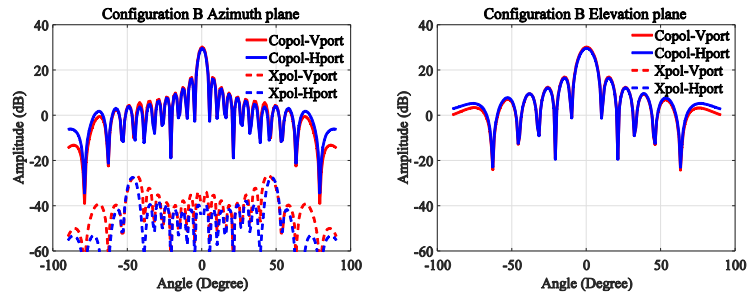
Considering the above asymmetry point, we proposed the symmetrical center-fed crossed dipole with very low cross polarization. Of interest are the even and odd components of the crossed-dipole radiation patterns calculated from the measurement results and provided in figure 5.16. It is clear that all odd copolar components, for both polarizations, are more than 40 dB below the even counterparts in both principal planes, and thus the radiation pattern components satisfy the mentioned requirement. This happens because of the symmetry applied to the design in both principal planes, high port-to-port

isolation, and the center-fed excitation.

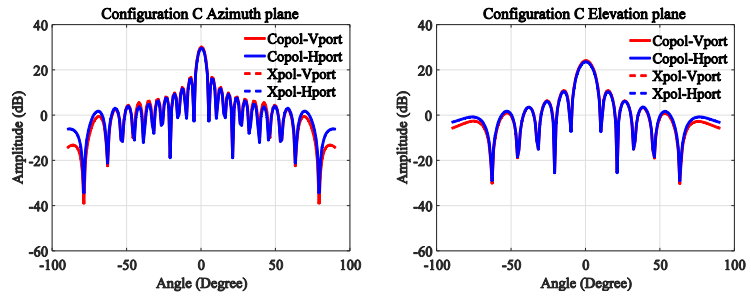
To have a fair comparison, the four different configurations of proposed crossed dipole, shown in figure 5.15, are arranged in the same 16×8 planar array as in [81] with identical properties. To show that the same inference can be applied to any other configuration in either principal plane, the 16×8 crossed dipole array radiation patterns $\overline{E}_{16 \times 8}(\theta, \varphi)$ for all configurations are calculated following the same procedure in [81], and plotted in figure 5.17. By comparing each of these plots with their corresponding patch counterparts, it can be easily revealed that none of the four configurations have side lobe issue. Moreover, better match between two polarizations copolar patterns are achieved, which is beneficial to many applications, including weather observations. It can be seen from figure 5.17c that a crossed dipole array antenna, arranged in configuration C, proposes zero cross-polarization in both principal planes without side lobe problem. This obviates the need for the multilayer imaged arrangement proposed in [81] for patch antenna arrays.



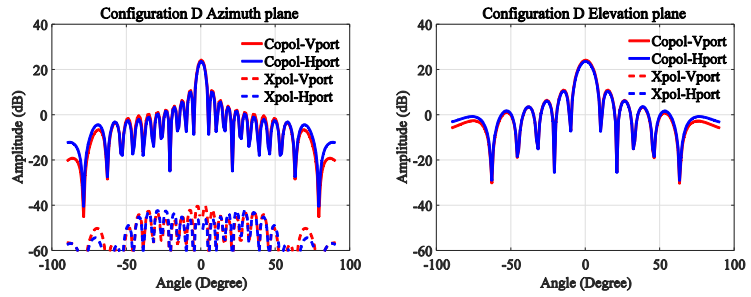
(a)



(b)



(c)



(d)

Figure 5.17: 16×8 crossed dipole planar array gains in principal planes, (a) Configuration A, (b) Configuration B, (c) Configuration C, and (d) Configuration D.

Chapter 6

Conclusions and Future Work

6.1 Introduction

The goal of this research was to develop a new phased array antenna for MPAR. Many stringent system requirements, including high polarization purity, matched copolar patterns, simple and inexpensive geometry are imposed upon the proposed solution. In this work, a novel crossed dipole antenna has been presented to address such requirements.

First, the cross coupling, the port-isolation, and the cross-polarization radiation were discussed for dual-linear polarized antennas. These parameters, as the main focuses of this research, were examined for the reported works in the literature. It was accompanied by compiling and categorizing existing dual polarization antennas into three separate groups. The techniques to enhance the polarization purity in different categories were emphasized. These techniques can be integrated into future antennas with higher performance, opening the door for new application spaces such as phased array weather radar and precise polarization control for communication systems.

Following the points highlighted in chapter 2, we proposed a crossed dipole antenna which meets the MPAR requirements. The proper performance of the

antenna in terms of high port-to-port isolation and the low cross-polarization level was demonstrated. Looking for a perfect match between two polarizations, we have modified the balun structures in a new version of the antenna. Using two identical geometries for the two polarizations, we achieved a pair of matched copolar patterns. This, in turn, allows for accurate weather measurements enabling polarimetric phased array radar to distinguish different hydrometeor types, e.g., rain vs melting snow or hail.

In the next step, we proposed an alternative to the frequency scanning antenna array mounted on the CPPAR. The proposed linear array includes the modified version of the crossed dipole antenna. The elements in the linear array are individually excited, allowing for beam shaping and fast adaptive scanning. Suppressed azimuthal surface wave was achieved by eliminating the thick substrate over the large cylindrical ground plane. This allows for higher isolation between adjacent elements and easier beam shaping. Suppression of the surface wave in terms of attenuated ripples of the copolar patterns was demonstrated with the aid of phase mode analysis. The flexibility and rapid convergence rate of unit cell approach were discussed and verified for proposed crossed dipole.

Finally, a planar polarimetric phased array antenna of the proposed crossed dipole was presented. Its high performance in severe scanning scenario was proven in terms of high port isolation and polarization purity. It was followed by a thorough discussion of side lobe problem in the imaged arrangement of planar array antennas. The requirement of the element radiation pattern to eliminate the increased side lobe is theoretically calculated and related to the symmetry of the element. We demonstrated that our crossed dipole antenna array, arranged in an specific configuration, can have zero cross-polarization

in principal planes without sidelobe problem.

6.1.1 Contributions

- Reviewing the existing dual polarization technology and categorizing them into three different groups.
- Discussing and formulating of the crossed coupling, the port isolation, and the cross polarization for dual-linear polarization antennas.
- Design and fabrication of a novel crossed dipole with high port isolation and low cross-polarization level.
- Design and implementation of a modified crossed dipole antenna with matched copolar beams.
- Design and fabrication of a linear crossed dipole antenna for cylindrical polarimetric phased array antennas.
- Calculation and characterization of the embedded element pattern of a cylindrical array with phase mode analysis.
- Design, development, and implementation of a planar polarimetric phased array antenna for multi-mission applications.
- Demonstration and discussion of the side lobe problem in the imaged arrangement of planar array antennas.

6.2 Future Work

The works presented in this dissertation can be expanded in the following areas.

6.2.1 Wide Bandwidth Crossed Dipole Antenna

From the phase and amplitude imbalance discussion, provided in chapter 2, it can be revealed that the performance of the proposed crossed dipole is limited by the frequency bandwidth of its balun feedline. Having a wideband balun, the proposed solution can have similar isolation over a wider range of frequency. This is not critical for MPAR concerning its operational frequency range. However, it can provide the dipole with a flatter phase imbalance resulting in lower cross-polarization level over the entire frequency range. The principle of Marchand balun has been discovered in 1944 [84], and this balun has evolved into a PCB fabricated version for different applications [85]. Figure 6.1 shows a linear dipole excited by a Marchand balun using stripline structure [86]. We have used the stripline structure for the baluns in our design and that is why we believe that this specific Marchand balun is potentially compatible with our proposed antenna. However, in a dual polarized antenna, careful considerations should be given to the design in order to preserve the high performance of the antenna. This remains as an active future research area in wideband dual polarized applications.

6.2.2 Fully Printed Crossed Dipole over Perfect Magnetic Surface

Using a Perfect Magnetic Conducting (PMC) ground plane, a dipole can be situated in the vicinity of a flat surface [87]. In doing so, the antenna can be fully fabricated by PCB technology reducing the cost and the complexity of design. The current orientations of a dipole and its image, above a PEC and a PMC surface, are compared in figure 6.2. This is a well-known concept, and many studies have been conducted regarding profile miniaturization

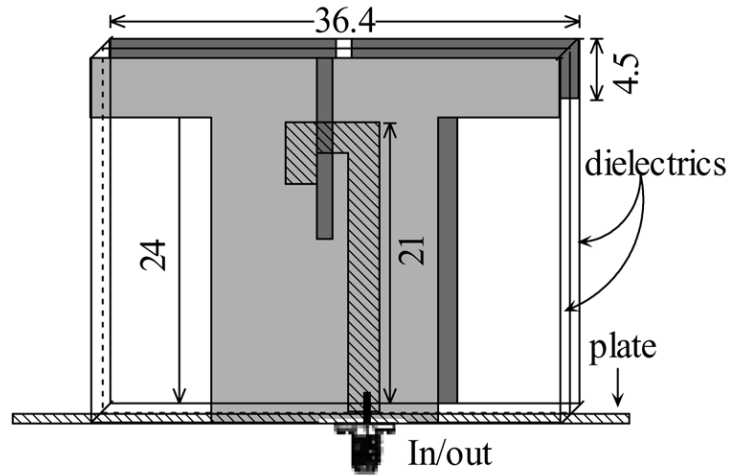


Figure 6.1: A double-layered printed dipole antenna integrated with a Marchand balun.

and bandwidth enhancement of these antennas [88]. A sample design of a dual-band Electromagnetic Bandgap (EBG) Artificial Magnetic Conducting (AMC) ground plane optimized using a Genetic Algorithm (GA) is shown in figure 6.3. This artificial ground plane was designed for dual-band applications at the Pennsylvania State University. The polarization purity of these ground planes are to be investigated quantitatively for multi-mission applications. The diffraction and the edge effects of artificial PMC should be controlled in such a way that do not affect the antenna polarization purity. Implementation of a crossed dipole antenna using this method for dual polarization applications will be of great interest to the antenna community.

6.2.3 Planar Array Antenna with Polarization Purity in and out of the Principal Planes

The planar polarimetric phased array antenna, though easy-to-fabricate, suffers from an intrinsic limitation. When the transmit beam is directed off the

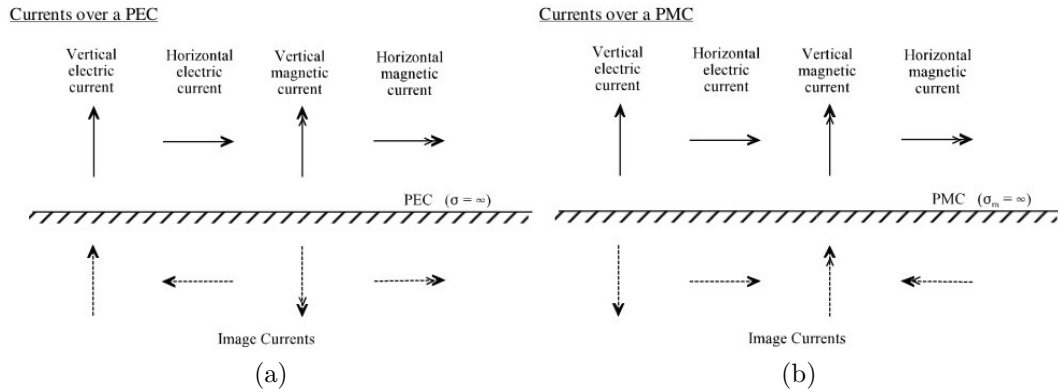


Figure 6.2: Electric and magnetic sources and their images near (a) electric (PEC) and (b) magnetic (PMC) conductors.



Figure 6.3: A sample design of a dual-band Electromagnetic Bandgap (EBG) Artificial Magnetic Conducting (AMC) ground plane fabricated at the Pennsylvania State University.

principal plane, the two polarizations are not orthogonal and the horizontal (vertical) polarization is not parallel (perpendicular) to the surface of the earth. Such effect allows part of the power in the horizontal polarization to be returned in the vertical beam and vice versa. This bias can be compensated by costly and cumbersome calibration, but at the cost of a decrease in the sensitivity. There is an alternative solution which can simplify the complicated calibration process. An antenna with fixed orientations of its two orthogo-

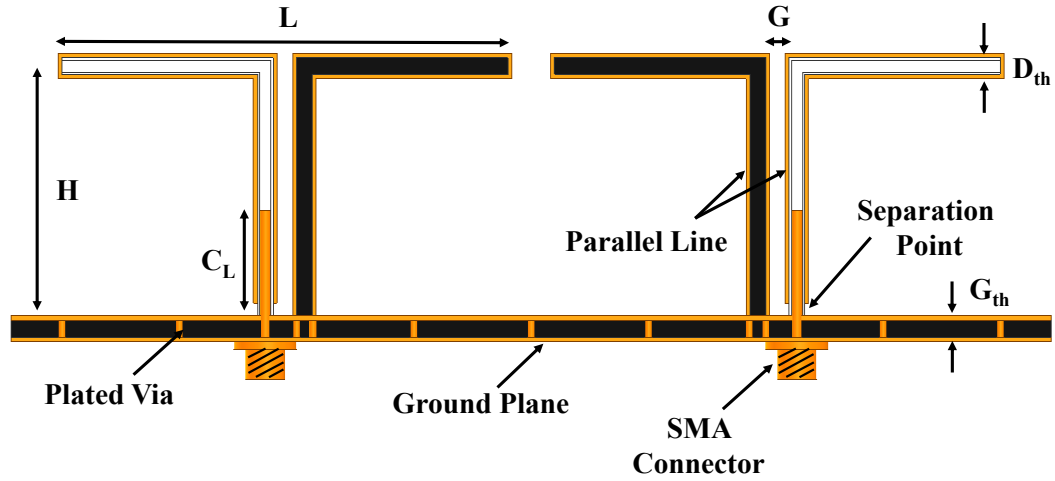


Figure 6.4: A unit cell of two imaged linear dipole antennas. One pole of each dipole is shown transparent to present the excitation method.

nal radiation patterns over the entire volumetric scan will resolve this issue. Having Ludwig's II definition in mind, this antenna could be a slot-dipole or a patch-dipole, both oriented in the z -direction. The slot-dipole solution has been previously touched [1]. It has been concluded that collocation of the two antennas affects each other radiation characteristics. However, we believe that the two elements can be situated in close proximity, and the interference could be handled in such a way that the polarization purity of both antennas can be preserved. This research thrust is of great importance to MPAR community as the planar phased array antennas have been always given priority owing to its ease of fabrication.

6.2.4 3D Printed Crossed Dipole Antenna

Additive manufacturing technologies, often called 3D printing, have received much attention recently. Besides mechanical objects, 3D electromagnetic structures such as waveguides, antennas, lenses, and holographic devices have also been demonstrated recently for a wide range of frequencies. Although it has

been argued that 3D printing could be the future of manufacturing, the potential and applicability of these methods for creating advanced and integrated antenna systems still remain largely unexplored. Additive manufacturing enabled new antennas and electromagnetic structures which may lead to a paradigm change in antenna designs have not been explored much. As part of our ongoing research, we have started to fabricate a single polarized linear dipole array with 3D printing technology. A unit cell of the proposed antenna array is shown in figure 6.4. Detailed discussion on the fabrication procedure and results of the 3D printed linear antenna is provided in Appendix B. The initial results suggest that higher performance can be achieved by an optimum choice of the antenna dimensions and an appropriate plating process. This research thrust could be expanded to include other dual polarization antennas, including crossed dipole, slot dipole, etc.

References

- [1] J. E. Stailey and K. D. Hondl, “Multifunction phased array radar for aircraft and weather surveillance”, *Proceedings of the IEEE*, vol. 104, no. 3, pp. 649–659, 2016.
- [2] R. J. Mailloux, *Phased array antenna handbook*. Artech House Boston, 2005, vol. 2.
- [3] R. Doviak, V Bringi, A Ryzhkov, A Zahrai, and D Zrnić, “Considerations for polarimetric upgrades to operational wsr-88d radars”, *Journal of Atmospheric and Oceanic Technology*, vol. 17, no. 3, pp. 257–278, 2000.
- [4] G. Zhang, *Weather radar polarimetry*. Crc Press, 2016.
- [5] R. L. Jordan, B. L. Huneycutt, and M. Werner, “The sir-c/x-sar synthetic aperture radar system”, *IEEE Transactions on Geoscience and Remote Sensing*, vol. 33, no. 4, pp. 829–839, 1995.
- [6] S. Karimkashi and G. Zhang, “Optimizing radiation patterns of a cylindrical polarimetric phased-array radar for multimissions”, *IEEE Transactions on Geoscience and Remote Sensing*, vol. 53, no. 5, pp. 2810–2818, 2015.
- [7] G. Brown, “Turnstile antenna”, 1941, US Patent 2,267,550.
- [8] Q. Xue, S. W. Liao, and J. H. Xu, “A differentially-driven dual-polarized magneto-electric dipole antenna”, *IEEE Transactions on antennas and propagation*, vol. 61, no. 1, pp. 425–430, 2013.
- [9] M. Mirmozafari, G. Zhang, S. Saeedi, and R. Doviak, “A dual-linear polarized highly isolated crossed dipole antenna for mpar application”, *IEEE Antennas and Wireless Propagation Letters*, vol. 16, pp. 1879–1882, 2017.

- [10] Y. Gou, S. Yang, J. Li, and Z. Nie, “A compact dual-polarized printed dipole antenna with high isolation for wideband base station applications”, *IEEE Transactions on Antennas and Propagation*, vol. 62, no. 8, pp. 4392–4395, 2014.
- [11] Y. Liu, H. Yi, F.-W. Wang, and S.-X. Gong, “A novel miniaturized broadband dual-polarized dipole antenna for base station”, *IEEE Antennas and Wireless Propagation Letters*, vol. 12, pp. 1335–1338, 2013.
- [12] B. Q. Wu and K.-M. Luk, “A broadband dual-polarized magneto-electric dipole antenna with simple feeds”, *IEEE Antennas and Wireless Propagation Letters*, vol. 8, pp. 60–63, 2009.
- [13] W. K. Roberts, “A new wide-band balun”, *Proceedings of the IRE*, vol. 45, no. 12, pp. 1628–1631, 1957.
- [14] H. G. Booker, “Slot aerials and their relation to complementary wire aerials (babinet’s principle)”, *Journal of the Institution of Electrical Engineers-Part IIIA: Radiolocation*, vol. 93, no. 4, pp. 620–626, 1946.
- [15] Y. Li, Z. Zhang, J. Zheng, and Z. Feng, “Compact azimuthal omnidirectional dual-polarized antenna using highly isolated colocated slots”, *IEEE Transactions on Antennas and Propagation*, vol. 60, no. 9, pp. 4037–4045, 2012.
- [16] T. Oh, Y.-G. Lim, C.-B. Chae, and Y. Lee, “Dual-polarization slot antenna with high cross-polarization discrimination for indoor small-cell mimo systems”, *IEEE Antennas and Wireless Propagation Letters*, vol. 14, pp. 374–377, 2015.
- [17] A Constantine Balanias, *Antenna theory analysis and design*, 1982.
- [18] C.-H. Lee, S.-Y. Chen, and P. Hsu, “Isosceles triangular slot antenna for broadband dual polarization applications”, *IEEE Transactions on Antennas and Propagation*, vol. 57, no. 10, pp. 3347–3351, 2009.
- [19] P. K. Mishra, D. R. Jahagirdar, and G. Kumar, “A review of broadband dual linearly polarized microstrip antenna designs with high isolation [education column]”, *IEEE Antennas and Propagation Magazine*, vol. 56, no. 6, pp. 238–251, 2014.

- [20] T. Chiba, Y. Suzuki, and N. Miyano, "Suppression of higher modes and cross polarized component for microstrip antennas", in *Antennas and Propagation Society International Symposium, 1982*, IEEE, vol. 20, 1982, pp. 285–288.
- [21] K. Carver and J. Mink, "Microstrip antenna technology", *IEEE transactions on antennas and propagation*, vol. 29, no. 1, pp. 2–24, 1981.
- [22] J. Huang, "The finite ground plane effect on the microstrip antenna radiation patterns", *IEEE Transactions on Antennas and Propagation*, vol. 31, no. 4, pp. 649–653, 1983.
- [23] S. Bhardwaj and Y. Rahmat-Samii, "Revisiting the generation of cross-polarization in rectangular patch antennas: a near-field approach", *IEEE Antennas and Propagation Magazine*, vol. 56, no. 1, pp. 14–38, 2014.
- [24] L Lewin, "Spurious radiation from microstrip", in *Proceedings of the Institution of Electrical Engineers*, IET, vol. 125, 1978, pp. 633–642.
- [25] M. Cryan and P. Hall, "Integrated active antenna with simultaneous transmit-receive operation", *Electronics Letters*, vol. 32, no. 4, pp. 286–287, 1996.
- [26] S.-S. Zhong, X.-X. Yang, S.-C. Gao, and J.-H. Cui, "Corner-fed microstrip antenna element and arrays for dual-polarization operation", *IEEE Transactions on Antennas and Propagation*, vol. 50, no. 10, pp. 1473–1480, 2002.
- [27] Y. Hu, D. R. Jackson, J. T. Williams, S. A. Long, and V. R. Komanduri, "Characterization of the input impedance of the inset-fed rectangular microstrip antenna", *IEEE Transactions on Antennas and Propagation*, vol. 56, no. 10, pp. 3314–3318, 2008.
- [28] S. Gao, L. Li, T. Yeo, and M. Leong, "Low cost, dual linearly polarised microstrip patch array", *IEE Proceedings-Microwaves, Antennas and Propagation*, vol. 148, no. 1, pp. 21–24, 2001.
- [29] E. Chang, S Long, and W Richards, "An experimental investigation of electrically thick rectangular microstrip antennas", *IEEE Transactions on antennas and propagation*, vol. 34, no. 6, pp. 767–772, 1986.

- [30] K. Gosalia and G. Lazzi, “Reduced size, dual-polarized microstrip patch antenna for wireless communications”, *IEEE Transactions on Antennas and Propagation*, vol. 51, no. 9, pp. 2182–2186, 2003.
- [31] A Petosa, A Ittipiboon, and N Gagnon, “Suppression of unwanted probe radiation in wideband probe-fed microstrip patches”, *Electronics Letters*, vol. 35, no. 5, pp. 355–357, 1999.
- [32] A Kishk and L. Shafai, “The effect of various parameters of circular microstrip antennas on their radiation efficiency and the mode excitation”, *IEEE Transactions on antennas and propagation*, vol. 34, no. 8, pp. 969–976, 1986.
- [33] K. Luk, C. Mak, Y. Chow, and K. Lee, “Broadband microstrip patch antenna”, *Electronics letters*, vol. 34, no. 15, pp. 1442–1443, 1998.
- [34] Z. N. Chen and M. Chia, “Enhanced radiation performance of broadband suspended plate antenna”, in *Antennas and Propagation Society International Symposium, IEEE*, vol. 3, 2001, pp. 290–293.
- [35] H. Wong, K.-L. Lau, and K.-M. Luk, “Design of dual-polarized l-probe patch antenna arrays with high isolation”, *IEEE Transactions on Antennas and Propagation*, vol. 52, no. 1, pp. 45–52, 2004.
- [36] H. Lai and K. Luk, “Wideband patch antenna with low cross-polarisation”, *Electronics Letters*, vol. 40, no. 3, pp. 159–160, 2004.
- [37] D. M. Pozar, “Microstrip antenna aperture-coupled to a microstripline”, *Electronics letters*, vol. 21, no. 2, pp. 49–50, 1985.
- [38] A Adrian and D. Schaubert, “Dual aperture-coupled microstrip antenna for dual or circular polarisation”, *Electronics Letters*, vol. 23, no. 23, pp. 1226–1228, 1987.
- [39] Y Murakami, W Chujo, I Chiba, and M Fujise, “Dual slot-coupled microstrip antenna for dual frequency operation”, *Electronics Letters*, vol. 29, no. 22, pp. 1906–1907, 1993.
- [40] Y Murakami, W Chujo, and M Fujise, “Mutual coupling between two ports of dual slot-coupled circular patch antennas”, in *Antennas and Propagation Society International Symposium, 1993. AP-S. Digest, IEEE*, 1993, pp. 1469–1472.

- [41] S. Hienonen, A. Lehto, and A. V. Raisanen, “Simple broadband dual-polarized aperture-coupled microstrip antenna”, in *Antennas and Propagation Society International Symposium, 1999. IEEE*, IEEE, vol. 2, 1999, pp. 1228–1231.
- [42] S.-J. Li, J. Gao, X. Cao, Z. Zhang, and D. Zhang, “Broadband and high-isolation dual-polarized microstrip antenna with low radar cross section”, *IEEE Antennas and Wireless Propagation Letters*, vol. 13, pp. 1413–1416, 2014.
- [43] D. Pozar and S. Targonski, “Improved coupling for aperture coupled microstrip antennas”, *Electronics Letters*, vol. 27, no. 13, pp. 1129–1131, 1991.
- [44] V. Rathi, G. Kumar, and K. Ray, “Improved coupling for aperture coupled microstrip antennas”, *IEEE Transactions on antennas and propagation*, vol. 44, no. 8, pp. 1196–1198, 1996.
- [45] C. Tsao, Y. Hwang, F Kilburg, and F Dietrich, “Aperture-coupled patch antennas with wide-bandwidth and dual-polarization capabilities”, in *Antennas and Propagation Society International Symposium, 1988. AP-S. Digest*, IEEE, 1988, pp. 936–939.
- [46] S. D. Targonski and D. M. Pozar, “Design of wideband circularly polarized aperture-coupled microstrip antennas”, *IEEE Transactions on Antennas and Propagation*, vol. 41, no. 2, pp. 214–220, 1993.
- [47] M Edimo, A Sharaiha, and C Terret, “Optimised feeding of dual polarised broadband aperture-coupled printed antenna”, *Electronics Letters*, vol. 28, no. 19, pp. 1785–1787, 1992.
- [48] B. Lindmark, “A novel dual polarized aperture coupled patch element with a single layer feed network and high isolation”, in *Antennas and Propagation Society International Symposium, 1997. IEEE., 1997 Digest*, IEEE, vol. 4, 1997, pp. 2190–2193.
- [49] M Yamazaki, E. Rahardjo, and M Haneishi, “Construction of a slot-coupled planar antenna for dual polarisation”, *Electronics letters*, vol. 30, no. 22, pp. 1814–1815, 1994.

- [50] K Ghorbani and R. Waterhouse, “Dual polarized wide-band aperture stacked patch antennas”, *IEEE Transactions on Antennas and Propagation*, vol. 52, no. 8, pp. 2171–2175, 2004.
- [51] T.-W. Chiou and K.-L. Wong, “Broad-band dual-polarized single microstrip patch antenna with high isolation and low cross polarization”, *IEEE Transactions on Antennas and Propagation*, vol. 50, no. 3, pp. 399–401, 2002.
- [52] C.-C. Chang, J.-S. Row, *et al.*, “Dual-feed dual-polarized patch antenna with low cross polarization and high isolation”, *IEEE Transactions on Antennas and Propagation*, vol. 57, no. 10, pp. 3405–3409, 2009.
- [53] Y. Li, Z. Zhang, J. Zheng, and Z. Feng, “Design of dual-polarized monopole-slot antenna with small volume and high isolation”, *IEEE Transactions on Antennas and Propagation*, vol. 60, no. 5, pp. 2511–2514, 2012.
- [54] N. Kuga, H. Arai, and N. Goto, “A notch-wire composite antenna for polarization diversity reception”, *IEEE Transactions on Antennas and Propagation*, vol. 46, no. 6, pp. 902–906, 1998.
- [55] C. Deng, P. Li, and W. Cao, “A high-isolation dual-polarization patch antenna with omnidirectional radiation patterns”, *IEEE antennas and wireless propagation letters*, vol. 11, pp. 1273–1276, 2012.
- [56] X. Quan and R. Li, “A broadband dual-polarized omnidirectional antenna for base stations”, *IEEE Transactions on Antennas and Propagation*, vol. 61, no. 2, pp. 943–947, 2013.
- [57] K.-M. Luk, K.-F. Lee, and J. S. Dahele, “Analysis of the cylindrical-rectangular patch antenna”, *IEEE Transactions on antennas and propagation*, vol. 37, no. 2, pp. 143–147, 1989.
- [58] J Sureau and A Hessel, “Element pattern for circular arrays of axial slits on large conducting cylinders”, *IEEE Transactions on Antennas and Propagation*, vol. 17, no. 6, pp. 799–803, 1969.
- [59] M. Mirmozafari, S. Karimkashi, and G. Zhang, “An overview of dual polarized isolated antennas”, in *Antennas and Propagation (APSURSI), 2016 IEEE International Symposium on*, IEEE, 2016, pp. 1893–1894.

- [60] Z. Bao, X. Zong, Z. Nie, and S. Yang, “Design and discussion of a broadband cross-dipole with high isolation and low cross-polarisation utilising strong mutual coupling”, *IET Microwaves, Antennas & Propagation*, vol. 8, no. 5, pp. 315–322, 2014.
- [61] M Mirmozafari, H Saeidi-Manesh, and G Zhang, “Highly isolated crossed dipole antenna with matched copolar beams”, *Electronics Letters*, vol. 54, no. 8, pp. 470–472, 2018.
- [62] S. M. Rao, T. K. Sarkar, P. Midya, and A. R. Djordevic, “Electromagnetic radiation and scattering from finite conducting and dielectric structures: surface/surface formulation”, *IEEE Transactions on Antennas and Propagation*, vol. 39, no. 7, pp. 1034–1037, 1991.
- [63] R. G. Vaughan and J. B. Andersen, “Antenna diversity in mobile communications”, *IEEE Transactions on vehicular technology*, vol. 36, no. 4, pp. 149–172, 1987.
- [64] C. Fulton, J. L. Salazar, Y. Zhang, G. Zhang, R. Kelly, J. Meier, M. McCord, D. Schmidt, A. D. Byrd, L. M. Bhowmik, *et al.*, “Cylindrical polarimetric phased array radar: beamforming and calibration for weather applications”, *IEEE Transactions on Geoscience and Remote Sensing*, vol. 55, no. 5, pp. 2827–2841, 2017.
- [65] S. Karimkashi and G. Zhang, “A dual-polarized series-fed microstrip antenna array with very high polarization purity for weather measurements”, *IEEE transactions on antennas and propagation*, vol. 61, no. 10, pp. 5315–5319, 2013.
- [66] A Munger, J Provencher, and B Gladman, “Mutual coupling on a cylindrical array of waveguide elements”, *IEEE Transactions on Antennas and Propagation*, vol. 19, no. 1, pp. 131–134, 1971.
- [67] G Borgiotti and Q. Balzano, “Mutual coupling analysis of a conformal array of elements on a cylindrical surface”, *IEEE Transactions on Antennas and Propagation*, vol. 18, no. 1, pp. 55–63, 1970.
- [68] J Herper, A Hessel, and B Tomasic, “Element pattern of an axial dipole in a cylindrical phased array, part i: theory”, *IEEE transactions on antennas and propagation*, vol. 33, no. 3, pp. 259–272, 1985.

- [69] B. Tomasic, A. Hessel, and J. C. Herper, “Element pattern of an axial dipole in a cylindrical phased array. part 1. theory. part 2. element design and experiments. volume 1”, ROME AIR DEVELOPMENT CENTER GRIFFISS AFB NY, Tech. Rep., 1986.
- [70] C. J. Fulton and A. Mirkamali, “A computer-aided technique for the analysis of embedded element patterns of cylindrical arrays [em programmer’s notebook]”, *IEEE Antennas and Propagation Magazine*, vol. 57, no. 3, pp. 132–138, 2015.
- [71] K. F. Braun, “Electrical oscillations and wireless telegraphy”, *Nobel Lecture, December*, vol. 11, no. 1909, pp. 226–245, 1909.
- [72] R. Guinvarc’h and R. L. Haupt, “Dual polarization interleaved spiral antenna phased array with an octave bandwidth”, *IEEE Transactions on Antennas and Propagation*, vol. 58, no. 2, pp. 397–403, 2010.
- [73] S Livingston and J. Lee, “Evolution of wide band array designs”, in *Antennas and Propagation (APSURSI), 2011 IEEE International Symposium on*, IEEE, 2011, pp. 1957–1960.
- [74] V. B. Erturk, O. BakIr, R. G. Rojas, and B. Guner, “Scan blindness phenomenon in conformal finite phased arrays of printed dipoles”, *IEEE transactions on antennas and propagation*, vol. 54, no. 6, pp. 1699–1708, 2006.
- [75] M. A. Khayat, J. T. Williams, D. R. Jackson, and S. A. Long, “Mutual coupling between reduced surface-wave microstrip antennas”, *IEEE Transactions on Antennas and Propagation*, vol. 48, no. 10, pp. 1581–1593, 2000.
- [76] D. E. Forsyth, J. F. Kimpel, D. S. Zrnic, R. Ferek, J. F. Heimmer, T. McNellis, J. E. Crain, A. M. Shapiro, R. J. Vogt, and W. Benner, “The national weather radar testbed (phased-array)”, in *32nd Conference on Radar Meteorology*, 2005, pp. 24–29.
- [77] R. C. Hansen, *Phased array antennas*. John Wiley & Sons, 2009, vol. 213.
- [78] D. M. Pozar, “The active element pattern”, *IEEE Transactions on Antennas and Propagation*, vol. 42, no. 8, pp. 1176–1178, 1994.

- [79] A. O. Boryssenko, “Polarization constraints in dual-polarized phased arrays derived from an infinite current sheet model”, *IEEE Antennas and Wireless Propagation Letters*, vol. 8, pp. 955–958, 2009.
- [80] H Saeidi-Manesh, M Mirmozafari, and G Zhang, “Low cross-polarisation high-isolation frequency scanning aperture coupled microstrip patch antenna array with matched dual-polarisation radiation patterns”, *Electronics Letters*, vol. 53, no. 14, pp. 901–902, 2017.
- [81] K Woelder and J. Granholm, “Cross-polarization and sidelobe suppression in dual linear polarization antenna arrays”, *IEEE transactions on antennas and propagation*, vol. 45, no. 12, pp. 1727–1740, 1997.
- [82] M. Mirmozafari, G. Zhang, S. Saeedi, and R. J. Doviak, “On side lobe problem of configured array antennas”, *IEEE transactions on Antennas and propagation*, 2018.
- [83] A. Ludwig, “The definition of cross polarization”, *IEEE Transactions on Antennas and Propagation*, vol. 21, no. 1, pp. 116–119, 1973.
- [84] N. Marchand, “Transmission-line conversion transformers”, *Electron*, vol. 17, pp. 142–146, 1944.
- [85] Z. Xu and L. MacEachern, “Optimum design of wideband compensated and uncompensated marchand baluns with step transformers”, *IEEE Transactions on Microwave Theory and Techniques*, vol. 57, no. 8, pp. 2064–2071, 2009.
- [86] Z. Zhou, S. Yang, and Z. Nie, “A novel broadband printed dipole antenna with low cross-polarization”, *IEEE transactions on Antennas and propagation*, vol. 55, no. 11, pp. 3091–3093, 2007.
- [87] J. Zhu, S. Liao, S. Li, and Q. Xue, “Wideband low-profile highly isolated mimo antenna with artificial magnetic conductor”, *IEEE Antennas and Wireless Propagation Letters*, 2018.
- [88] S. X. Ta and I. Park, “Dual-band low-profile crossed asymmetric dipole antenna on dual-band amc surface”, *IEEE Antennas and Wireless Propagation Letters*, vol. 13, pp. 587–590, 2014.

Appendix A

3D Printing of Non-Planar Linear Dipole Phased Array Antennas

A unit cell of the proposed antenna array is shown in figure A.1. The elements are simple half-wavelength dipoles situated a quarter wavelength above the ground plane. One pole of each dipole is shown transparent to present the feeding method. They are fed directly using coaxial connectors. The inner conductor of the SMA connector, without any electrical connection, is inserted inside the excited pole of the dipole. The current over this pole is induced through proximity coupling. The outer conductor of the SMA connector is connected to the ground plane directly under the grounded pole of the dipole. The electrical connection between the outer conductor of the SMA connector and the opaque pole in figure A.1 is reinforced using metal vias surrounding this pole. This excitation scheme eliminates the need for balun feedline, resulting in a simple geometry of the array antenna. The gap between two poles of the dipole, denoted by “G”, plays an important role in the performance of the antenna. A parametric study of this variable and its effect on the impedance matching of a single dipole is provided in figure A.2. As seen, the optimum value of this parameter guarantees the differential excitation mode of the dipole.

We have frequently discussed the asymmetry of an element and its destructive effects on polarization purity. This also happens to the proposed design, because of the asymmetric excitation of each dipole with respect to its center. If the elements are simply duplicated in an array, all radiation patterns of the elements are directed to one direction. In order to compensate for the beam tilt of the elements, and return the symmetry to the linear array antenna, we have mirrored the elements with respect to the center of the array antenna. This mirrored arrangement is shown in figure A.1 where two adjacent dipoles are excited at mirrored poles. It can hence be concluded that due to the absolute symmetry of the mirrored array antenna, it will have theoretically zero cross-polarization when the beam is pointed in the broadside direction.

In the design of the array, an inter-element spacing of 63 mm ($0.63 \lambda_u$) was chosen according to the operational frequency range in order to avoid the grating lobe in scanning up to $\pm 45^\circ$. Figure A.3 shows the scanning performance of the middle element. With active VSWR < 1 over the entire operational bandwidth, the proposed antenna has no blindness effect in such an scanning scenario. The proposed array is capable of operating over a wide range of frequencies with desired bandwidth. While the length of the dipole determines the center resonance frequency, the bandwidth can be adjusted by the width of the dipole. The final dimensions of the antenna, used in the current design, are provided in Table A.1.

The proposed linear array was fabricated using stereolithography (SLA) 3D printing technology. Due to the size limit of the utilized 3D printer (Form2 from Formlabs) the array was divided into three similar sub-arrays. However, they were arranged to be fabricated in the same run. The outcome of different steps, used in the fabrication process, are displayed in figure A.4. As

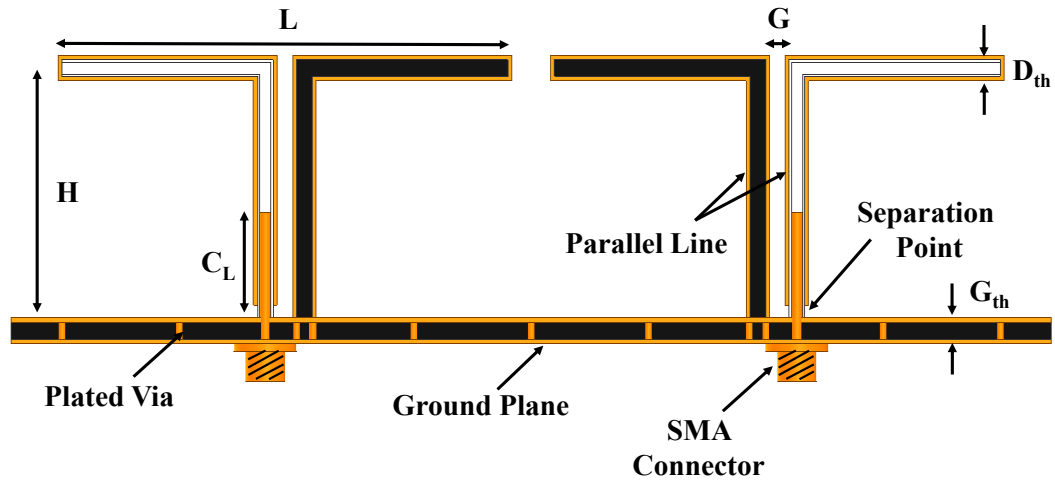


Figure A.1: A unit cell of two imaged linear dipole antennas. One pole of each dipole is shown transparent to present the excitation method.

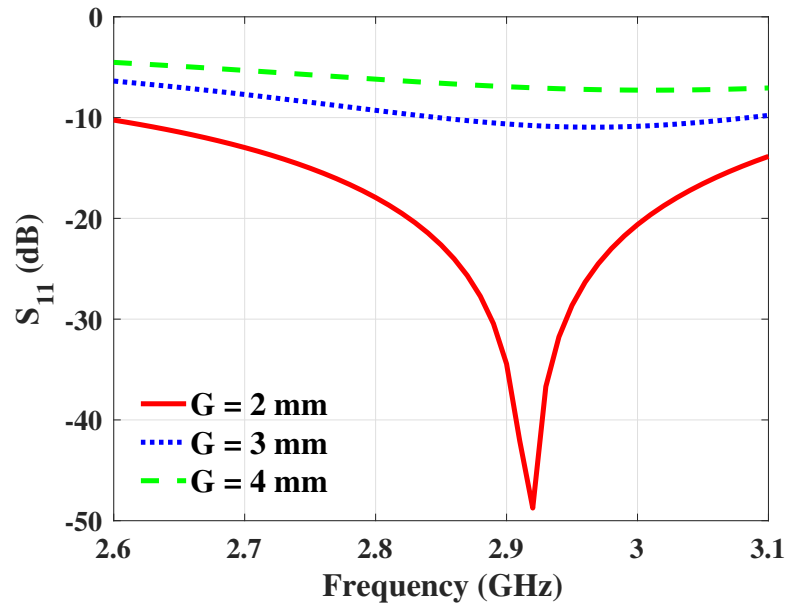


Figure A.2: Reflection coefficient of the single dipole antenna as a function of gap distance between the two poles.

shown, The fabrication process consists of three major steps. First, the whole structure, including the ground plane, the parallel line, and the dipole were printed uniformly in a single step, resulting in a rigid geometry. This eases the manufacturing and assembly processes and precludes any additional soldering

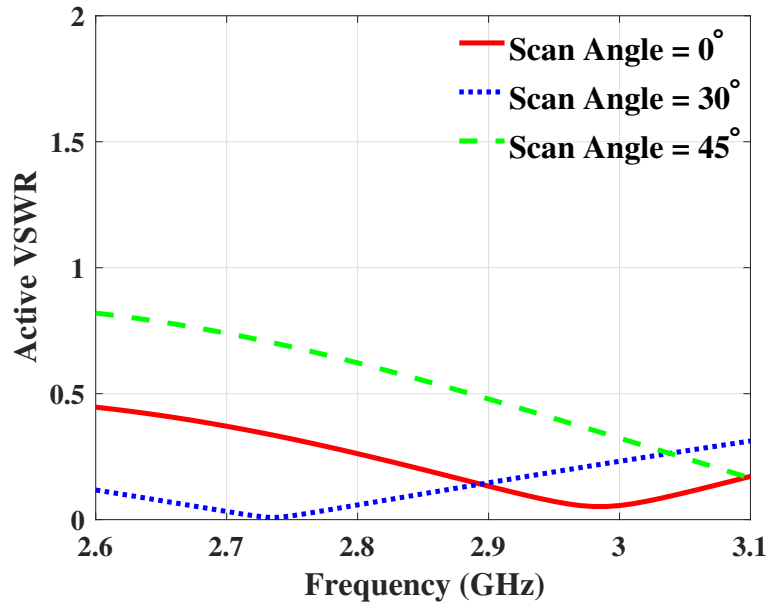


Figure A.3: Simulated active VSWR in 0°, 30°, and 45° scanning angles.

loss. While printing the ground plane, rows of tiny holes were included to form the vias. Then a thin layer of copper was deposited on the whole structure using electro-less plating process. This shiny thin layer of copper that is shown in figure A.4b, provides a base for developing the copper in the next step. Finally, with the aid of high-current electroplating, the surface copper layer was reinforced resulting in a good electric conductivity. The final prototype with the connector assembled is shown in figure A.4c. The outer conductor of the SMA connector was soldered to the bottom surface of the ground plane which is at the same potential as its top surface using metal-plated vias. The inner conductor of the SMA connector was inserted into excited pole of the dipole. The conductive coating of this pole was precisely separated from the ground plane. Besides the ground planes vias, some other ones, as shown in the subset of figure A.4c, surround the opposite pole of the dipole providing a low-impedance connection to the outer conductor of SMA connector.

Table A.1: Detailed Dimensions of the fabricated antenna (unit:*mm*)

Parameters	L	H	G	C_L	D_{th}	G_{th}
Values	55	26	2	10	2.5	2

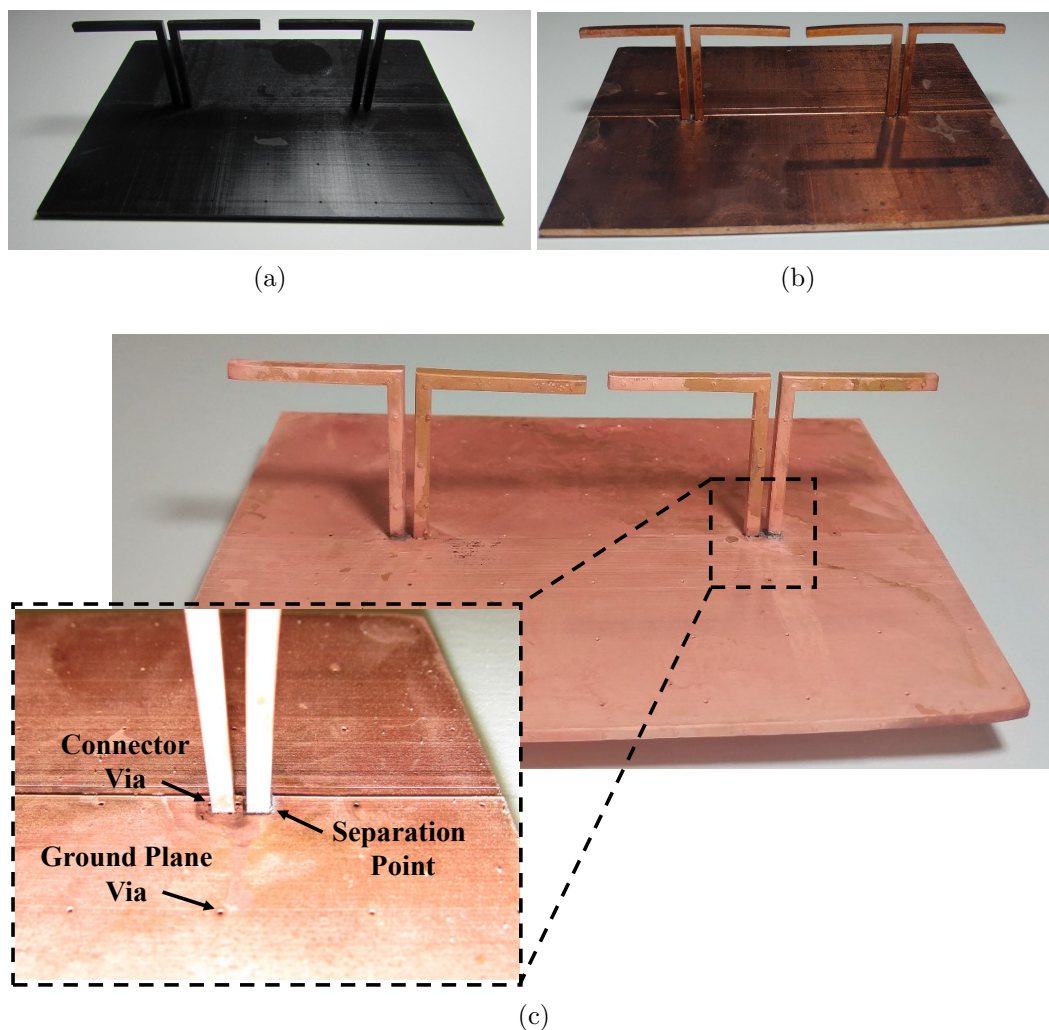


Figure A.4: Antenna prototype after each fabrication process. (a) 3-D printed sample, (b) antenna after electroless plating, (c) final copper coated antenna after electro plating, isolating the excited pole, and soldering of connectors.

A prototype of six-element linear dipole array was fabricated and is shown in figure A.5. This linear array is composed of three blocks of imaged elements situated beside each other. The middle element was excited and its reflection

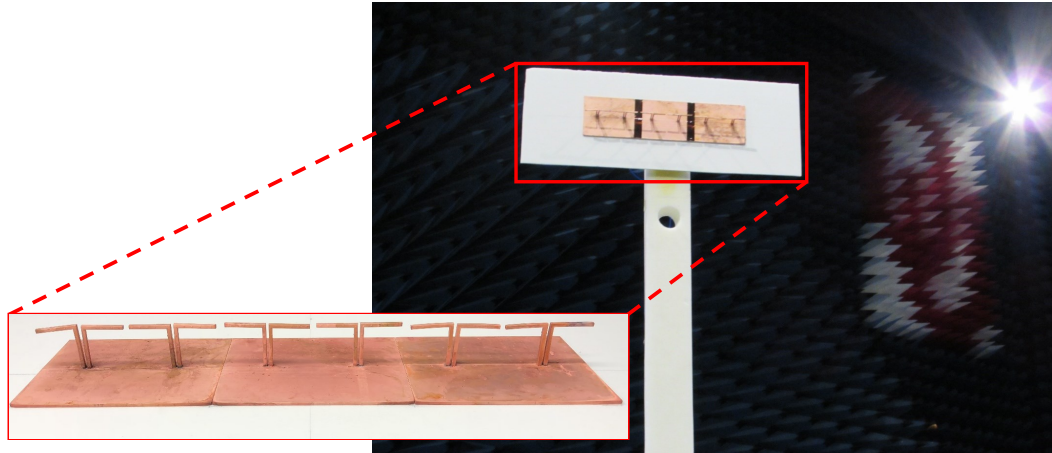


Figure A.5: Linear array antenna and the radiation pattern measurement set-up.

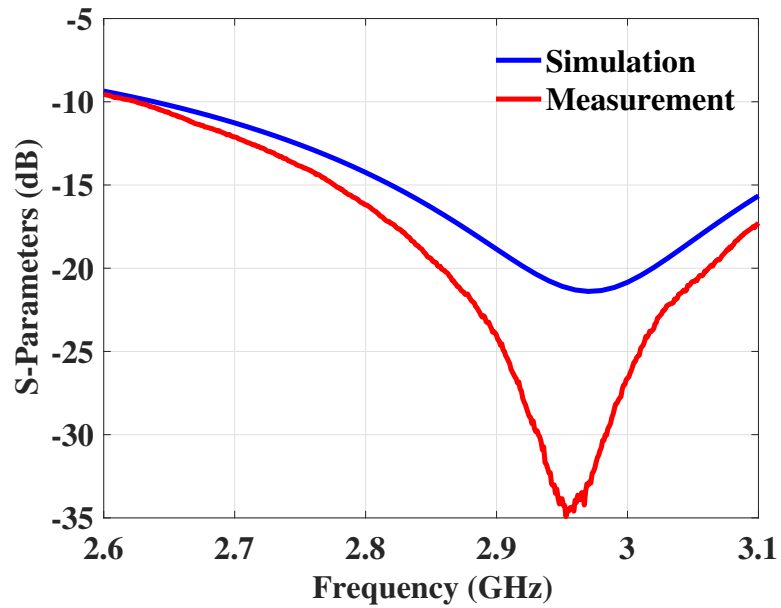


Figure A.6: S-parameter of the middle element in the array.

coefficient, while the other elements are terminated in matched loads, was measured and compared to its simulation counterpart in figure A.6. A good match between two results is observed. They remain below -12 dB over the entire frequency range.

The radiation patterns of the antenna were measured in the far-field ane-

choic chamber at the Advanced Radar Research Center of the University of Oklahoma. Figure A.5 depicts the set-up used for the pattern measurement. The linear array antenna was mounted on a fairly high stand of Rohacell 31HF foam, with a dielectric constant of 1.05, fabricated and mounted over the pedestal. To avoid the bias of phase shifters and splitters, the radiation pattern of each individual element was measured and combined with uniform weighting using MATLAB. The measured E-plane beam scanning performance at the low (2.7 GHz), middle (2.85 GHz) and high (3 GHz) frequencies are displayed in figure A.7. The dipoles and ground plane experienced a slight deformation in plating process. This can be revealed by comparing their shapes before and after plating in figure A.4. This reshaping reduces the polarization purity of the antenna to some extent. Nevertheless, the cross-polarization level while scanning is at least 30 dB below the co-polarized component. This polarization purity could be modified by a thicker dimensions of the dipoles that are more resistant to tensions due to plating. This is an ongoing research effort with the initial results suggesting that higher performance can be achieved by an optimum choice of the antenna dimensions and an appropriate plating process. The 3-D printing technology holds significant potential for a number of applications where customized antennas with light-weight, low-cost, and rapid manufacturing are required.

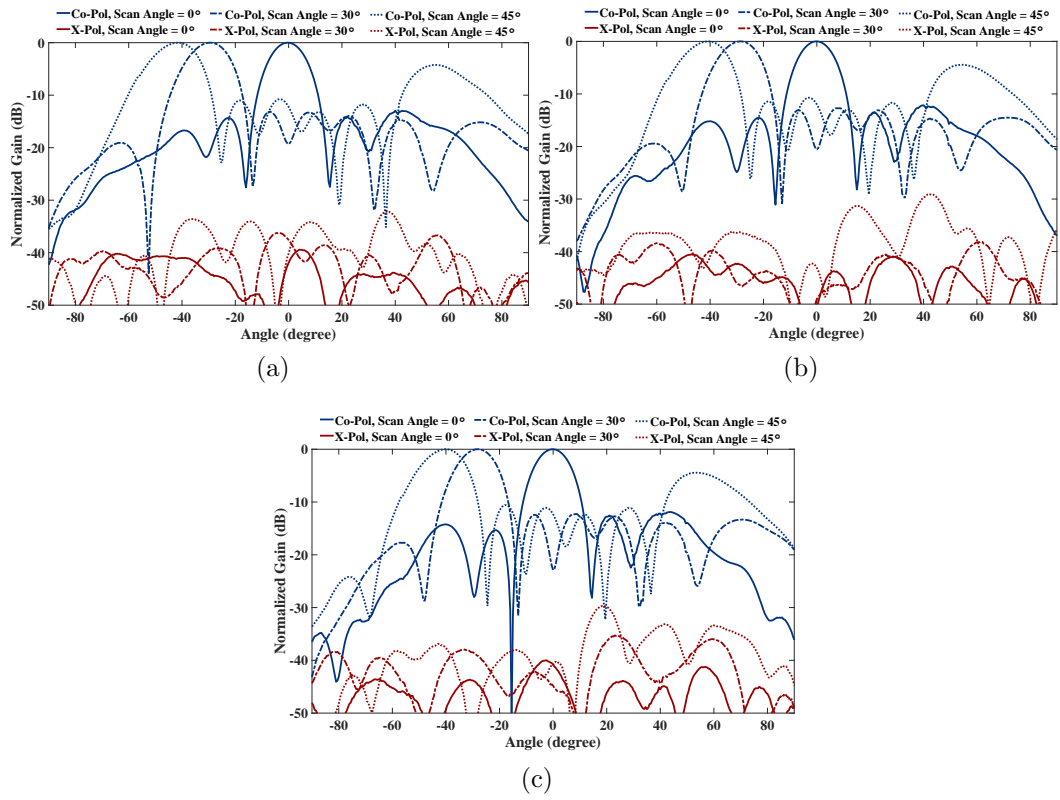


Figure A.7: Measured radiation patterns of the proposed array antenna at different frequencies. (a) 2.7 GHz, (b) 2.85 GHz, and (c) 3 GHz.